CHALMERS
UNIVERSITY OF TECHNOLOGY

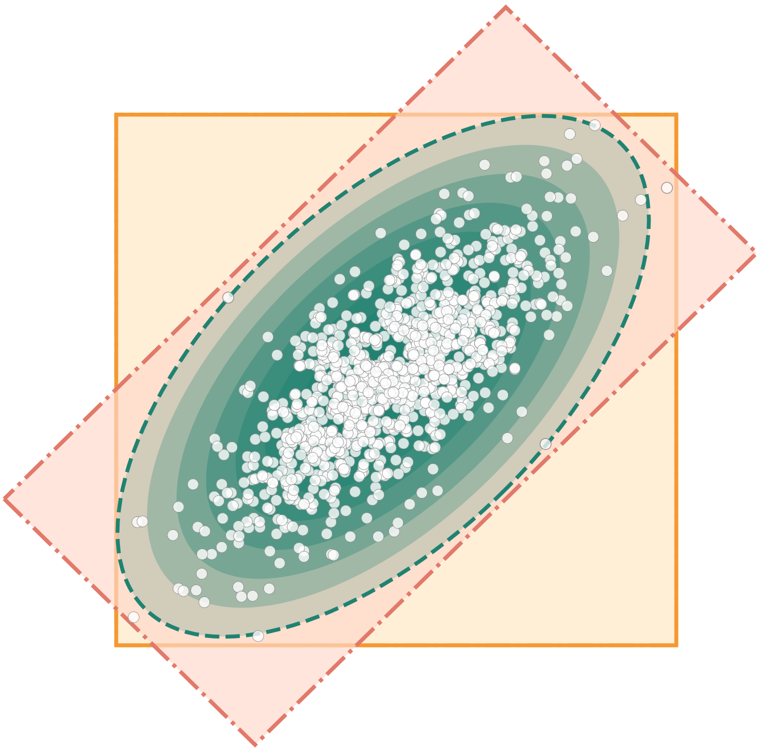

Bayesian History Matching of Chiral Effective Field Theory in the Two-Nucleon Sector

An Exploration of Non-Implausible Low-Energy Constants at Leading Order in a Modified Weinberg Power Counting

Master's thesis in Physics

ELEANOR MAY

DEPARTMENT OF PHYSICS

CHALMERS UNIVERSITY OF TECHNOLOGY
Gothenburg, Sweden 2022
www.chalmers.se

Master's thesis 2022

Bayesian History Matching of Chiral Effective Field Theory in the Two-Nucleon Sector

An Exploration of Non-Implausible Low-Energy Constants at Leading Order in a Modified Weinberg Power Counting

Eleanor May

CHALMERS
UNIVERSITY OF TECHNOLOGY

Department of Physics
Division of Subatomic, High Energy and Plasma Physics
Theoretical Subatomic Physics
Chalmers University of Technology
Gothenburg, Sweden 2022

Bayesian History Matching of Chiral Effective Field Theory in the Two-Nucleon Sector
An Exploration of Non-Implausible Low-Energy Constants at Leading Order in a Modified Weinberg Power Counting
Eleanor May

Supervisor: Christian Forssén, Department of Physics
Examiner: Christian Forssén, Department of Physics

Master's Thesis 2022
Department of Physics
Division of Subatomic, High Energy and Plasma Physics
Theoretical Subatomic Physics
Chalmers University of Technology
SE-412 96 Gothenburg
Telephone +46 31 772 1000

Cover: Two-dimensional representation of hyperrectangle (yellow), rotated hyperrectangle (red), and Gaussian (green) non-implausible volumes, implemented as sampling techniques within the Bayesian history matching method. Volumes are constructed around a set of non-implausible samples (white circles). The figure is equivalent to Fig. 5.1 in Chapter 5.

Typeset in LaTeX
Printed by Chalmers Reproservice
Gothenburg, Sweden 2022

Bayesian History Matching of Chiral Effective Field Theory in the Two-Nucleon Sector
An Exploration of Non-Implausible Low-Energy Constants at Leading Order in a Modified Weinberg Power Counting
Eleanor May
Department of Physics
Chalmers University of Technology

Abstract

The accurate calculation of nucleon-nucleon scattering observables from first principles is an ongoing challenge within nuclear physics. Working within the framework of chiral effective field theory provides a method for calculating such observables. This is achieved through the construction of an effective Lagrangian that maintains the symmetries of quantum chromodynamics (QCD). In this thesis, truncation of the Lagrangian is performed using a modified Weinberg power counting, introducing a set of unknown low-energy constants at each order in the chiral expansion.

Bayesian history matching is used to explore the leading order description of the nucleon-nucleon system. This is achieved through the iterative reduction of the four-dimensional parameter space, taking a Bayes linear approach. The history matching implementation is validated on the nuclear liquid drop model. Several novel methods of sampling are introduced within the implementation with the purpose of capturing correlations between parameters; The generation of ellipsoidal distributed samples is shown to be the most successful. History matching is subsequently applied to the proton-neutron scattering problem. We identify the subset of parameter space containing all low-energy constants that produce model outputs consistent with experimental two-nucleon scattering data, accounting for relevant sources of uncertainty. Non-implausible parameter volumes are obtained across a range of momentum regulator cutoffs. A set of non-implausible samples are used to predict the deuteron binding energy. Results indicate that the inclusion of this observable within the history match could further constrain the volumes.

The analysis performed in this thesis was successful in producing sets of non-implausible samples. Such sets can be subsequently used as a starting point for a full Bayesian analysis, with the aim of producing posterior probability distributions of the parameters. For example, the samples can be used to initialise walkers within the Markov Chain Monte Carlo method.

Keywords: global parameter search, computer models, history matching, nuclear physics, liquid drop model, nucleon-nucleon scattering, chiral effective field theory, modified Weinberg power counting, emulators

Acknowledgements

First and foremost, I would like to thank my supervisor Prof. Christian Forssén for all of his guidance. His wealth of knowledge, thought-provoking feedback, and meticulous proofreading have proved to be indispensable to this project. I would also like to thank the members of the Theoretical Subatomic Physics group for the many interesting discussions. In particular, I thank Prof. Andreas Ekström and Oliver Thim for their valuable insight.

Finally, I thank my partner Andreas for his never-ending support and encouragement. Without him, this thesis would not have been possible.

Eleanor May, Gothenburg, May 2022

List of Acronyms

Below is the list of acronyms that have been used throughout this thesis, listed in alphabetical order:

AME2016	Atomic Mass Evaluation 2016
χEFT	Chiral Effective Field Theory
ChPT	Chiral perturbation theory
DSG	Differential cross section
EFT	Effective Field Theory
LEC	Low-energy constant
LH	Latin hypercube
LO	Leading order
NLO	Next-to-leading order
MCMC	Markov Chain Monte Carlo
MWPC	Modified Weinberg power counting
NN	Nucleon-nucleon
np	Neutron-proton
OLS	Ordinary least squares
PB	Polarisation of the beam
PDF	Probability density function
QCD	Quantum chromodynamics
RG	Renormalisation group
SGT	Total cross section
WPC	Weinberg power counting

Contents

List of Figures

List of Tables

Chapter 1

Introduction

The driving force behind nuclear physics is the goal to understand the properties of atomic nuclei. The nucleon-nucleon (NN) scattering process provides valuable insight into these properties and the forces which govern them. Scattering phase shifts and scattering observables can be determined numerically starting from a realistic model of the nuclear interaction, developed within the framework of chiral effective field theory (χEFT) [1–6]. This framework originates in chiral perturbation theory (χPT) [7] and leads to an infinite number of interaction terms. These terms can be ordered using a power counting scheme, leading to a finite number of terms at a given order. Modified Weinberg power counting (MWPC), as defined in Refs. [6, 8, 9], is the scheme used within this thesis. However, the use of this framework introduces a set of unknown parameters named low-energy constant (LEC)s. The number of LECs depends upon the truncation order of the scheme. In this thesis, leading order is considered, which for our MWPC implies that a four-dimensional parameter space must be explored.

The governing of a model by a set of unknown input parameters is not unusual, particularly in the case of complex computer models. In these cases, the model can be fitted to experimental data through parameter optimisation, aiming to minimise the difference between the model output and the given data. However, such parameter optimisation can be challenging, particularly in high dimensional cases. In this project, the problem of multi-parameter optimisation is approached using the Bayesian history matching method [10, 11]. The use of history matching corresponds to a Bayes linear approach [12] and eliminates the need for a full probabilistic analysis. This method is an iterative process that allows a set of non-implausible model parameters to be identified and subsequently used to make model predictions. However, evaluating the model over a large parameter space to perform a history match can be computationally demanding. Instead, emulators are incorporated into the history matching scheme. This allows approximations of the model to be made and significantly lessens the computational cost.

This thesis is divided into two main areas of study. The focus will first lie on the investigation and validation of the history matching scheme using the nuclear liquid drop model as a toy model. This will involve the introduction of several sampling designs, defined as types of non-implausible volumes. The purpose of this first area of study is to answer the following questions:

1. Does the method of history matching, when applied to the liquid drop model, successfully show a reduction in parameter space? Furthermore, does a set of optimal input parameters obtained using linear regression fall within the obtained non-implausible parameter volume?
2. Can alternative sampling methods be introduced to the history matching scheme, with the aim of successfully capturing correlations between input parameters?
3. How do the alternative sampling designs perform in terms of sampling efficiency, when compared to sampling methods typically used within history matching?

The second area of focus of this thesis will be the modelling of the neutron-proton (np) system. This will involve the application of history matching to χEFT at leading order (LO) in MWPC [9, 13]. The final aim is to locate the region(s) of parameter space that lead to acceptable matches between model outputs and data. The analysis will be performed using experimental data on scattering phase shifts [14, 15] and scattering observables. A history match will be first performed using a momentum regulator cutoff of $\Lambda = 450$ MeV. The obtained set of non-implausible samples will be used to predict an observable that was not included within the history match, in order to investigate the performance of the method. Finally, history matches will be performed for a range of momentum regulator cutoffs in order to explore the non-implausible LECs obtained in each case.

Both history matching and χEFT are topics of a wide scope. However, this thesis is only able to explore a limited number of the possibilities offered by these research topics. Therefore, potential outlooks and improvements to the current work will be discussed in the final chapter of the thesis.

Part I

Theory

Chapter 2

Bayesian History Matching

2.1 An Introduction to History Matching

History matching [10, 11, 16] is a statistical method used to iteratively identify the set of all acceptable input parameters for a computer model of a physical system. The goal of history matching may be to locate a parameter volume with the aim of learning more about the parameters or the model in question. Alternatively, one may wish to infer a set of optimum parameters through the construction of a posterior distribution. In this case, the aim of the history match is to reduce the parameter volume enough so to perform a full Bayesian analysis at the next stage. One method is to use the remaining set of parameter samples as initial positions when performing Markov Chain Monte Carlo (MCMC) sampling [17].

The aim is to identify all such non-implausible parameter choices for (a vector of) given observational data $\boldsymbol{z}$. Each observational datapoint z_i, corresponds to a measurement of the physical system y_i, differing by an observational error $\epsilon_{\text{exp, i}}$. The observational errors are modelled as stochastic variables, such that each error is specified via its mean $\mathbb{E}[\epsilon_{\text{exp, i}}]$ and variance $\text{Var}[\epsilon_{\text{exp, i}}]$. In this thesis, we make the assumption that $\mathbb{E}[\epsilon_{\text{exp, i}}] = 0$, but note that this is not always the case. The relation between the vectors of quantities is given by

$$\boldsymbol{z} = \boldsymbol{y} + \boldsymbol{\epsilon}_{\text{exp}}. \tag{2.1}$$

The model is unlikely to perfectly represent a physical system, giving rise to additional uncertainties. The model is represented as a function of a vector of input parameters $\boldsymbol{\theta}$ that produces a vector of model outputs $\boldsymbol{M}(\boldsymbol{\theta})$. It can therefore be stated that

$$\boldsymbol{y} = \boldsymbol{M}(\boldsymbol{\theta}) + \boldsymbol{\epsilon}_{\text{model}} + \boldsymbol{\epsilon}_{\text{method}}, \tag{2.2}$$

where $\epsilon_{\text{model},i}$ is the model discrepancy [18] corresponding to the model output M_i, and specified via $\mathbb{E}[\epsilon_{\text{model, i}}]$ and $\text{Var}[\epsilon_{\text{model, i}}]$. It represents uncertainty due to approximations and simplifications within the model. $\epsilon_{\text{method},i}$ is similarly defined as a stochastic variable with $\mathbb{E}[\epsilon_{\text{method, i}}]$ and $\text{Var}[\epsilon_{\text{method, i}}]$. It is known as the method uncertainty and the term represents uncertainty arising from the computational method used to obtain numerical model solutions. Similarly to earlier, we assume that $\mathbb{E}[\epsilon_{\text{model, i}}] = 0$ and $\mathbb{E}[\epsilon_{\text{method, i}}] = 0$.

We define $Q(\boldsymbol{z})$ as the set of all input parameters that lead to an acceptable model fit through the fulfillment of Eq. (2.2). To identify $Q(\boldsymbol{z})$, the model must be evaluated over parameter space. Unless the model solution is available as a closed form expression, one must choose a reduced area of parameter space to explore. Even so, this parameter volume may be large. In the case of complex computer models, a large parameter space may lead to a computer evaluation that is too costly for full exploration. To counter this, some models allow for the construction of an emulator. This emulator is used to evaluate an approximation to the model output $\tilde{\boldsymbol{M}}(\boldsymbol{\theta})$. The resulting relation is defined by

$$\boldsymbol{M}(\boldsymbol{\theta}) = \tilde{\boldsymbol{M}}(\boldsymbol{\theta}) + \boldsymbol{\epsilon}_{\text{em}}, \tag{2.3}$$

where an additional uncertainty ϵ_{em} has been introduced, corresponding to the error arising due to the use of an emulator. An input parameter vector $\hat{\boldsymbol{\theta}}$ therefore leads to an acceptable model fit if the following relation is fulfilled:

$$\boldsymbol{z} = \tilde{\boldsymbol{M}}(\hat{\boldsymbol{\theta}}) + \boldsymbol{\epsilon}_{\text{exp}} + \boldsymbol{\epsilon}_{\text{model}} + \boldsymbol{\epsilon}_{\text{method}} + \boldsymbol{\epsilon}_{\text{em}}. \tag{2.4}$$

As described, the uncertainties are modelled as stochastic variables and thus they are described by probabilistic distributions that can be approximated. In the context of history matching, the variances of the uncertainties are incorporated into a metric used to iteratively exclude implausible parameter regions in order to obtain $Q(\boldsymbol{z})$. This metric is named the *implausibility metric* and evaluates the distance between an expectation value $\mathbb{E}[\tilde{\boldsymbol{M}}]$ outputted by the emulator for a given $\boldsymbol{\theta}$ and the observation $\boldsymbol{z}$, standardised by the aforementioned uncertainties. Assuming uncorrelated outputs, the implausibility metric is defined as

$$I^2(\boldsymbol{\theta}) \equiv \max_{z_i \in \mathcal{Z}} \frac{\left|\mathbb{E}[\tilde{M}_{\text{i}}(\boldsymbol{\theta})] - z_{\text{i}}\right|^2}{\sigma^2_{\text{exp,i}} + \sigma^2_{\text{model,i}} + \sigma^2_{\text{method,i}} + \sigma^2_{\text{em,i}}}. \tag{2.5}$$

Where $\mathcal{Z}$ is the set of relevant observables. The denominator is the sum of the variances of the uncertainties for the ith observable, written as $\sigma^2_{\text{exp,i}} = \text{Var}[\epsilon_{\text{exp,i}}]$, $\sigma^2_{\text{model,i}} = \text{Var}[\epsilon_{\text{model,i}}]$, $\sigma^2_{\text{method,i}} = \text{Var}[\epsilon_{\text{method,i}}]$, and $\sigma^2_{\text{em,i}} = \text{Var}[\epsilon_{\text{em,i}}]$.

The implausibility metric assigns each set of input parameters $\boldsymbol{\theta}$ an implausibility value $I(\boldsymbol{\theta})$. An implausibility cut-off can then be imposed. Following Pukelsheim's 3-sigma rule [19], all input parameters with $I(\boldsymbol{\theta}) > 3$ are determined to be implausible and subsequently discarded. Note that a case of $I(\boldsymbol{\theta}) \leq 3$ does not imply that $\boldsymbol{\theta}$ is plausible but simply that it cannot be ruled out at this stage. Similarly, history matching is a *likelihood free* method since the uncertainties are only described by their expectation values and variances, rather than a fully specified probability density function (PDF) for each. Therefore, a lower value of $I(\boldsymbol{\theta})$ does not imply a greater 'plausibility' than a higher value would, if both values fall below the cut-off.

Due to the existence of multiple observables $z_i \in \mathcal{Z}$, and therefore multiple implausibilities obtained for each observable at a given $\boldsymbol{\theta}$, Eq. (2.5) requires a maximum implausibility value to be taken. We denote the maximum implausibility by I_M. An alternate approach is to take the second or third highest implausibility value, denoted I_{2M} and I_{3M} respectively, ensuring that errors in uncertainty variance estimates do not lead to unfairly labelling points as implausible.

The iterations of a history match are known as *waves*. Each wave operates as follows:

1. A conservative number of parameter samples are generated over the non-implausible parameter volume Q_n. These samples are chosen using a space filling design. The model is evaluated for this set of input parameter samples.
2. When emulating the model, we require a set of training data for the emulator. The previously obtained set of model evaluations, alongside the set of parameter samples used to generate them, form the training data. The emulator is then fitted over the entirety of Q_n using the training data.
3. A larger number parameter samples are generated within Q_n, again using a space filling design. The emulator is used to generate an output for each sample.
4. The implausibility metric is evaluated for the emulator outputs. The implausibility cut-off is imposed and all input parameters with $I(\boldsymbol{\theta})$ greater than the cut-off are discarded.
5. The remaining parameter samples define the new non-implausible volume Q_{n+1}, which could be several orders of magnitude smaller than Q_n.
6. The waves continue until one of two conditions are met. If the emulator uncertainty falls below the other uncertainties, additional iterations will not further decrease the size of the non-implausible region and the history match is terminated. Alternatively, if the non-implausible region is empty, the scheme is ended. If neither of these criteria are fulfilled, the above scheme is repeated, now sampling over Q_{n+1}.

In the $(n+1)$th wave, the non-implausible parameter volume $Q_{\mathrm{n+1}}$ is smaller than that of the previous wave's volume Q_{n}. The exact definition of the non-implausible parameter volume will be explored later in this thesis (see Section 5).

The strength of the history matching scheme lies within its ability to achieve this volume reduction. This is accomplished through the elimination of parameter space containing samples deemed implausible through the comparison of model outputs with observational data. There are several ways in which the non-implausible volume may continue to shrink after the initial wave:

- In each wave after the first, new samples are generated within a smaller volume than in the previous wave. Therefore, the density of samples is greater than in the previous wave, if the total number of samples is kept constant. The emulator then improves as the model function within the decreased volume becomes smoother. Consequently, the emulator variance decreases and samples that were previously non-implausible may be deemed implausible.
- Additional observables may be introduced in later waves. The parameter space

is now further constrained by these observables.
- One or more parameters may be chosen to act as *inactive* during earlier waves and ‘activated’ in a later wave. Since an inactive parameter introduces initial uncertainty, and this uncertainty is removed once the parameter is introduced. Samples deemed non-implausible before may now be implausible.

2.1.1 Model Discrepancy

The idea of model discrepancy was briefly introduced in relation to history matching. This section will discuss the concept further.

Models are used to predict the behaviour of a physical system. It is unlikely that a model will perfectly represent any real physical system, resulting in a systematic error between the model output and the physical quantity — the *model discrepancy*. The model discrepancy is especially relevant in the case of models of a system as complex as the atomic nucleus. If calculation of the discrepancy was trivial, then such a value would be incorporated into the model directly. Instead it requires a more considered approach — the estimation of the probabilistic distribution of the discrepancy.

In most cases, it is not possible to solve for model parameters analytically. This does not allow for model outputs to be generated with the explicit goal of comparison with data, and thus the uncertainty cannot be quantified directly. In reality, one generally requires the model uncertainty in order to infer the parameters. However, a deeper consideration of the model itself may reveal simplifications and approximations that lead to the existence of a discrepancy. As a result, expert opinion is often a useful way to approximate the probabilistic distribution of the model uncertainty, as utilised in Refs. [10, 11]. Alternatively, some models may allow the discrepancy to be estimated through an investigation of the construction of the model. For example, χEFT offers a systematic way to quantify the model discrepancy via the knowledge of the magnitudes of truncated orders (see Section 3.2).

There exist alternative, and potentially more robust, methods for the approximation of model discrepancy. For example, modelling the model discrepancy as a Gaussian process has been shown to lead to model predictions compatible with observational data [18]. However, such a method is out of the scope of this thesis.

2.2 Emulation

In order to determine the implausibility over the parameter space, it is required to evaluate the model over such a space. However, this is infeasible for a computationally expensive, complex model operating within a high dimensional parameter space. An alternative approach is the construction of emulators. Emulators, given a set of training data, can approximate model outputs.

In several history matching implementations [10, 11, 17] the Bayes Linear approach is implemented. In this approach, an emulator is constructed that can predict outputs based only on mean and covariance values.

2.2.1 Gaussian Process Emulators

Gaussian processes provide a powerful approach to approximating model outputs through the incorporation of prior knowledge. This thesis will provide a brief overview of the core concepts behind Gaussian process emulators. It will follow the approach given in Ref. [20] which may be referred to for a more comprehensive description. To preserve a sense of continuity, the notation used in the following sections will follow that of Section 2.1 rather than that of [20].

A Gaussian process consists of a collection of random variables such that any finite subset of variables has a multivariate Gaussian distribution. It is entirely defined by the mean function $\mu(\boldsymbol{\theta})$ and the covariance function $k(\boldsymbol{\theta}, \boldsymbol{\theta}')$ of a real process $u(\boldsymbol{\theta})$ and may be written as

$$u(\boldsymbol{\theta}) \sim \mathcal{GP}\Big(\mu(\boldsymbol{\theta}), k(\boldsymbol{\theta}, \boldsymbol{\theta}')\Big). \tag{2.6}$$

A common choice of covariance function, and that used in this thesis, is the *squared exponential* kernel, given by

$$\text{cov}\Big(u(\boldsymbol{\theta}), u(\boldsymbol{\theta}')\Big) = k(\boldsymbol{\theta}, \boldsymbol{\theta}') = \sigma_f^2 \text{exp}\Big(\frac{||\boldsymbol{\theta} - \boldsymbol{\theta}'||^2}{2\ell^2}\Big). \tag{2.7}$$

Where the correlation length ℓ and variance σ_f^2 are hyperparameters. The aim of a Gaussian process emulator is to infer the posterior distribution over functions given a training set of input parameters $\boldsymbol{\theta}_t$ and corresponding function outputs $\boldsymbol{u}_t = u(\boldsymbol{\theta}_t)$. The posterior distribution over outputs $\boldsymbol{u}$ for a set of test inputs $\boldsymbol{\theta}$ can be expressed through Bayes' theorem. Bayes' theorem is defined as

$$\text{posterior} = \frac{\text{likelihood} \times \text{prior}}{\text{marginal likelihood}}. \tag{2.8}$$

In the context of our model, this may be written as

$$p(\boldsymbol{u} \mid \boldsymbol{\theta}_t, \boldsymbol{\theta}, \boldsymbol{u}_t) \propto p(\boldsymbol{u}_t \mid \boldsymbol{\theta}, \boldsymbol{\theta}_t, \boldsymbol{u}) p(\boldsymbol{u}). \tag{2.9}$$

Working in a Bayesian formalism allows for the assumption of a Gaussian process prior over functions in the form of Eq. (2.6). By definition of a Gaussian process, the joint distribution of the training outputs and the test outputs must be Gaussian. It can be expressed as

$$\begin{bmatrix} \boldsymbol{u}_t \\ \boldsymbol{u} \end{bmatrix} \sim \mathcal{N}\left(\begin{bmatrix} \mu(\boldsymbol{\theta}_t) \\ \mu(\boldsymbol{\theta}) \end{bmatrix}, \begin{bmatrix} k(\boldsymbol{\theta}_t, \boldsymbol{\theta}_t) & k(\boldsymbol{\theta}_t, \boldsymbol{\theta}) \\ k(\boldsymbol{\theta}, \boldsymbol{\theta}_t) & k(\boldsymbol{\theta}, \boldsymbol{\theta}) \end{bmatrix}\right). \tag{2.10}$$

It can then be shown (see Ref. [20] for a detailed derivation) that the posterior has a Gaussian distribution of the form

$$\begin{aligned} p(\boldsymbol{u} \mid \boldsymbol{\theta}, \boldsymbol{\theta}_t, \boldsymbol{u}) = \mathcal{N}\Big(&\mu(\boldsymbol{\theta}) + k(\boldsymbol{\theta}, \boldsymbol{\theta}_t) k(\boldsymbol{\theta}_t, \boldsymbol{\theta}_t)^{-1} (\boldsymbol{u} - \mu(\boldsymbol{\theta}_t)), \\ &k(\boldsymbol{\theta}, \boldsymbol{\theta}) - k(\boldsymbol{\theta}, \boldsymbol{\theta}_t) k(\boldsymbol{\theta}_t, \boldsymbol{\theta}_t)^{-1} k(\boldsymbol{\theta}_t, \boldsymbol{\theta})\Big). \end{aligned} \tag{2.11}$$

2.2.2 Regression Plus Gaussian Process Emulators

Refs. [10, 11, 17] implement emulators within their history matching schemes that combine the use of regression and Gaussian processes. In this work, the same approach is taken, and the construction of the emulator for the ith model output M_i is defined as

$$\tilde{M}_i(\boldsymbol{\theta}) = \sum_j \beta_{ij} g_{ij}(\boldsymbol{\theta}) + u_i(\boldsymbol{\theta}) + w_i. \tag{2.12}$$

The first term is simply a regression term, where β_{ij} are regression coefficients corresponding to low order polynomial functions $g_{ij}(\boldsymbol{\theta})$ of the input parameter vector $\boldsymbol{\theta}$. The second term is a Gaussian process. The regression term allows for the global behaviour of the model to be captured. The Gaussian process term is then used to emulate the model's local behaviour, better accounting for the model's complexity. In the case of high dimensional parameter spaces, a subset of the parameters may have the greatest effect on model output. The remaining parameters may then be classed as *inactive parameters.* w_i is a 'nugget' term that may be used to model any noise arising from the existence of inactive parameters.

Since the Gaussian process is used to model local behaviour, $u_i(\boldsymbol{\theta})$ is assumed to have zero mean. The regression term acts similarly to the mean function usually present in a Gaussian process. Implementing the relation given in Eq. (2.11) alongside Eq. (2.12) gives the expectation value of the model output, which may be written as

$$\mathbb{E}[\tilde{M}(\boldsymbol{\theta})] = \mu(\boldsymbol{\theta}) + k(\boldsymbol{\theta}, \boldsymbol{\theta}_t) k(\boldsymbol{\theta}_t, \boldsymbol{\theta}_t)^{-1} (\boldsymbol{M} - \mu(\boldsymbol{\theta}_t)) \tag{2.13}$$

$$\mu(\boldsymbol{\theta}) = \sum_j \mathbb{E}[\beta_{ij}] g_{ij}(\boldsymbol{\theta}). \tag{2.14}$$

Similarly, the variance is given as

$$\mathrm{Var}[\tilde{M}(\boldsymbol{\theta})] = \mathrm{Var}[\sum_j \beta_{ij} g_{ij}(\boldsymbol{\theta})] - k(\boldsymbol{\theta}, \boldsymbol{\theta}_t) k(\boldsymbol{\theta}_t, \boldsymbol{\theta}_t)^{-1} k(\boldsymbol{\theta}_t, \boldsymbol{\theta}). \tag{2.15}$$

Chapter 3

Chiral Effective Field Theory

Quantum chromodynamics (QCD) provides the fundamental theory behind the strong nuclear force, formulated in terms of quarks interacting via the exchange of gluons. The theory of QCD is encoded within a Lagrangian. Despite the deceptive simplicity of possessing all QCD information within a single Lagrangian, performing predictions using QCD has proved to be difficult. Due to the large scope of QCD, this thesis cannot provide a comprehensive description of the theory. An overview of QCD can instead be found at [21]. However, the complexity of solving QCD is introduced to explain the difficultly that nuclear physicists have faced for decades in the effort to model nuclear interactions. In the high-energy regime, pertubative techniques are seen to be effective. However, QCD is non-perturbative in the low-energy regime in which nuclear physicists are interested [9]. Lattice QCD [22] offers a method for the computation of low-energy quantities, but is extremely computationally intensive. Instead, effective theories are currently widely used.

The effective field theory (EFT) approach [23] allows for an approximate description of a physical system at a given energy scale, taking into account only the degrees of freedom relevant at the chosen scale. To do so, a separation of scales must be identified. Alongside a separation of scales, there are several more important properties of an EFT. Firstly, an EFT must be consistent with the symmetries present in the underlying theory, typically leading to an infinite number of terms. Furthermore, the problem of having an infinite number of terms is handled by the idea of power counting. In this case, an expansion parameter is introduced and each term is dependent on the parameter to a certain order. This orders the terms by their relative importance and allows for the identification of leading order terms that will have the greatest influence. The concept of power counting is discussed further in Section 3.1. A second important feature of an EFT is the requirement of renormalizability at each order [8].

χEFT [4] is an EFT developed according to the underlying theory of QCD, where nucleons and pions are treated as degrees of freedom. χEFT is named as such since it is consistent with the broken chiral symmetry of QCD, amongst other symmetries. The separation of scales is based on the significant difference between pion mass m_π and the chiral-symmetry-breaking scale Λ_χ. The soft scale is therefore approximated as the maximum of either the nucleon momentum p or the pion mass $m_\pi \sim 140$ MeV, for low energies. The chiral-symmetry-breaking scale is known as the hard scale $\Lambda_\chi \leq\sim 1$ GeV.

The Lagrangian is based upon Weinberg's 'Folk Theorem' [1], which motivates the construction of an effective Lagrangian including *all* terms consistent with symmetries (and broken symmetries). The prediction of low-energy nuclear observables is then possible through the calculation of amplitudes of Feynman diagrams to a given order of an expansion in terms of a small parameter. This small parameter is defined as the ratio between the soft scale and hard scale, and is given by

$$Q = \frac{\max(p, m_\pi)}{\Lambda_\chi}, \tag{3.1}$$

3.1 Power Counting

There exist an infinite number of terms within the effective Lagrangian — clearly an impracticable feature as one must derive all terms and will subsequently possess an infinite number of unknown parameters, where such a parameter is known as a LEC. The solution to this problem utilises the aforementioned separation of scales to perform an expansion. A power counting scheme was first demonstrated in several papers by Weinberg [1–3] and has been further developed since [5, 24, 25]. Within the scheme, contributions to χEFT scale with $(Q/\Lambda_\chi)^\nu$. The value of such a scheme is that it allows for a truncation of the expansion at a particular order ν. Calculations may be made to a desired precision through the inclusion of higher order terms.

At LO in Weinberg power counting (WPC), the interaction potential in momentum space is given by

$$V_{\mathrm{LO}}^{\mathrm{WPC}}(\boldsymbol{p}, \boldsymbol{p}') = -\frac{g_A^2}{4f_\pi^2}\tau_1 \cdot \tau_2 \frac{(\sigma_1 \cdot \boldsymbol{q})(\sigma_2 \cdot \boldsymbol{q})}{m_\pi^2 + \boldsymbol{q}^2} + \widetilde{C}_{^1S_0}\hat{P}_{^1S_0} + \widetilde{C}_{^3S_1}\hat{P}_{^3S_1}. \tag{3.2}$$

The first term is the one-pion-exchange potential. g_A is the axial coupling and f_π is the pion-decay constant. σ and τ are the spin and isospin, respectively, where the subscripts refer to the nucleon in the interaction. The second and third terms act as NN contact terms and are accompanied by two LECs, $\widetilde{C}_{^1S_0}$ and $\widetilde{C}_{^3S_1}$, acting in the $^1S_0$ and $^3S_1$ partial waves, respectively[1]. $\hat{P}_{^1S_0}$ and $\hat{P}_{^3S_1}$ are projection operators.

The use of WPC has yielded successful results when modelling the nuclear interaction. However, WPC must be modified if one wants to achieve renormalisation group-invariance [6, 8, 9], or RG-invariance. Such a modification is referred to as MWPC in this thesis. In order to achieve RG-invariance at LO, two additional counter terms are promoted from higher order. These additional contact terms act in the $^3P_0$ and $^3P_2$ partial waves. The LO potential may now be represented by

$$V_{\mathrm{LO}}^{\mathrm{MWPC}}(\boldsymbol{p}, \boldsymbol{p}') = V_{\mathrm{LO}}^{\mathrm{WPC}}(\boldsymbol{p}, \boldsymbol{p}') + (C_{^3P_0}\hat{P}_{^3P_0} + C_{^3P_2}\hat{P}_{^3P_2})pp', \tag{3.3}$$

---

[1] Tilde notation is used to differentiate $\widetilde{C}_{^1S_0}$ and $\widetilde{C}_{^3S_1}$ from the LECs $C_{^1S_0}$ and $C_{^3S_1}$ appearing at next-to-leading order (NLO).

where two additional LECs, $C_{^3P_0}$ and $C_{^3P_2}$, have been introduced.

Each of the counter terms of the effective Lagrangian at LO in MWPC is therefore accompanied by an unknown LEC. I now refer back to Chapter 2, where the concept of a model, dependent on a set of unknown parameters, is introduced. χEFT may be considered as such a model which could well represent a physical system with the inclusion of all symmetry-consistent terms. Precision lost due to the truncation of χEFT at a finite order in the chiral expansion can be encapsulated within a model discrepancy term.

Upon possession of estimated parameters, the model may be used for quantitative predictions of nuclear observables. The inference of LECs is therefore a topic of much importance in nuclear physics [26, 27]. Working within a Bayesian framework is a particularly popular approach, as the use of priors on the LECs allows for the inclusion of theoretical beliefs, such as naturalness arguments [6]. In addition, the parameters can be constrained according to an abundance of observational data (e.g. NN scattering observables). Using the NN potential in Eq. (3.3), the Lippmann-Schwinger equation may be solved (see Section 4.4) allowing for the calculation of such scattering observables.

3.2 Model Discrepancy

A model discrepancy arises as a result of the truncation of the chiral expansion. This thesis follows the method of determining the model discrepancy given by Refs. [28, 29]. The truncated χEFT expansion for a predicted observable y_{th} may be written as

$$y_{\text{th}}^{(k)} = y_{\text{ref}} \sum_{\nu=0}^{k} c_\nu Q^\nu, \tag{3.4}$$

where y_{ref} is a reference observable value that sets the scale, c_ν are expansion coefficients, and the truncation is performed at chiral order k. Q is the expansion parameter defined in Eq. (3.1). The truncation at k leads to an error given by

$$\epsilon_{\text{th}}^{(k)} = y_{\text{ref}} \sum_{\nu=k+1}^{K} c_\nu Q^\nu, \tag{3.5}$$

where $K \to \infty$. The expansion coefficients c_ν are unknown but may be assumed to be independent and identically distributed, and equally likely to be positive or negative. As such, we may assume a mean zero Gaussian prior on c_ν, written as

$$c_\nu \sim \mathcal{N}(0, \bar{c}^2), \tag{3.6}$$

where the variance $\bar{c}$ quantifies the magnitude of the coefficient. Conditioning our error $\epsilon_{\text{th}}^{(k)}$ on values for $\bar{c}^2$ and Q allow us to construct the PDF for the error

$$\text{pr}(\epsilon_{\text{th}}^{(k)} | \bar{c}^2, Q, I) = \mathcal{N}(0, \sigma_{\text{th}}^2). \tag{3.7}$$

For the purposes of this thesis, the errors are assumed to be uncorrelated. As in Ref. [30], we now obtain an expression for the model discrepancy variance as

$$\sigma_{\mathrm{th}}^2 = \bar{c}^2 y_{\mathrm{ref}}^2 \frac{Q^{2(k+1)}}{1-Q^2}. \tag{3.8}$$

There are no contributions to the potential at $\nu = 1$, and therefore the first non-zero term in Eq. (3.5) occurs at $\nu = 2$. Therefore, at leading order, $k = 1$ and the model discrepancy variance becomes

$$\sigma_{\mathrm{th}}^2 = \bar{c}^2 y_{\mathrm{ref}}^2 \frac{Q^4}{1-Q^2}. \tag{3.9}$$

Chapter 4

Scattering Theory

In its broadest sense, quantum scattering theory describes a process in which an initial state undergoes an interaction and is transformed into a final state. An important motivation behind studying scattering processes in nuclear physics is to gain insight into the properties of atomic nuclear forces through scattering observables.

In this chapter, the basics of scattering theory are covered. The field of quantum scattering is complex; To do the topic justice, a more comprehensive exploration of the theory is required than is possible in this thesis. Therefore, the topics introduced in the following sections aim to give a brief overview of the theory required for an elementary understanding of how scattering observables are obtained in the case of nucleon-nucleon scattering. A deeper exploration of several concepts may be found in Appendix B. The theory in this chapter primarily follows that given in Refs. [31–33].

4.1 Scattering Cross Sections

We begin by considering the scattering of a single particle with mass m from a potential $V(\boldsymbol{r})$. A complex-valued wavefunction $\psi(\boldsymbol{r})$ is introduced to describe the motion of the particle relative to the target potential. The wave function obeys the time-independent Schrödinger equation,

$$H\left|\psi(\boldsymbol{r})\right\rangle = E\left|\psi(\boldsymbol{r})\right\rangle . \tag{4.1}$$

The Hamiltonian H, in canonical coordinates $\boldsymbol{r}$ and $\boldsymbol{p}$, is

$$H = \frac{\boldsymbol{p}^2}{2m} + V(\boldsymbol{r}) \equiv H_0 + V(\boldsymbol{r}). \tag{4.2}$$

where H_0 is the Hamiltonian in the absence of any interactions. Solutions to Eq. (4.1) are energy eigenstates. There exist two types of state: Bound states and scattering states. Bound states are localised to a region of space and have discretised energies of $E < 0$. In contrast, scattering states are not localised to any region and have $E > 0$. In the case of scattering states, the energy eigenvalues take the form

$$E_{\boldsymbol{k}} = \frac{\boldsymbol{p}^2}{2m}. \tag{4.3}$$

The wave function of a scattering state takes the form

$$\psi(\boldsymbol{r}) = \psi_{\text{incident}} + \psi_{\text{scattered}}. \tag{4.4}$$

This can be interpreted by imagining a plane wave approaching the potential from $\boldsymbol{r} \to -\infty$, scattering off the potential, and 'spreading' out into a spherical wave as $\boldsymbol{r} \to \infty$. The outgoing spherical wave will possess a phase and an amplitude, and thus we can represent the wavefunction as

$$\psi(\boldsymbol{r}) = e^{i\boldsymbol{k}\cdot\boldsymbol{r}} + \frac{f(\theta,\varphi)}{r}e^{ikr}, \tag{4.5}$$

where $f(\theta,\varphi)$ is defined as the *scattering amplitude.* We now introduce the *differential cross section $d\sigma/d\Omega$*, defined as

$$\frac{d\sigma}{d\Omega}d\Omega = \frac{\text{Number of particles scattered into } d\Omega \text{ per unit time}}{\text{Flux of incident particles}}, \tag{4.6}$$

where $d\Omega$ is a solid angle about (θ,φ), and illustrated in Fig. 4.2. The differential cross section can be related to the scattering amplitude by

$$\frac{d\sigma}{d\Omega} = |f(\theta,\varphi)|^2, \tag{4.7}$$

where Ref. [32] can be consulted for a detailed derivation. The *total cross section* σ_{tot} is defined as

$$\sigma_{\text{tot}} = \int |f(\theta,\varphi)|^2 \, d\Omega. \tag{4.8}$$

The aforementioned scattering observables may also be referred to by the SAID nomenclature [34]. In this work we will consider total cross section (SGT), differential cross section (DSG), and polarization of the beam (PB). Details on PB may be found in Ref. [35].

If a spherically symmetric potential is assumed, the system is rotationally invariant. As such, we may choose the direction of the incident wave to be along the z-axis and the scattering problem to now be independent of the azimuthal angle φ. Therefore, calculation of the scattering cross section reduces to the problem of calculating $f(\theta)$.

4.2 Two-Body Scattering

In the previous section, the scattering of only a single particle was considered. The scenario of interest for this thesis is two-nucleon scattering, and therefore the two-body scattering problem must be considered. The problem may be simplified by viewing the elastic scattering of two particles from the centre-of-mass frame of reference, which reduces the problem to that of a single particle scattered by a fixed potential under relative coordinates.

We consider two particles of mass m_1 and m_2, located at positions $\boldsymbol{r}_1$ and $\boldsymbol{r}_2$, respectively. Instead of the particles scattering off one another, the particles may be viewed as undergoing motion due to an interaction potential that depends on the distance between the particles $\boldsymbol{r}_{\textbf{rel}}$ as

$$V(\boldsymbol{r}_1, \boldsymbol{r}_2) = V(\boldsymbol{r}_1 - \boldsymbol{r}_2) = V(\boldsymbol{r}_{\text{rel}}). \tag{4.9}$$

It is convenient to express the masses in terms of the *reduced mass*, defined as

$$\mu = \frac{m_1 m_2}{m_1 + m_2}. \tag{4.10}$$

The relative momentum of the system can be expressed as

$$\boldsymbol{p}_{\text{rel}} = \frac{m_1 \boldsymbol{p}_1 - m_2 \boldsymbol{p}_2}{m_1 + m_2}. \tag{4.11}$$

We also define the total mass M and total momentum $\boldsymbol{P}$ of the system as

$$M = m_1 + m_2, \quad \boldsymbol{P} = \boldsymbol{p}_1 + \boldsymbol{p}_2. \tag{4.12}$$

The Hamiltonian of the two-body system can be written as

$$H = \frac{\boldsymbol{p}_1^2}{2m} + \frac{\boldsymbol{p}_2^2}{2m} + V(\boldsymbol{r}_{\text{rel}}). \tag{4.13}$$

Instead working with the relative and total quantities defined above, the Hamiltonian becomes [36]

$$H = \frac{\boldsymbol{P}^2}{2M} + \left[\frac{\boldsymbol{p}_{\text{rel}}^2}{2m_{\text{rel}}} + V(\boldsymbol{r}_{\text{rel}})\right] \equiv H_{\text{cm}} + H_{\text{rel}}. \tag{4.14}$$

Within the centre-of-mass frame, $\boldsymbol{p}_1 = -\boldsymbol{p}_2$. Since this thesis considers two-nucleon scattering, we introduce the notation μ_{NN} to denote the reduced mass of the two nucleons, each with mass m_{N}, as

$$\mu_{\text{NN}} = \frac{m_{\text{N}} \cdot m_{\text{N}}}{m_{\text{N}} + m_{\text{N}}} = \frac{m_{\text{N}}}{2}. \tag{4.15}$$

We use V_{NN} to represent the potential present in nucleon-nucleon scattering. The Hamiltonian for two-nucleon scattering is therefore given by

$$H = \frac{\boldsymbol{p}_{\text{rel}}^2}{2\mu_{\text{NN}}} + V_{\text{NN}}. \tag{4.16}$$

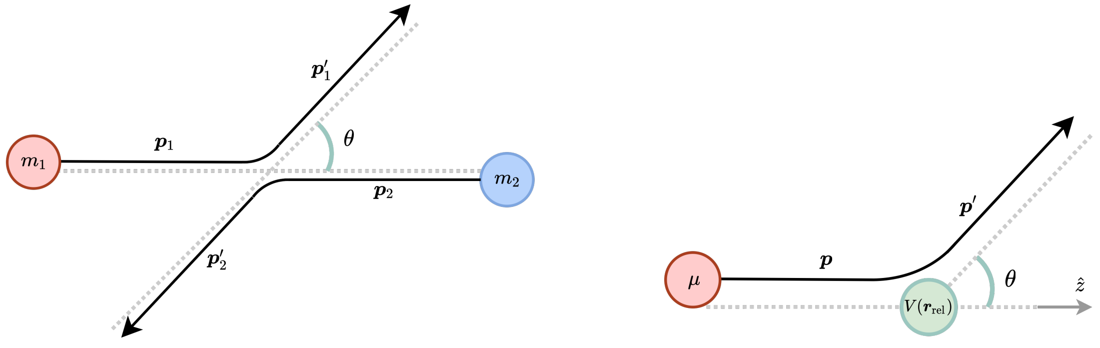

(a) **(b)**

Figure 4.1: Two-body scattering, viewed from the centre-of-mass frame, is shown as equivalent to one-body scattering upon the use of relative coordinates, in (b); An incoming state with relative momentum $\boldsymbol{p}$ is transformed to an outgoing state with relative momentum $\boldsymbol{p'}$ after interaction with a potential $V(\boldsymbol{r}_{\mathrm{rel}})$.

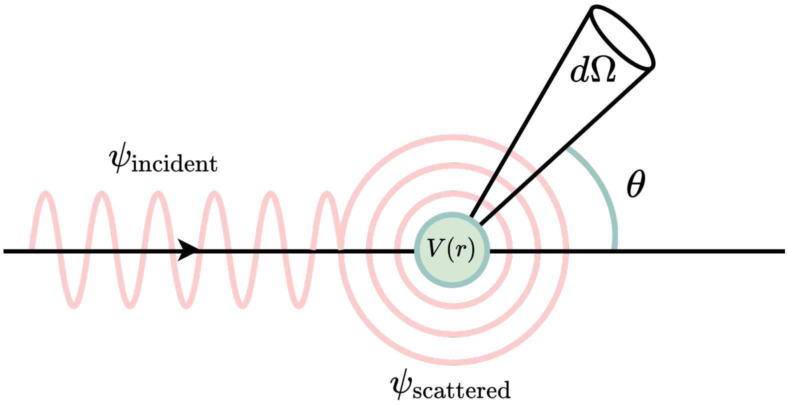

Figure 4.2: Scattering of a single particle from a potential. The wavefunction consists of an incident plane wave and a scattered spherical wave. With a spherically symmetric potential, the azimuthal angle is taken as $\varphi = 0$.

4.3 Partial Wave Expansion

Working in MWPC ensures that the total angular momentum of the system will be conserved by the interaction. However, mixing of different orbital angular momentum components is possible due to the tensor operator. The relevant quantum numbers that we consider in this section are the orbital angular momentum l, the spin s, and the total angular momentum j. The total angular momentum operator is denoted J and obeys

$$J \equiv L + S, \tag{4.17}$$

where L is the orbital angular momentum operator and S is the total spin operator. It therefore follows that [37]

$$|j - s| \leq l \leq j + s. \tag{4.18}$$

Within a two-nucleon system, the total spin operator is given by

$$S = S_1 + S_2, \tag{4.19}$$

where S_1 and S_2 are the spin operators for each of the two nucleons. Since the spin quantum number of a single nucleon is 1/2, it follows that the total spin will take values $s \in \{0, 1\}$ [31].

Due to the conservation of total angular momentum, it is convenient to express our incident wave as a superposition of orbital momentum eigenstates as

$$e^{i\boldsymbol{k}\cdot\boldsymbol{r}} = e^{ikr\cos\theta} = \sum_l (2l+1) i^l j_l(kr) P_l(\cos\theta). \tag{4.20}$$

where $P_l(\cos\theta)$ are Legendre polynomials and $j_l(kr)$ is the spherical Bessel function of order l. The above expression and the following explanations in this section are influenced by Ref. [31], which can be consulted for detailed derivations.

The scattering amplitude $f(\theta, k)$ may also be expanded in terms of partial waves as

$$f(\theta, k) = \sum_{l=0}^{\infty} (2l+1) f_l(k) P_l(\cos\theta), \tag{4.21}$$

where $f_l(k)$ is the *partial-wave amplitude.* Using the above partial wave expansions, the asymptotic form of the wave function, given in Eq. 4.4, can now be expressed as a sum of incoming and outgoing spherical waves as

$$\psi(\boldsymbol{r}) = \sum_l (2l+1) \frac{P_l(\cos\theta)}{2ik} \left[(1 + 2ikf_l(k)) \frac{e^{ikr}}{r} - \frac{e^{-i(kr - l\pi)}}{r} \right]. \tag{4.22}$$

Taking also spin degrees of freedom into account, the spectroscopic notation

$$^{2s+1}l_j \tag{4.23}$$

is used to denote the different scattering channels. The orbital angular momentum l is typically denoted by a letter:

$$l = 0 \Leftrightarrow S, \quad l = 1 \Leftrightarrow P, \quad l = 2 \Leftrightarrow D, \quad ... \tag{4.24}$$

The relevant nucleon-nucleon scattering channels considered in this thesis (see Section 3.1) are:

$$^1S_0 \; : \; s = 0, \; j = 0, \; l = 0 \tag{4.25}$$

$$^3S_1 \; : \; s = 1, \; j = 1, \; l = 0 \tag{4.26}$$

$$^3P_0 \; : \; s = 1, \; j = 0, \; l = 1 \tag{4.27}$$

$$^3P_2 \; : \; s = 1, \; j = 2, \; l = 1 \tag{4.28}$$

Spin-singlet channels are those in which $s = 0$, and spin-triplet are those with $s = 1$. Within nucleon-nucleon interactions, both s and j are conserved. Therefore, obeying

Eq. (4.18), in spin-singlet channels we must have $l = j$, and thus l is also a conserved quantity. Within spin-triplet channels, $l \neq j$ implies that values of initial l and final l' may differ, due to the one-pion exchange tensor interaction [38]. This leads to additional elements within the *S-matrix* — a matrix that contains information on the evolution of an initial state to a final state of a system undergoing scattering. A further explanation of the S-matrix and its role within scattering may be found in Appendix B.1. The S-matrix is typically denoted[1] by S and its partial wave decomposition is expressed using the notation [39]

$$S^{sj}_{ll'}(p', p) = \langle p', l', s, j| \, S \, |p, l, s, j\rangle \, . \tag{4.29}$$

The channels in which non-diagonal ($l \neq l'$) S-matrix elements occur are *coupled channels* [37]. There exist two coupled channels of interest for us:

$$^3S_1 \; - \; ^3D_1 \tag{4.30}$$

$$^3P_2 \; - \; ^3F_2 \tag{4.31}$$

From Eq. (4.22) it is determined that, in the presence of scattering, the incoming wave is unaffected and the outgoing wave changes only in terms of its coefficient. Now taking into account spin, the change in coefficient follows

$$1 \rightarrow 1 + 2ikf^{sj}_l(k). \tag{4.32}$$

We now define the lth diagonal element of the S-matrix as

$$S^{sj}_l \equiv 1 + 2ikf^{sj}_l(k). \tag{4.33}$$

Since the S-matrix is unitary, the diagonal elements must be

$$S^{sj}_l = e^{2i\delta^{sj}_l}, \tag{4.34}$$

where $2\delta_l$ is the phase shift[2]. For an uncoupled channel, there will be a single phase shift. In a coupled channel, the phase shifts will be contained within a 2×2 matrix. This now allows f^{sj}_l to be expressed in terms of δ_l:

$$f^{sj}_l = \frac{e^{2i\delta^{sj}_l} - 1}{2ik}. \tag{4.35}$$

The scattering amplitude is now given by

$$f(\theta, k) = \frac{1}{k} \sum_{l=0} (2l+1) e^{i\delta_l} \sin\delta^{sj}_l P_l(\cos\theta). \tag{4.36}$$

We are now in possession of an expression for $f(\theta)$, allowing the differential cross section $d\sigma/d\Omega$ to be obtained by taking the modulus squared of Eq. (4.37). In accordance with Ref. [31], the total cross section is given as

$$\sigma_{\text{tot}}(k) = \int |f(\theta, k)|^2 \, d\Omega \tag{4.37}$$

$$= \frac{4\pi}{k^2} \sum_l (2l+1) \sin^2\delta^{sj}_{l,s,j} \tag{4.38}$$

---

[1] Note that the S representing the S-matrix is *not* equivalent to the S denoting the total spin operator, nor the S present in the notation for partial waves with $l = 0$.

[2] The factor of 2 is here by convention.

4.4 The Lippmann-Schwinger Equation

It has now been shown that all the information needed to compute scattering cross sections is available from the scattering phase shifts. To calculate phase shifts, we saw that the S-matrix is required. The S-matrix is, in turn, related to the *T-matrix*. To introduce the T-matrix, we must introduce the *Lippmann-Schwinger equation*, which acts as equivalent to the Schrödinger equation in the context of two-nucleon scattering. The Lippmann-Schwinger equation is [40]

$$T(\mathbf{p'}, \mathbf{p}) = V(\mathbf{p'}, \mathbf{p}) + \int d^3\boldsymbol{k}\; V(\mathbf{p'}, \mathbf{k}) \frac{1}{E - E_k + i\epsilon} T(\mathbf{k}, \mathbf{p}). \tag{4.39}$$

A brief explanation of how the above equation is obtained may be found in Appendix B.2.

Solving the Lippmann-Schwinger equation for the T-matrix subsequently allows for the calculation of scattering observables. Therefore, the partial-wave Lippmann-Schwinger equation is useful for this purpose. For the T-matrix and the potential, we introduce the notation

$$T^{sj}_{ll'}(p', p) = \langle p', l', s, j | \, T \, | p, l, s, j \rangle \, . \tag{4.40}$$

$$V^{sj}_{ll'}(p', p) = \langle p', l', s, j | \, V \, | p, l, s, j \rangle \, . \tag{4.41}$$

Note that spin and total angular momentum are conserved in the interaction.

The Lippmann-Schwinger equation in the partial-wave basis can be obtained by performing partial wave expansions of T and V, where Ref. [40] can be referred to for a full derivation. The result is

$$T^{sj}_{ll'}(p', p) = V^{sj}_{ll'}(p', p) + \frac{2}{\pi} \int_0^\infty dk\, k^2\, V(p', k) \frac{1}{E - E_k + i\epsilon} T^{sj}_{ll'}(k, p) \tag{4.42}$$

The S-matrix is defined in terms of the T-matrix as[3] [41]

$$S^{sj}_{ll'}(p', p) = \delta(p' - p) - 2\pi i \delta(E' - E) T^{sj}_{ll'}(p', p). \tag{4.43}$$

4.4.1 Solving the Lippmann-Schwinger Equation

Solving the Lippmann-Schwinger equation, Eq. (B.15) requires repeated iteration of the potential, which subsequently leads to divergent behaviour and an infinite number of terms. Alternatively, the use of numerical methods, such as matrix representation and inversion, may be used to avoid divergences. However, such numerical methods require discretisation and truncation of the integral.

The solution to both of these problems is approached by introducing a cutoff to the the potential. The treatment of the cutoff, examined further in Ref. [6], involves

---

[3] Several alternative definitions exist. A discussion may be found in [41].

the introduction of a regulator function $f(p', p)$ as a function of a cutoff parameter Λ. It is multiplied with V to give

$$V(\boldsymbol{p}', \boldsymbol{p}) \rightarrow V(\boldsymbol{p}', \boldsymbol{p}) f(p', p). \tag{4.44}$$

$f(p', p)$ is generally chosen to be of the form of an exponential

$$f(p', p) = \exp\Bigg[- (p'/\Lambda)^{2n} - (p/\Lambda)^{2n} \Bigg], \tag{4.45}$$

where n is a chosen cutoff power. Results obtained when solving for the T-matrix will obviously be sensitive to the choice of regulator function and Λ. However, it is not desirable that predictions of scattering observables depend on such choices. They should rather be renormalisation group (RG)-invariant. Consequently, the LECs must account for the introduction of a regulator, and they will therefore be dependent on Λ.

A numerical method for solving the Lippmann-Schwinger equation is that of matrix inversion. Such a method involves the use of Gaussian quadrature, where an integral of a function is expressed as a weighted summation of the function. The Lippmann-Schwinger equation expressed in this form is

$$T^{sj}_{ll'}(p', p) = V^{sj}_{ll'}(p', p) + \frac{2}{\pi} \sum_{ll'} \sum_{i=1}^{n} w_i k_i^2 \; V(p, k_i) \frac{2m}{p^2 - k_i^2 + i\epsilon} T^{sj}_{ll'}(k_i, p), \tag{4.46}$$

with k_i and w_i representing momenta $\{k_i\}_{i=1}^{N_p}$ and weights $\{w_i\}_{i=1}^{N_p}$, respectively, for a polynomial mesh. In our case, we consider a Gauss-Legendre mesh. N_p is the number of momentum-grid points, chosen high enough such that the solution is converged. Further details on the approach may be found in Ref. [39, 40].

Part II

Implementation

Chapter 5

Defining the Non-Implausible Volume

A new batch of samples must be generated in each wave of a history match. They are generated within an increasingly smaller parameter space and according to some criteria imposed by the non-implausible samples of the previous wave. Two problems must therefore be addressed:

- In a high-dimensional parameter space, how do we avoid an exponential increase in the number of samples with dimension?
- How do we generate a new set of samples within a wave, based on the set of non-implausible samples obtained in the previous wave?

We first address the problem of generating samples in a high-dimensional space. This is often expressed as the *curse of dimensionality.* One of two opposing obstacles are encountered in such a situation; An increase in the dimensionality of the parameter space can lead to an exponential increase in the number of samples [42], resulting in a high computational cost. Conversely, if the number of samples is kept constant, there will be a growing sparsity of samples. In the case of history matching, this sparsity may lead to a failure to locate particularly small non-implausible regions. One approach to combat the 'curse' is the generation of samples using a space-filling design, where samples are characterised as *well-spaced.* In an intuitive sense, samples are seen as well-spaced if no point in parameter space is too far from a sample. Latin hypercube (LH) sampling is introduced as one example of a space-filling design and is the sampling method implemented in this thesis. Details of its implementation, amongst other such designs and their characterisations of well-spaced, may be found in Ref. [43].

In the case of LH sampling, N samples are generated within a d-dimensional unit hypercube, where each sample is a vector $\boldsymbol{x}_i \in [0,1]^d$, $i = 1, 2, ..., N$. This now directs attention to the second problem: Which properties of the previous wave's non-implausible samples do we use to impose conditions on the generation of new samples? In other words, how can we transform a set of samples, located within a unit hypercube, such that the samples lie within the parameter space that contains the non-implausible samples of the previous wave. Furthermore, how do we apply such properties to the chosen space-filling design? The problem is addressed by introducing the concept of a *non-implausible volume*. It is here important to note that we define the non-implausible volume in two related, but distinct, ways:

1. A bounding volume located in parameter space. This volume encloses the set of non-implausible samples obtained at the end of a wave. This is defined to quantify volume reduction and to aid visualisation.
2. A method of generating samples in a wave based on the non-implausible volume obtained in the previous wave.

Throughout this chapter, it will be explained how the former definition allows us to construct the sampling method given in the latter definition. Here we will discuss four different options for defining the non-implausible volume.

5.1 The Hyperrectangle

Often in history matching literature [10, 11, 17], the volume is defined by simply determining upper and lower boundaries for each input parameter. The boundaries can easily be determined in each wave by identifying the minimum and maximum parameter coordinate in each dimension among the non-implausible samples of the previous wave. The non-implausible volume can then be defined as the parameter space that lies within these limits, and will be of hyper-rectangular shape, i.e, an orthotope..

Generating samples according to such a volume is straightforward; N samples are generated using a space-filling design within a d-dimensional space, where each sample is a vector $\boldsymbol{x}_i \in [0,1]^d$, $i = 1, 2, ..., N$. It is then trivial to transform the samples according to the parameter boundaries. A two-dimensional hyperrectangle bounding volume, constructed around a set of non-implausible samples, is illustrated in Fig. 5.1.

5.2 The Rotated Hyperrectangle

Correlations between parameters may exist within a model. Quantitatively, the correlation is characterised by the covariance. The pairwise relationship between a set of two-dimensional non-implausible parameter samples can also be visualised, as shown in Fig. 5.1. This correlation information is lost upon the construction of a hyperrectangle bounding volume enclosing the samples, that is parallel to the parameter directions. Accounting for correlations therefore motivates the introduction of another non-implausible volume — a *rotated* hyperrectangle.

A $d \times d$ covariance matrix $\boldsymbol{\Sigma}$ represents the covariance between parameters in a d-dimensional parameter space. An eigendecomposition of $\boldsymbol{\Sigma}$ may be obtained as

$$\boldsymbol{\Sigma} = \boldsymbol{V}\boldsymbol{\Lambda}\boldsymbol{V}^T. \tag{5.1}$$

Where $\boldsymbol{\Lambda}$ is the diagonal matrix of eigenvalues λ_i and $\boldsymbol{V}$ is the $d \times d$ matrix where the columns are eigenvectors of $\boldsymbol{\Sigma}$. The eigenvectors represent the directions of the largest variance in each dimension. Since $\boldsymbol{\Sigma}$ is a symmetric matrix, the eigenvectors are orthogonal unit vectors and $\boldsymbol{V}$ can be thought of in terms of a rotation matrix. The eigenvalues corresponding to the eigenvectors represent the magnitude of each variance. $\sqrt{\boldsymbol{\Lambda}}$ therefore acts as a scaling matrix. This enables a transformation matrix to be defined as

$$\boldsymbol{T} = \boldsymbol{V}\sqrt{\boldsymbol{\Lambda}}. \tag{5.2}$$

The extraction of $\boldsymbol{T}$ now allows for the rotation and scaling of a set of samples generated using the space-filling design. To generate a *new* set of samples, a unit hypercube of space-filling samples is generated. This is transformed such that the samples are centred on 0: $\boldsymbol{x}_i \in [-1, 1]^d$. The covariance matrix of the set of non-implausible samples obtained in the *previous wave* is computed and $\boldsymbol{T}$ is obtained. The transformation matrix is then applied to each of the *new* set of samples $\boldsymbol{\theta}_i = \boldsymbol{T}\boldsymbol{x}_i$. This is the set of samples to be used within the new wave of the history match. The bounding volume of this set of samples takes the shape of a rotated hyperrectangle, as represented in Fig. 5.1.

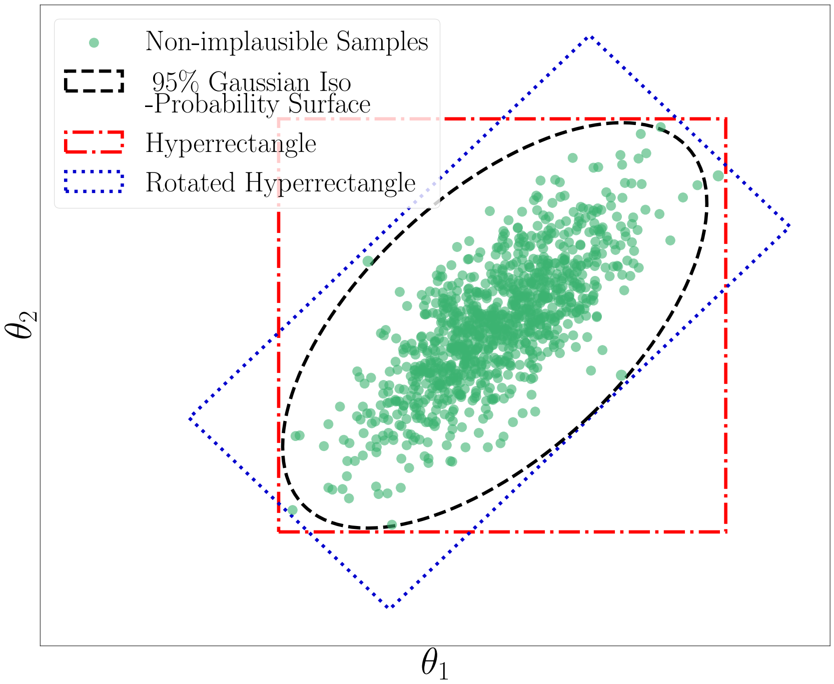

Figure 5.1: A two dimensional representation of the boundaries of non-implausible volumes defined as a hyperrectangle, a rotated hyperrectangle, and a 95% Gaussian iso-probability surface. The non-implausible volumes shown were constructed using the plotted non-implausible samples, shown as green circles. Note that an ellipsoid non-implausible volume would have identical boundaries to the 95% Gaussian iso-probability surface and only differ in the distribution of new samples within the volume.

5.3 The Gaussian

Since the construction of a rotated hyperrectangle requires a covariance matrix and mean for a set of non-implausible samples, it is also viable to define an alternative non-implausible volume in the form of a multivariate Gaussian distribution. It must be noted that this volume-type differs from the others in the sense that a Gaussian alone does not constitute a bounding volume. We refer back to the non-implausible volume definitions and note that when referring to the Gaussian volume, we henceforth refer to:

- A bounding volume defined by the 95% iso-probability surface of the multivariate Gaussian distribution.
- A method of generating multivariate Gaussian distributed samples.

In order for all probability mass to be contained within the Gaussian, an integral over infinite limits is required. Therefore a 95% iso-probability surface is constructed as a practical approach to define the bounding volume within this thesis. The 95% iso-probability surface will be used for visual representation and volume calculations. However, this is no way a hard constraint on the non-implausible volume since the Gaussian volume is defined only by its covariance and mean. Information on the non-implausible parameter space excluded by the 95% limit is therefore not lost. See Section 5.4 for a description of the construction of an iso-probability surface.

The motivation behind such a volume definition is primarily to allow correlations between parameters to be captured more precisely. However, there is the potential for a further benefit to be tested upon implementation; There may not exist non-implausible samples located in all regions of the parameter space contained within a hyperrectangle bounding volume. Instead, a hyperrectangle could still include regions of *implausible* parameter space. One may refer to Fig. 5.1, where these regions lie at the corners of the rotated hyperrectangle. Consequently, this could lead to an increased number of waves in the history match due to the repeated resampling of these implausible areas. Furthermore, the final non-implausible parameter volume obtained through history matching could be larger than the optimal parameter volume. Defining a Gaussian non-implausible volume potentially accounts for this issue and motivates a comparison between volume types within this thesis.

It is straightforward to transform a set of space-filling samples to be normally distributed using inverse transform sampling. Only a mean $\boldsymbol{\mu}$ and a covariance matrix $\boldsymbol{\Sigma}$ is required. The method is given in Algorithm 1.

An illustration of the 95% iso-probability surface of a Gaussian non-implausible volume may be found in Fig. 5.1.

Algorithm 1 Generation of well-spaced samples with a multivariate Gaussian distribution.

```
Input: $\boldsymbol{\Sigma}$ (Covariance matrix), $\boldsymbol{\mu}$ (Mean)
  1. Generate $N$ well-spaced samples $\boldsymbol{x}_i$, $i = 1, 2, ..., N$. Each sample $\boldsymbol{x}_i$ is a $d$-dimensional coordinate $(x_1, x_2, ..., x_d)$ in parameter space, where $x_j \in [0, 1]$, $j = 1, .., d$.
  2. Transform samples according to $\boldsymbol{u}_i = F_u^{-1}(\boldsymbol{x_i})$, where $F_u^{-1}$ is the inverse cumulative distribution function.
  3. Compute the Cholesky decomposition $\boldsymbol{L}$ of the covariance matrix $\boldsymbol{\Sigma} = \boldsymbol{L}\boldsymbol{L}^T$. Note that, to ensure numerical stability when computing the Cholesky decomposition, it may be required to add a small multiple of the identity matrix to $\boldsymbol{\Sigma}$ [20].
  4. Return $\boldsymbol{\theta}_i = \boldsymbol{\mu} + \boldsymbol{L}\boldsymbol{u}_i$
```

5.4 The Ellipsoid

History matching is a likelihood-free method. The implausibility measure is used only to impose an implausibility cut-off and the exact implausibility value that a sample in parameter space receives is not a reflection of how ‘plausible’ the sample may be. However, generating Gaussian-distributed samples does, by definition, constitute a bias towards the mean of the previous wave’s non-implausible samples. Within a Gaussian, there exists a higher density of samples close to the mean. This could lead to more non-implausible samples found near the mean, despite this region of parameter space being no more ‘plausible’ than any other region. Theoretically, this could also cause the mean of the Gaussian volume to resist changing in subsequent waves even if the ‘true’ non-implausible region shifts in position (due to the introduction of additional parameters or observables).

To avoid bias and yet still retain the ability to capture correlations, samples may be instead generated to be uniformly well-spaced within an ellipsoid. The ellipsoidal volume is therefore defined such that there is no higher density of samples in any particular region (no bias at the mean). The sample generation method chosen within this thesis requires points to be generated on the surface of a multidimensional sphere [44] — steps 1-2 of Algorithm 2. These points are then redistributed radially and transformed according to a covariance matrix [45], performed in steps 3-6 of Algorithm 2. Only the covariance matrix $\boldsymbol{\Sigma}$ and the mean $\boldsymbol{\mu}$ of a set of non-implausible samples are needed.

Therefore, the ellipsoid non-implausible volume differs only from the Gaussian in the sense that the samples lying within the 95% iso-probability surface of the Gaussian are transformed such that they are well-spaced. The bounding volume for both types of non-implausible volumes is therefore identical.

In order to explain how samples are generated within an ellipse, it is instructive to first introduce how the 95% iso-probability surface is obtained. The confidence-ellipsoid for a Gaussian distribution $\mathcal{N}(\boldsymbol{x};\boldsymbol{\mu},\boldsymbol{\Sigma})$ is defined as

$$(\boldsymbol{x}-\boldsymbol{\mu})^T\boldsymbol{\Sigma}^{-1}(\boldsymbol{x}-\boldsymbol{\mu}) = c^2. \tag{5.3}$$

Values of $\boldsymbol{x}$ that fulfill this ellipsoid equation have equal probability density. One therefore wishes to choose a value of c such that the ellipsoid boundary defines a contour of a given constant probability density, or an *iso-probability contour.* We define the probability that a value of $\boldsymbol{x}$ lies within the ellipsoid, for a given value of c, to be $(1-\alpha)$. This allows us to write

$$\Pr\Big\{(\boldsymbol{x}-\boldsymbol{\mu})^T\boldsymbol{\Sigma}^{-1}(\boldsymbol{x}-\boldsymbol{\mu}) \leq c^2\Big\} = 1-\alpha, \tag{5.4}$$

where c^2 is the squared Mahalanobis distance, known to have a chi-square distribution with d degrees of freedom [46]. $\chi^2_{d,\alpha}$ can therefore replace c^2 as follows:

$$\Pr\Big\{(\boldsymbol{x}-\boldsymbol{\mu})^T\boldsymbol{\Sigma}^{-1}(\boldsymbol{x}-\boldsymbol{\mu}) \leq \chi^2_{d,\alpha}\Big\} = 1-\alpha. \tag{5.5}$$

In other words, $100(1-\alpha)\%$ of the Gaussian-distributed samples will be contained within the ellipsoid defined as

$$(\boldsymbol{x}-\boldsymbol{\mu})^T\boldsymbol{\Sigma}^{-1}(\boldsymbol{x}-\boldsymbol{\mu}) = \chi^2_{d,\alpha}. \tag{5.6}$$

To obtain the 95% iso-probability surface, we set c^2 to be equal to a critical value of the chi-squared distribution $\chi^2_{d,\alpha}$ where $\alpha = 0.05$. Values for $\chi^2_{d,0.05}$ may be easily obtained by consulting a Chi-Square distribution table [47], given the degrees of freedom d (the dimensionality of $\boldsymbol{x}$ in this case). Equipped with $\chi^2_{d,0.05}$, well-spaced samples may be generated within a hyper-ellipsoid according to Algorithm 2.

Algorithm 2 Generation of well-spaced samples within an ellipsoid

```
Input: $\boldsymbol{\Sigma}$ (Covariance matrix), $\boldsymbol{\mu}$ (Mean), $\chi^2_{d,\alpha}$ (Critical value of the Chi-Square distribution at $\alpha$ for $d$ degrees of freedom).
  1. Generate $N$ well-spaced multivariate Gaussian samples $\boldsymbol{v}_i$, $i = 1, 2, ..., N$. Each sample $\boldsymbol{v}_i$ is a $d$-dimensional coordinate $(v_1, v_2, ..., v_d)$ in parameter space.
  2. For each sample $\boldsymbol{v}_i$, compute the $\ell^2$-norm $|\boldsymbol{v}_i| = \left(\sum_{k=1}^{d} v_k^2\right)^{1/2}$ and return $\boldsymbol{u}_i = \boldsymbol{v}_i/|\boldsymbol{v}_i|$.
  3. Generate $N$ well-spaced scalar points $r_i = i \cdot \Delta x$, $i = 1, 2, ..., N$. $\Delta x = 1/N$.
  4. Compute $\boldsymbol{y}_i = \boldsymbol{u}_i r_i^{1/d}$.
  5. Compute the Cholesky decomposition $L$ of the covariance matrix $\boldsymbol{\Sigma} = \boldsymbol{L}\boldsymbol{L}^T$.
  6. Return $\boldsymbol{\theta}_i = \chi_{d,\alpha}(\boldsymbol{L}\boldsymbol{y}_i) + \boldsymbol{\mu}$.
```

5.4.1 Space-Filling Design Metric

To ensure that the ellipsoid samples fulfill the requirement to be well-spaced, both qualitative and quantitative assessments are performed. A set of $N = 1000$ samples from a two-dimensional ellipsoid, defined by the mean and (arbitrary) covariance matrix

$$\mu = (0, 0), \qquad \Sigma = \begin{pmatrix} a & b \\ b & c \end{pmatrix}, \tag{5.7}$$

were generated using Algorithm 2. In addition, a separate set of $N = 1000$ samples were generated following the same procedure yet with the samples $\boldsymbol{v}_i$ in step 1 of Algorithm 2 generated randomly, rather than with a space-filling design. The proposal is that samples generated via a space-filling design for $\boldsymbol{v}_i$ will demonstrate well-spaced behaviour in the ellipsoid. Samples generated with $\boldsymbol{v}_i$ taken as random (independently sampled) should display behaviour indicating otherwise.

A plot of the samples obtained in both cases can be found in Fig. 5.2. Upon visual inspection, the samples obtained using a space-filling design seem relatively well-spaced in contrast with the samples obtained through random sampling, which appear to cluster at the edges.

To perform a quantitative numerical test upon the samples, the *joint* Shannon entropy of two discrete variables X, Y [48] is introduced as

$$H(X,Y) = \sum_{x\in X}\sum_{y\in Y} P(x,y)\log_2\left(\frac{1}{P(x,y)}\right), \tag{5.8}$$

where x and y are samples from X and Y. $P(x,y)$ is the joint probability of x and y occurring simultaneously. One can relate the discrete variables X and Y to the situation at hand by constructing a grid of cells within which samples lie. Each cell has width $(\Delta x, \Delta y)$ and is denoted by $(\hat{x}, \hat{y})$, where $\hat{x}$ and $\hat{y}$ are discrete values corresponding to the coordinates at the centre of the respective cell. Each cell may then be assigned a probability defined as the number of samples that lie within the cell divided by the total number of samples. The cells lying at the boundary of the ellipse will only partially contain samples; Evaluating a probability over the entirety of the cell would therefore imply a density of samples lower than the true value. To avoid the resulting effect on the entropy, the cells lying both outside and on the boundary of the defined ellipse are removed in this study. This also ensures that the probability distribution for each ellipse is computed over the same number of cells. The grid and corresponding probabilities for each cell are shown in Fig. 5.3.

The benefit of such a method is that it allows for the calculation of an ‘optimum’ entropy value — the maximum entropy. Maximum entropy occurs in the case of a uniform probability distribution, analogous to perfectly uniform samples across the parameter space. Therefore, the greater $H(X,Y)$ value obtained, the more well-spaced the samples are.

The described two-dimensional sets of samples were each generated 5000 times and the entropy calculated for each set. The mean entropy obtained using a space-filling design was calculated to be $\bar{H}^{(2D)}_{\text{lhs}} = 7.76$. In comparison, the mean entropy obtained using random sampling was found to be $\bar{H}^{(2D)}_{\text{rand}} = 7.49$. The maximum entropy is calculated to be $H^{(2D)}_{\text{max}} = 8.64$ bits. A histogram of the entropy values in each case is shown in Fig. 5.4. Similarly, the entropy was obtained for 5000 sets of $N = 10^6$ four-dimensional samples, now using a four-dimensional joint Shannon entropy. Values obtained are $\bar{H}^{(4D)}_{\text{rand}} = 14.5$ bits, $\bar{H}^{(4D)}_{\text{lhs}} = 15.0$ bits, and $H^{(4D)}_{\text{max}} = 17.3$ bits.

The higher entropy values obtained using a space-filling design in both the two- and four-dimensional examples confirm that it produces samples more well-spaced than the case of random sampling. Maximum entropy is not reached, which is unsurprising since generating space-filling samples using LH sampling is still a technique involving sample randomisation within grid cells [49]. Evidence of this randomisation is present in Fig. 5.2, where small clusters of samples may be seen in the space-filling case. Maximum entropy would, most likely, not be reached unless in the case of uniform sampling. As described earlier in the chapter, this approach is not feasible as uniformly spaced samples grow too sparse with an increase in the dimensionality of parameter space.

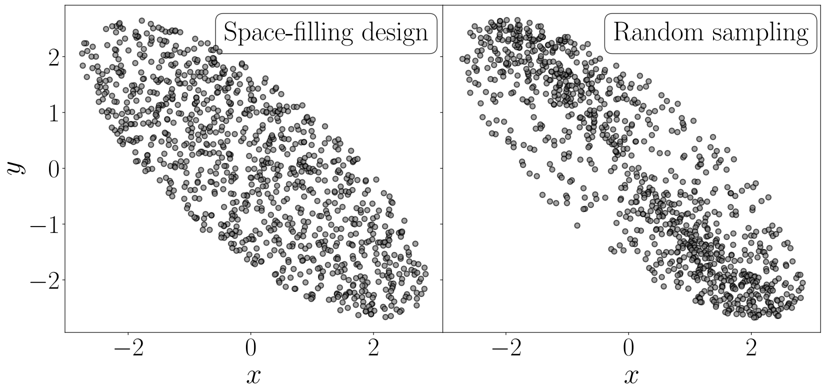

Figure 5.2: $N = 1000$ two-dimensional samples generated using a well-spaced ellipsoidal sampling method (on the left) and random ellipsoidal sampling (on the right). Areas of higher sample density are seen when implementing random sampling.

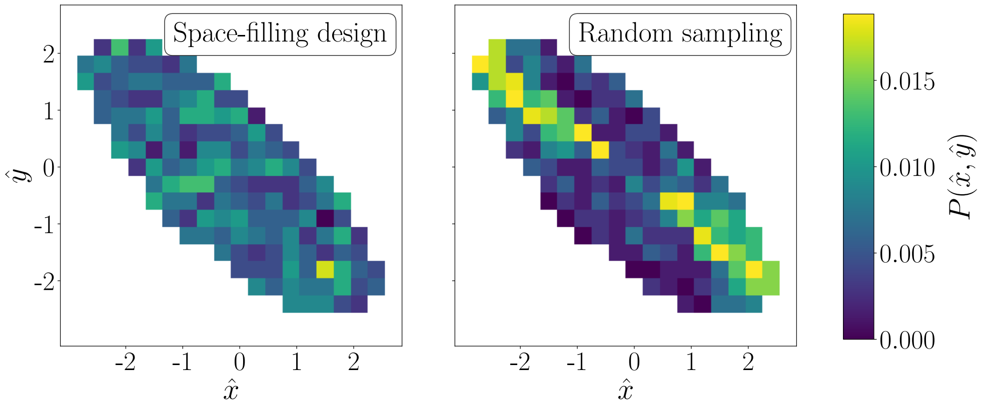

Figure 5.3: Two-dimensional probability distributions of $N = 1000$ samples generated using a well-spaced ellipsoidal sampling method (on the left) and random ellipsoidal sampling (on the right). The discrete joint probability $P(\theta_1, \theta_2)$ is evaluated over cells of a grid. Note the higher contrast in areas of low and high probability when using random sampling.

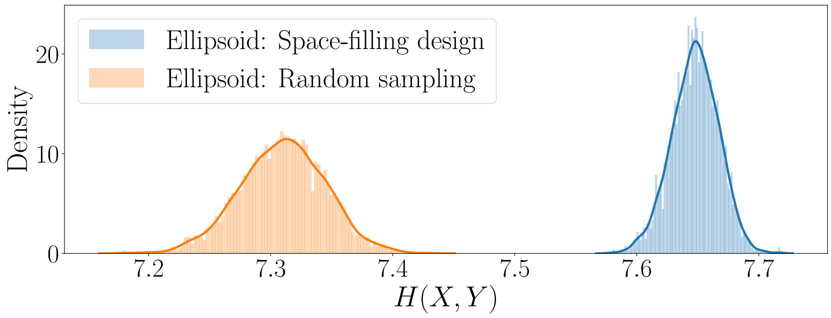

Figure 5.4: Normalised histograms of joint entropy $H(X, Y)$ values obtained for 5000 sets of $N = 1000$ two-dimensional samples generated using a space-filling design and 5000 sets of $N = 1000$ two-dimensional samples generated using random sampling.

Chapter 6

Toy Model

6.1 Parameter Posterior Distributions

Before the application of a challenging method to a problem, there is value in first validating the method. In order to validate the history matching framework developed in this thesis, a toy model is used. The toy model is chosen such that there is a simple linear dependence on model parameters $\boldsymbol{\theta}$. This linear dependence allows for a ordinary least squares (OLS) regression to be performed so to obtain a set of optimum parameters $\boldsymbol{\theta}^*$.

According to Bayes' theorem, the posterior distribution for $\boldsymbol{\theta}$ may be expressed as

$$p(\boldsymbol{\theta}|\mathcal{D}) \propto p(\mathcal{D}|\boldsymbol{\theta})p(\boldsymbol{\theta}), \tag{6.1}$$

where $\mathcal{D}$ is the set of data. Assuming a uniform prior, i.e. the prior's contribution to the posterior is independent of $\boldsymbol{\theta}$ in a certain range, we obtain:

$$p(\boldsymbol{\theta}|\mathcal{D}) \propto p(\mathcal{D}|\boldsymbol{\theta}). \tag{6.2}$$

Assuming a uniform prior, finding the maximum a posteriori (MAP) estimator for $\boldsymbol{\theta}$ is analogous to finding the OLS estimator $\boldsymbol{\theta}^*$. We therefore motivate performing an OLS regression on the toy model as a method to obtain a posterior distribution for $\boldsymbol{\theta}$. Before the toy model itself is introduced, the procedure for obtaining the posterior will be outlined. We introduce a model consisting of a functions of which each function output is dependent on an independent variable x_i, a vector of input parameters $\boldsymbol{\theta}$, and related to an observational datapoint z_i with the inclusion of an uncertainty ϵ_i:

$$z_i = f(x_i, \boldsymbol{\theta}) + \epsilon_i. \tag{6.3}$$

Where ϵ_i may be a sum of independent errors and the variance of ϵ_i is $\sigma_{\epsilon_i}^2$. The function has been chosen to be linearly dependent on $\boldsymbol{\theta}$ and can therefore be written as a linear superposition. This allows us to write

$$f(x_i, \boldsymbol{\theta}) = \sum_{j=1}^{M} \theta_j g_{i,j}(x_i), \tag{6.4}$$

where M is determined by the truncation of the model, and corresponds to the number of model parameters. Each $g_{i,j}$ is a deterministic function of x_i and together form the set of basis functions. We define data and parameter vectors as

$$\boldsymbol{z} = [z_1, z_2, ..., z_N] \tag{6.5}$$

$$\boldsymbol{\theta} = [\theta_1, \theta_2, ..., \theta_M]. \tag{6.6}$$

We also define the $N \times M$ design matrix as

$$\boldsymbol{G} = \begin{bmatrix} g_{1,1} & g_{1,2} & \cdots & g_{1,M} \\ g_{2,1} & g_{2,3} & \cdots & g_{2,M} \\ \cdots & \cdots & \cdots & \cdots \\ g_{N1,} & g_{N,2} & \cdots & g_{N,M} \end{bmatrix}. \tag{6.7}$$

An $N \times N$ matrix $\boldsymbol{\Sigma}$ is constructed as $\Sigma = \text{diag}(\boldsymbol{\sigma}^2)$, where $\boldsymbol{\sigma}^2 = [\sigma_1^2, \sigma_2^2, ..., \sigma_N^2]$ is the vector of the uncertainty variances for each model output. We can now define the χ^2 function as

$$\chi^2(\boldsymbol{\theta}) = \frac{1}{N}\left\{\Big(\boldsymbol{z} - \boldsymbol{f}(\boldsymbol{\theta})\Big)^T \boldsymbol{\Sigma}^{-1}\Big(\boldsymbol{z} - \boldsymbol{f}(\boldsymbol{\theta})\Big)\right\}. \tag{6.8}$$

In order to find the optimal parameters, χ^2 is minimised with respect to $\boldsymbol{\theta}$. This may be represented as

$$\left.\frac{\partial \chi^2}{\partial \boldsymbol{\theta}}\right|_{\boldsymbol{\theta}=\boldsymbol{\theta}^*} = 0 \tag{6.9}$$

Since the parameters enter linearly in $\boldsymbol{f}(\boldsymbol{\theta})$, the obtained solution is

$$\boldsymbol{\theta}^* = \Big(\boldsymbol{A}^T\boldsymbol{A}\Big)^{-1}\boldsymbol{A}^T\boldsymbol{b}. \tag{6.10}$$

Where $\boldsymbol{A} = \boldsymbol{G}\boldsymbol{\Sigma}^{-1/2}$ and $\boldsymbol{b}$ is a vector containing elements $b_i = z_i/\sigma$. The covariance matrix for the optimum set of parameters $\boldsymbol{\theta}^*$ is defined as

$$\boldsymbol{H} = \Big(\boldsymbol{A}^T\boldsymbol{A}\Big)^{-1}. \tag{6.11}$$

Upon possession of $\boldsymbol{\theta}^*$ and the matrix $\boldsymbol{H}$, we may construct an analytically obtained posterior that is proportional to a multivariate Gaussian. This may be formulated as

$$p(\boldsymbol{\theta}|\mathcal{D}) \propto \mathcal{N}(\boldsymbol{\theta}^*, \boldsymbol{H}) \tag{6.12}$$

where $D \equiv \boldsymbol{z}$ is the set of data. We are now able to formulate the goal of the toy model validation — To confirm that the non-implausible volume obtained as a result of the history match contains the optimum set of parameters $\boldsymbol{\theta}^*$. It is also desirable that the 3σ region of the analytical posterior falls within the non-implausible region. Additionally, the analytical posterior allows for confirmation that the correct correlations are captured within the non-implausible volumes (when possible).

6.2 The Liquid Drop Model

As outlined above, we seek a toy model that has linear dependence on model parameters. Additional desirable features include a set of observational data corresponding to model outputs, and quantifiable uncertainty variances. The liquid drop model [50] fulfills these criteria. It is a simple yet useful model used within nuclear physics to approximate the binding energy E_{B} of nuclei. The model is a function of the number of nucleons in an atomic nucleus A, the number of protons Z, and the number of neutrons N. The function is linearly dependent on a set of coefficients, and is given by

$$E_{\mathrm{B}}(N,Z) = a_{\mathrm{v}}A + a_{\mathrm{s}}A^{2/3} + a_{\mathrm{c}}\frac{Z^2}{A^{1/3}} + a_{\mathrm{a}}\frac{(N-Z)^2}{A} + a_{\mathrm{p}}\delta. \tag{6.13}$$

A brief description of the terms is as follows:

Volume Term

The first term, $a_{\mathrm{v}}A$, is the *volume term*. Since the nuclear radius grows as $r \propto A^{1/3}$, and volume grows as $V \propto r^3$, it can be said that $V \propto A$. This relation motivates the naming of this term. The term is motivated by the short range of the strong nuclear force where nucleons interact only with their nearest neighbours.

Surface Term

The *surface term*, $a_{\mathrm{s}}A^{2/3}$, acts as a correction to the volume term. The volume term operates on the assumption that all nucleons interact with the same number of neighbours. In reality, nucleons on the surface on the nucleus have fewer nearest neighbours than those in the centre. This leads to reduction in binding energy. Since the volume is determined to be proportional to A, the surface term must be proportional to the surface area, $A^{2/3}$.

Coulomb Term

The *Coulomb term*, $a_{\mathrm{c}}Z^2/A^{1/3}$, arises due to the Coulomb repulsion between pairs of protons. The electrostatic potential energy is inversely proportional to the radius of a sphere, giving rise to the term's proportionality to $A^{-1/3}$. The factor Z^2 may also be written as a sum over all pairs of interacting protons

$$\sum_{i=1}^{Z}\sum_{j\neq i} Z_i \cdot Z_j, \tag{6.14}$$

which reduces to $Z(Z-1) \approx Z^2$ for large Z.

Asymmetry Term

The *asymmetry term*, $a_{\mathrm{a}}(N-Z)^2/A$, accounts for imbalances between the number of protons, Z, and the number of neutrons, N. Since some nuclei, typically heavier ones, will contain more neutrons than protons, the repulsion described in the *Coulomb term* will be counteracted by attractive proton-neutron interactions. However, an imbalance between the proton and neutron numbers results in the neutrons occupying higher energy levels than the protons due to the Pauli exclusion principle.

This leads to an increase in energy.

Pairing Term
Finally, the *pairing term* $a_\mathrm{p}\delta$ is introduced so to account for the tendency of like nucleons to couple into pairs, leading to a stable nucleus. The term can be defined as

$$\delta = \begin{cases} A^{-1/2} & \text{if Z, N even,} \\ 0 & \text{if A=Z+N odd,} \\ -A^{-1/2} & \text{if Z, N odd.} \end{cases} \tag{6.15}$$

The first case above corresponds to the fact that, if the proton and neutron numbers are even, both protons and neutrons can form pairs. The second case, where $A = Z + N$ is odd, implies that either Z is even and only protons can form pairs, or N is even and only neutrons can form pairs. In the third case, neither protons nor neutrons can form pairs.

The Atomic Mass Evaluation 2016 (AME2016) [51] contains experimental data for the binding energy per nucleon E_B/A for a wide range of nuclei and provides the observables to be used within the history match of the liquid drop model.

6.3 Emulation of the Liquid Drop Model

The liquid drop model is neither complex nor computationally expensive to evaluate. Generally, an emulator would not be needed in the case of this model. However, the purpose of performing a history match upon the liquid drop model is validation of the method. Since the use of an emulator is often integral to the history matching method, it is thought beneficial to the validation to include an emulator at this stage also.

To emulate the liquid drop model in this work, the approach models the global behaviour of the function as a polynomial — see Eq. (2.12). Since the model in question is linearly dependent on $\boldsymbol{\theta}$, constructing a first-order polynomial would quickly lead to successful output predictions. However, the Bayes Linear approach also includes a Gaussian process term, $u_i(\theta_i)$, to model local behaviour in the model. A further discussion of the method takes place in in Section 2.2.2. In the case of the liquid drop model, this term would be of little use after performing a first order linear regression. In order to better test the capabilities of the Gaussian process — important for application of the scheme to more complex models — a zeroth order regression is performed. The outcome provides a mean and variance of the training output that then allows $u_i(\theta_i)$ to capture deviations from the mean.

Since the liquid drop model is a continuous function, the simplest choice of covariance function within the Gaussian process emulator is that of the squared exponential kernel, defined in Eq. (2.7). The covariance function is dependent on two hyperparameters: the length-scale ℓ and the signal variance σ_f^2. Varying the hyperparameters can affect the predictions of the emulator dramatically and so must be chosen with care. Since the liquid drop model is a relatively simple model, we expect the emulator to be fairly accurate. We therefore consider a single correlation length for all parameters. In the case of more complex models, considering different correlation lengths in each dimension may be preferred.

Since $u_i(\theta_i)$ models local behaviour, a simple and intuitive choice for σ_f^2 is the residual variance of the zeroth-order linear regression. This choice of signal variance is inspired by the methodology given in Ref. [17].

6.3.1 Inactive Input Parameters

The liquid drop model is constructed such that successive terms are corrections to the volume term. This allows the binding energy to be calculated, albeit less accurately, if latter terms in the model are neglected. In the case of history matching, this allows either one or a set of *inactive* parameters to be defined during initial waves. The aim of doing so is to explain the dominant variation in model output by as few parameters as possible. This reduces the dimensionality of the model; Computational cost is lessened and thus denser sampling may be achieved. The inactive parameters may then be introduced in later waves so that small variations in the model output are accounted for and non-implausible parameter volumes adjusted accordingly.

The linear nature of the liquid drop model and the relatively simple physical principles that govern the model imply that a_p is the sensible choice for an inactive parameter. Fig. 6.1 shows a diagnostic plot used to justify such a choice. The figure shows binding energy predictions in the case of the five-dimensional model $\boldsymbol{\theta} = \{a_\mathrm{v}, a_\mathrm{s}, a_\mathrm{c}, a_\mathrm{a}, a_\mathrm{p}\}$ (blue dashed line) and the four-dimensional model $\boldsymbol{\theta} = \{a_\mathrm{v}, a_\mathrm{s}, a_\mathrm{c}, a_\mathrm{a}\}$ (red line). In the case of the four-dimensional model, a_p is classed as inactive by setting its value in the model to zero. A regression was then performed using only the most stable nuclei from the AME2016 dataset (see Section 6.3.2 for a further discussion). Binding energy predictions were subsequently made using the regression results. The results confirm that the pairing term, governed by a_p, has little effect on the global behaviour of the model. In this case, there exist only minor local deviations in binding energy between the predictions including all parameters and the predictions excluding a_p. Therefore, a_p is implemented as an inactive parameter in the first four waves of the history match.

The differences in binding energies between the 4- and five-dimensional outputs are small but not negligible. Therefore, an additional uncertainty must be introduced into the implausibility measure of the history match (an additional variance in the denominator of Eq. (2.5)). The uncertainty variance is defined as $\sigma^2_{\mathrm{inactive}}$. Since the pairing term introduces a dependence on whether A is odd or even, it was possible to calculate the deviance of E_B between the two cases. This allowed for a calculation of $\sigma_{\mathrm{inactive}} \approx 0.02$ MeV/A. Since the liquid drop model is solvable analytically, it was also possible to calculate the uncertainty between the outputs of the four- and five-dimensional models directly. This gave a value of $\sigma_{\mathrm{inactive}} \approx 0.01$ MeV/A. Since

a_p is only inactive for the early waves of the history match, a larger σ_inactive should not affect the final result. The larger value of $\sigma_\mathrm{inactive} = 0.02$ MeV/A is therefore included within the implausibility measure. The resulting $\pm 3\sigma_\mathrm{inactive}$ range is also shown in Fig. 6.1, confirming that the binding energies of the five-dimensional model fall within $\pm 3\sigma_\mathrm{inactive}$ of the four-dimensional output.

6.3.2 Selection of Observables

Several considerations must be taken into account when selecting which observables to use. Including all nuclei in the AME2016 dataset would incur a notable computational cost, largely due to the fact that the emulator must be trained and run for each observable separately. Instead, the limitations of the liquid drop model are considered, i.e., the model is most successful when considering the *maximum* binding energy for a given value of A. These are the most stable nuclei, lying at the bottom of the 'valley' of stability [52]. Including only these nuclei within the history match reduces the dataset from 2469 observables to 258. Since nuclei with $A < 20$ are not accurately represented by the liquid drop model [53, 54], they are also excluded. Although the liquid drop model predictions of nuclei $20 \leq A < 40$ can also be less accurate, the inaccuracy can be accounted for by associating a high model discrepancy [55] with these nuclei. However, large vales of σ_model may lead to uncharacteristically large non-implausible volumes being found, motivating inclusion of heavier nuclei with lower σ_model.

However, heavier nuclei are not without disadvantages; Only a small change in the model parameters leads to a significant change in the binding energy in regards to these nuclei. This high sensitivity to input parameters is illustrated in Fig. 6.2, where the parameters of the model have been perturbed by a small noise $\epsilon \sim \mathcal{N}(0, \sigma^2)$, where $\sigma = 5 \times 10^{-4}$. The mean of the binding energies given by 1000 parameter perturbations was found to follow the experimental data well. The variance in binding energy increases with atomic number, indicating an increasing sensitivity to parameters with A.

Nuclei with a high sensitivity to parameter variation require relatively dense sampling in order to find non-implausible parameter samples. To avoid incurring long computational times due to using a high number of samples over a large initial parameter volume, only light nuclei are considered in the first wave and heavier nuclei are introduced in later waves. The goal is to sufficiently reduce the parameter volume in a wave such that denser sampling can occur in the subsequent wave. This in turn allows heavier (more parameter sensitive) nuclei to be included at each iteration. Fig. 6.3a shows the observables introduced in each wave of the history matching scheme. The nuclei included in the first wave are chosen such that the peak in binding energies as a function of mass number is captured. To further reduce the computational cost of including all observables, only every third observable given in the AME2016 dataset is used. Each observable is plotted with its respective uncertainty, where the uncertainties are discussed in more detail in Section 6.3.3.

During the first four waves of the history match, represented in Fig. 6.3a, a_p is inactive. a_p is introduced in the fifth wave. As mentioned, only nuclei that result in the maximum E_B/A for a given A were included in the first four waves. However, the maximum E_B/A usually occurs for even-even Z and N [50]. Since the pairing term is dependent on the odd or even nature of Z and N, further observables are required upon the inclusion of a_p. Fig. 6.3b illustrates one observable chosen in wave 4, with $A = 100$ and $Z = 44$, resulting in maximum E_B/A. In wave 5, observables leading to the second and third maximum E_B/A are included. Note that in Fig. 6.3b, these observables also have odd proton number, $Z = 43$ and $Z = 45$, allowing better evaluation of the pairing term.

In Table 6.1, the number of observables used in each wave is given. Also given are the intervals of A that these observables fall within. The justification for such intervals is discussed in Section 6.3.3.

Wave	1	2	3
Nucleon Number	$20 \leq A < 40$	$20 \leq A < 140$	$20 \leq A < 200$
Number of Observables	10	40	60
Wave	4	5	
Nucleon Number	$20 \leq A \leq 269$	$20 \leq A \leq 269$	
Number of Observables	83	182	

Table 6.1: The number of observables used within each wave the history match. Each set falls within the given intervals of nucleon number A.

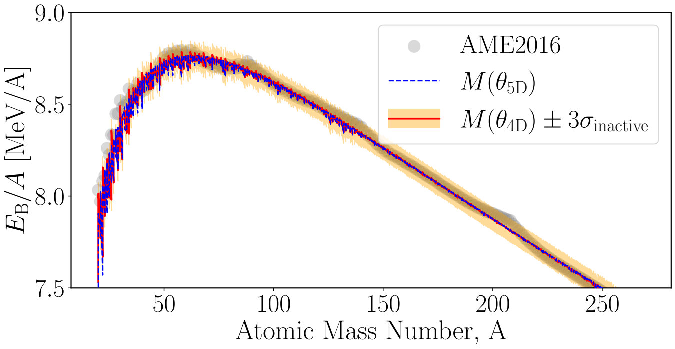

Figure 6.1: Diagnostic plot used to determine the viability of classing a_p as inactive. Model outputs were produced using parameters obtained through a linear regression trained on observables lying within the bottom of the valley of stability.

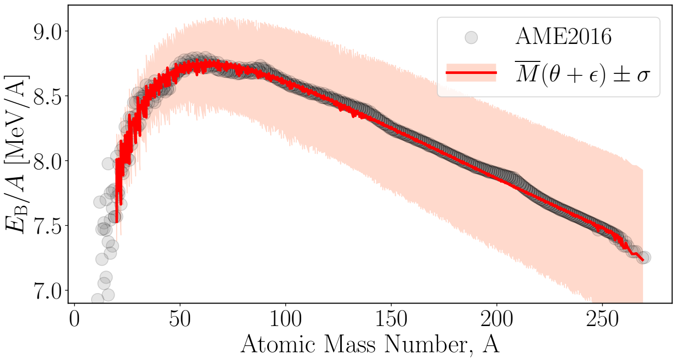

Figure 6.2: An average of 1000 outputs of the liquid drop model, given small random perturbations to the model parameters. The notation $\overline{M}(\theta+\epsilon)$ refers to the mean of the model outputs. $\pm\sigma$ is the standard deviation, where $\sigma^2 = \text{Var}[M(\theta+\epsilon)]$.

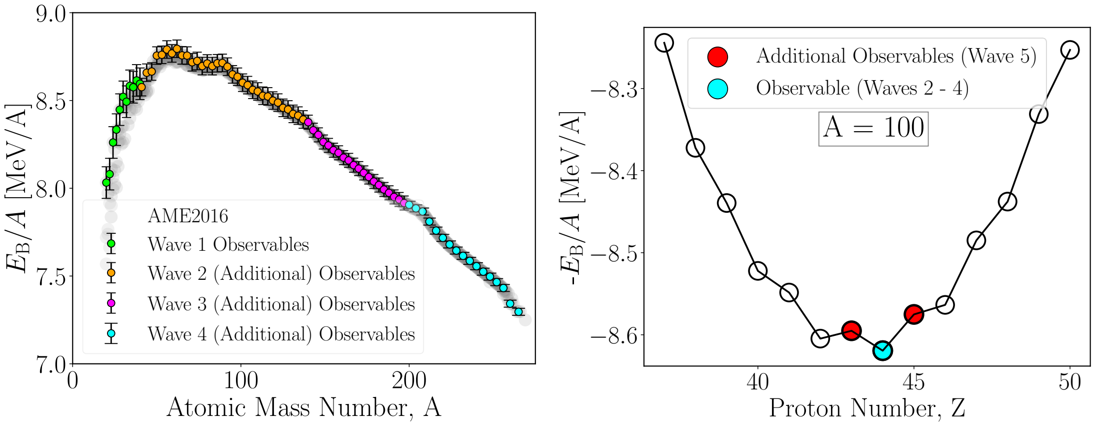

(a) **(b)**

Figure 6.3: Observables used in waves 1-4 of the history match are shown in (a). $1\sigma_{\text{model}}$ error bars are given in Table 6.2. Binding energy per nucleon for nuclei with $A = 100$ is shown in (b). The observable in waves 2-4 is in blue and additional nuclei included in wave 5 are in red.

6.3.3 Uncertainty Quantification

Observables z_i in the AME2016 dataset are given alongside experimental uncertainties corresponding to $\pm 1\sigma$, which may be used directly in the history matching scheme as $\sigma_{\mathrm{exp,i}}$. Values for $\sigma_{\mathrm{exp,i}}$ are very small, approximately six orders of magnitude smaller than the value of $E_{\mathrm{B},i}/A$.

Experimental uncertainties are typically simple to obtain, due to their inclusion with the data. In contrast, estimating the model discrepancy is more challenging. As discussed in Section 2.1.1, a commonly used method of determining uncertainties is through estimation from experts in the field. In the case of the liquid drop model, the model discrepancy is estimated by expert opinion to be $\sigma_{\mathrm{model}} \sim 0.1$ MeV/A [56].

Wrongly estimating the model discrepancy — even possible when relying on expert opinion — can lead to bias and an unrealistic confidence in parameter estimates. Since the purpose of the toy model is to serve as purely method validation, we have a rare case of being able to infer parameters analytically and directly determine the model discrepancy using the model outputs. Although not a viable solution when handling more complex models, it serves the purpose of confirming or disproving the expert estimation of the uncertainty.

To obtain an estimation of the uncertainty variance $\sigma^2_{\mathrm{model}}$, the model discrepancy is modelled as a normal distributed variable with mean zero and variance $\sigma^2_{\mathrm{model}}$. $\sigma^2_{\mathrm{model}}$ can be obtained using the sample variance S^2, defined as [57]

$$\sigma^2_{\mathrm{model}} = S^2 = \sum_{i=1}^{n} \frac{(E_{\mathrm{B},i}/A - \hat{E}_{\mathrm{B},i}/A)^2}{(n-p-1)}. \tag{6.16}$$

In the above expression, the residual sum of squares between an experimental binding energy per nucleon $E_{\mathrm{B},i}/A$ and a regression prediction $\hat{E}_{\mathrm{B},i}/A$ is divided by the degrees of freedom, $(n-p-1)$ (where p is the number of model parameters). A value of $S = 0.018$ MeV/A was obtained.

The calculation of the sample variance operates under the assumption of homoscedastic errors. In reality, the accuracy of the liquid drop model varies with A and thus the uncertainties are heterogeneous. In particular, the liquid drop model is unsuccessful at representing light nuclei [53, 54] which affects any uncertainty quantification performed over the range of nuclei used. Furthermore, the discrepancy was estimated using only the observables lying at the bottom of the valley of stability. Including all observables in the AME2016 dataset would have resulted in a significantly higher model discrepancy variance. Consequently, a value of $\sigma_{\mathrm{model}} \approx 0.02$ MeV/A intuitively seems low when considering both this fact and the expert-obtained value.

In order to further determine a reasonable value, a literature review was undertaken. A study [58] taking a similar approach finds a model discrepancy variance of $\sigma = 3.698$ MeV when investigating the *total* binding energy E_{B} over a dataset covering the range of all nuclei. In comparison, our of $\sigma_{\mathrm{model}} \approx 0.02$ MeV/A considers the binding energy *per nucleon* E_{B}/A. For heavy nuclei with $A \geq 200$, the results are comparable. However, using $\sigma_{\text{model}} = 0.02$ MeV/A within the history match when modelling lighter nuclei may lead to unrealistically designating non-implausible samples as implausible.

A study [55] to estimate the coefficients of the liquid drop model, also using the AME2016 dataset, takes the approach of categorising nuclei based on number of nucleons. Percentage errors on the binding energies are computed over several intervals of A. For $A \geq 200, \left|\delta E_{\text{B}}\right| / E_{\text{B}}$ is given as 0.2%, which is again comparable to the sample variance obtained through linear regression. In contrast, a percentage error of 11% is given for $20 \leq A < 40$.

Care must be taken to not assume that these are 'true' model discrepancies. However, when combined with expert opinion, they do provide an insight into how much the model discrepancy varies with A. The final model discrepancies used within the history match are influenced by both expert opinion and the residual method. To partially account for heteroscedasticity, they are grouped using the same intervals of A used in Ref. [55]. Then, assuming homoscedasticity within each interval, the uncertainties are scaled with increasing A. The final model discrepancies used within the history match of the liquid drop model are given in Table 6.2.

	$20 \leq A < 40$	$40 \leq A < 140$	$140 \leq A < 200$	$A \geq 200$
σ_{model} (MeV/A)	0.09	0.05	0.04	0.02

Table 6.2: The standard deviation of the model discrepancy σ_{model} used within the history match, given for various intervals of nucleon number A.

Since the aim of applying history matching to the liquid drop model is only to validate the method for use in later models, further methods of approximating the model discrepancy (see Section 2.1.1) are considered outside the scope of this particular application.

The model discrepancy values decided upon are, of course, an approximation. Approximations, and underestimations in particular, lead to samples within the history matching scheme being incorrectly labelled as implausible. We now refer back to the implausibility measure in Eq. (2.5), where the (first) maximum implausibility is taken. As a method of safeguarding against such an event, the second maximum implausibility value is taken instead of the maximum within the history matching of the liquid drop model.

6.3.4 Analytical Solution

Using the set of AME2016 observables included in wave 5 of the history match, and the corresponding uncertainties specified in the previous section, a linear regression is performed on the liquid drop model. A multivariate, joint posterior PDF is obtained following the procedure given in Section 6.1. The uni- and bi-variate marginalised PDFs between parameters are shown in Fig. 6.4.

The mode of the one-dimensional marginalised posterior distributions in Fig. 6.4 provide an optimal set of parameters that may be used to validate the history-matching results. If the history match is successful, then this set of parameters will fall within the non-implausible volume.

The two-dimensional marginalised posterior distributions provide an insight into the shape of the non-implausible volume expected from the history match. The aim of history matching is to find *all* sets of parameters that provide outputs consistent with the data, given the uncertainties. OLS, on the other hand, finds the *optimal* set of parameters. As a result, history matching will not provide non-implausible regions of equal size to the analytical posterior distribution. However, the aim of the history match is to validate that the analytical posteriors lie within the non-implausible volume. In addition, the posterior distributions do convey the strength of the correlations between parameters. It is these correlations that we aim to reproduce with the history match when implementing the rotated hyperrectangle, Gaussian, and ellipsoid definitions of a non-implausible volume.

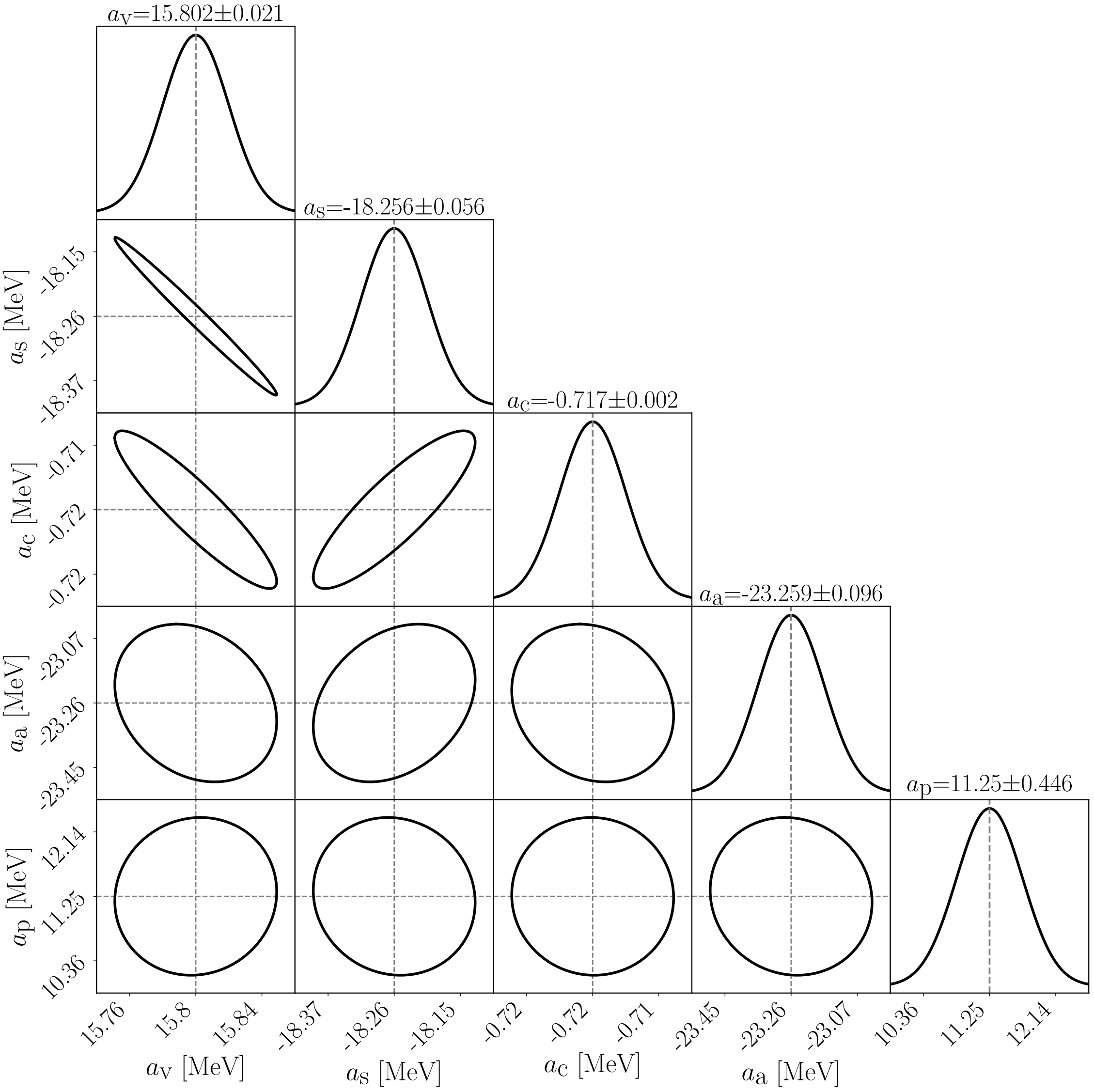

Figure 6.4: Marginalised posterior PDFs for each parameter of the liquid drop model, obtained through OLS regression.

Part III

Results and Discussion

Chapter 7

Toy Model Validation

The liquid drop model was introduced as a toy model in Chapter 6. In this chapter, the toy model is used to validate the history matching approach with a focus on comparing the non-implausible volume definitions described in Chapter 5. In particular, we perform a quantification of the size of the non-implausible parameter volumes obtained with each volume-definition. Additionally, we analyse the sample resolution and optical depth obtained using each volume-definition. These terms will be further defined in the upcoming chapter.

The history match was run for five waves with the aim of obtaining a five-dimensional non-implausible parameter volume for the liquid drop model. The initial parameter space searched is defined by minimum and maximum parameter values in each dimension, given in Table 7.1. The choice of such values was guided by *a priori* information about the liquid drop model coefficients. By definition, the volume term should be positive. The surface, Coulomb and asymmetry terms act as corrections to the volume term, implying that the corresponding coefficients should be negative. The pairing term is defined such that it changes sign based on whether A, Z, or N are odd or even. By convention, the coefficient is positive.

Since the inference of liquid drop model coefficients is a popular subject, the order of magnitude of the parameters is easily obtained. Refs. [55, 58] may be referred to for examples of inferred parameter values. Additionally, a regression performed on the liquid drop model provides a set of optimal parameters bma^*. As such, the initial area of parameter space to search was constructed so that the optimum parameter values lay near the centre of the range to search. The volumes were chosen to be large enough that the capabilities of the history matching scheme could be probed, given that the final volume should be significantly smaller than the initial volume. The initial parameter space adheres to the *a priori* knowledge of whether a parameter was positive or negative.

Due to the possession of only minimum and maximum parameter bounds at the initialisation of the first wave, hyperrectangle sampling must be used. In subsequent waves, the procedure diverges according to the chosen non-implausible volume type. The history match was therefore run using hyperrectangle, rotated hyperrectangle, Gaussian, and ellipsoidal non-implausible volumes after the first wave, yielding four sets of results. The hyperrectangle design is least efficient, requiring $N = 1 \times 10^7$ samples in each wave (see Section 7.3), whereas $N = 1 \times 10^6$ samples were used for all other volume types.

Fig. 7.1 shows hyperrectangle non-implausible volumes obtained at the end of each wave. Each volume is constructed from the non-implausible samples remaining at the end of the respective wave and, for waves 1-4, used for sample generation in the following wave. Also shown are the non-implausible samples remaining at the end of wave 5. Only the final non-implausible volume is shown in the case of a_p since this parameter was inactive until the last wave.

Upon comparison of Fig. 6.4 and Fig. 7.1, one can confirm that the hyperrectangle non-implausible volume successfully encloses the set of optimal parameters obtained through OLS. Furthermore, the final set of non-implausible parameter samples correspond with the correlation behaviour seen in Fig. 6.4. However, the hyperrectangle volumes constructed around the sets of non-implausible samples observed in each wave does not capture this correlation information. In comparison, correlation information is retained within the non-implausible volumes obtained using an ellipsoidal definition of the non-implausible volume, shown in Fig. 7.2. Similar plots obtained for the rotated hyperrectangle and the Gaussian may be found in Appendix A.

	a_v	a_s	a_c	a_a	a_p
$a_{i,\mathrm{min}}$ (MeV)	0	-50	-3	-50	0
$a_{i,\mathrm{max}}$ (MeV)	40	0	3	0	40
a^* (MeV)	15.8	-18.3	0.72	-23.3	11.25

Table 7.1: The minimum and maximum bounds of the initial parameter space for each coefficient of the liquid drop model.

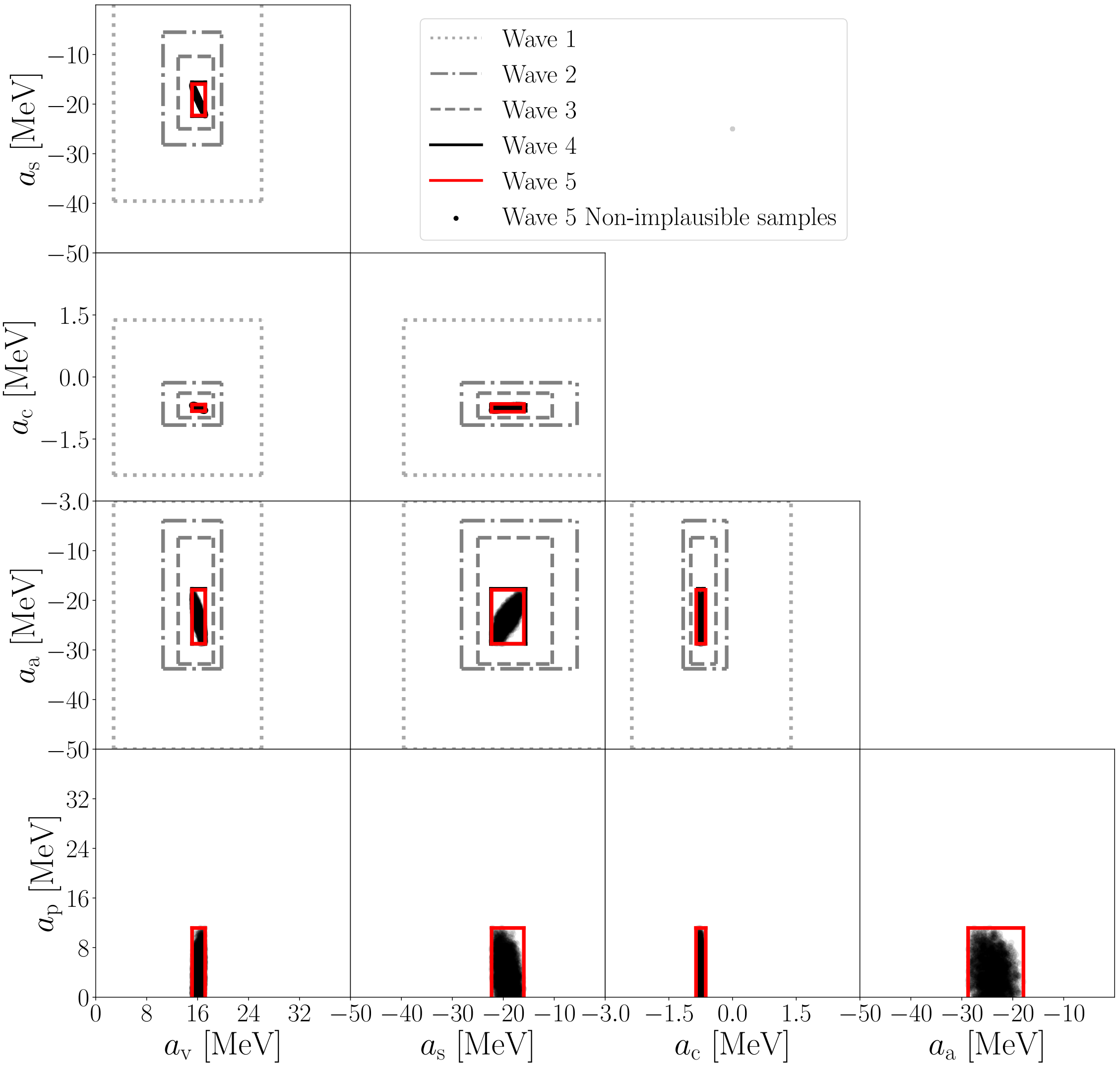

Figure 7.1: Two-dimensional representations of the non-implausible volumes obtained after each wave of the history match, using a hyperrectangle-defined non-implausible volume. Also shown are the non-implausible samples remaining after wave 5. The limits of the axes correspond to the initial parameter space searched.

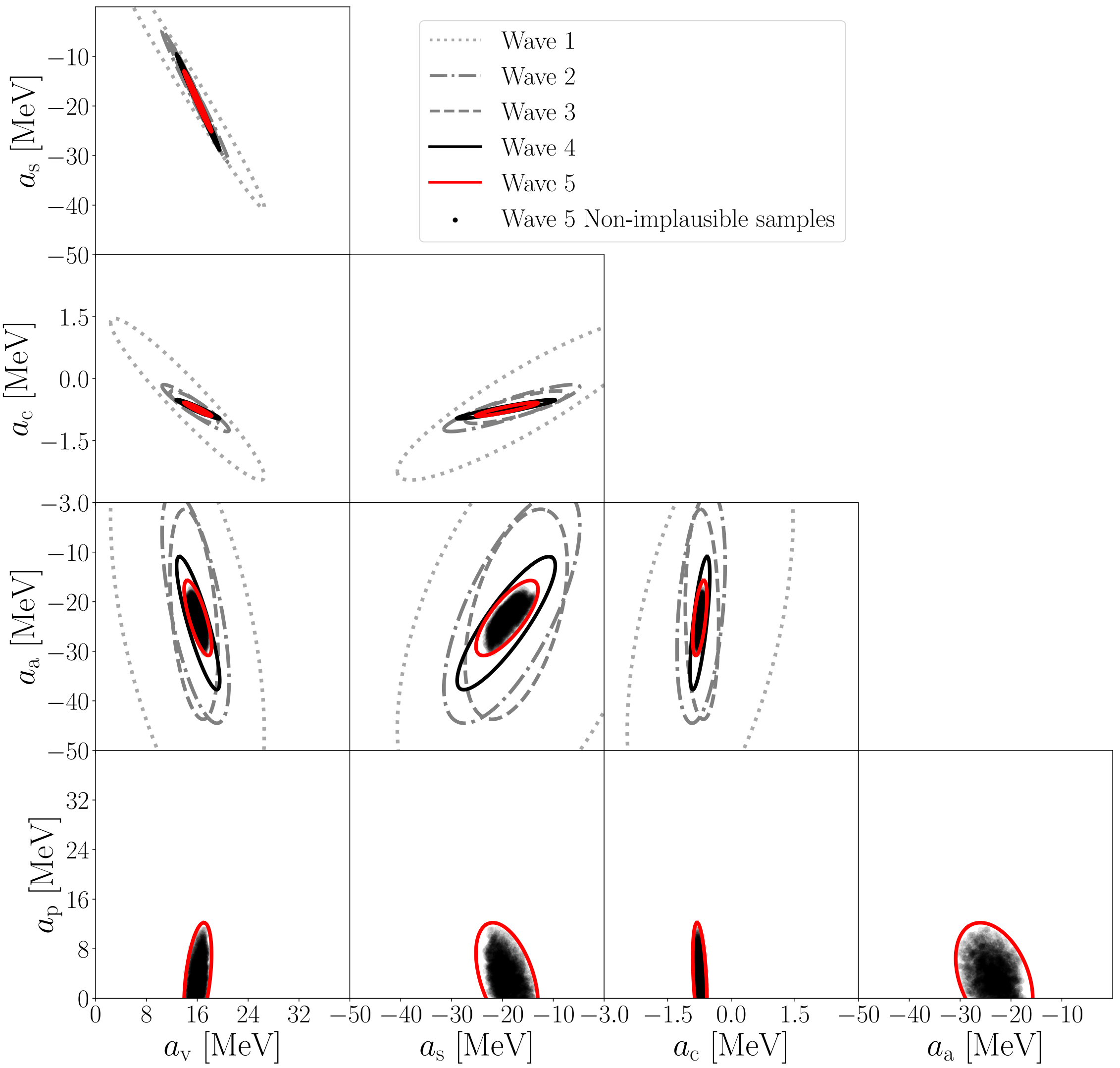

Figure 7.2: Non-implausible volumes at each of five waves of history matching, implementing an ellipsoidal volume. Also plotted are the non-implausible samples remaining in the final (fifth) wave. The limits of the axes correspond to the initial parameter space searched.

7.1 Non-implausible Volume Comparison

It is desirable to efficiently reduce the parameter volume during the history match. As such, we aim to quantify the volume reduction achieved using each of the non-implausible volume-definitions and compare the results in order to determine the most effective choice.

We begin by reminding the reader of the two related, but distinct, ways of defining a non-implausible volume introduced in Chapter 5. At the end of each wave, a set of non-implausible samples is obtained. Using the first definition of a non-implausible volume, one may construct a bounding volume enclosing this set of non-implausible samples. Upon possession of a bounding volume, one can quantify the volume of parameter space enclosed within it. Table 7.2 shows each wave with a volume value given for each of the volume-definitions used, obtained using the set of non-implausible samples obtained at the end of the respective wave. Since the set of samples used in the following wave is generated according to the volume-definition employed (see the second way of defining a non-implausible volume), the values in the table provide insight into how strongly the sampling designs affect the reduction of parameter space.

Calculations of hyperrectangle and rotated hyperrectangle volumes are trivial. To find the volume of a Gaussian or an ellipsoid, one must obtain the eigendecomposition of the covariance matrix of the non-implausible samples (Eq. (5.1)). Since $\mathbf{\Lambda}$, the diagonal matrix of eigenvalues λ_i, represents the magnitude of the variance in the directions of the eigenvectors, the size of the half axes of the ellipsoid can be calculated as

$$a_i = \chi_{d,\alpha}\sqrt{\lambda_i}, \tag{7.1}$$

where $\chi^2_{d,\alpha}$ is the critical value of the chi-squared distribution. The volume of an n-dimensional ellipsoid described by Eq. (5.6) is then given by [59]

$$V = \frac{2}{n}\frac{\pi^{n/2}}{\Gamma(n/2)}\prod_{i=1}^{n} a_i. \tag{7.2}$$

In the case of the Gaussian volumes in Table 7.2, a value of $\alpha = 0.05$ was chosen such that the volume within a 95% iso-probability contour is calculated. In the case of the ellipsoid, the ellipsoid sampling design used the same value of $\alpha = 0.05$ and therefore the same value of $\chi_{d,\alpha}$ in order to aid comparison between the two bounding volumes.

The volumes of the final non-implausible regions are given as a percentage of the initial parameter space sampled in the first wave. In all cases, the final volume is notably small and demonstrates a successful location of a small non-implausible volume relative to the initial parameter space. Volume-definitions that allow for correlations to be captured lead to smaller values than those of the hyperrectangle. This is not an unexpected result; Fig. 6.4 indicates that strong correlations between parameters do exist and thus constructing a hyperrectangle around naturally correlated samples will result in an unnecessarily large volume.

Interestingly, the ellipsoid-defined volumes are slightly larger than those obtained with the Gaussian-definition. Since the Gaussian design leads to a low density of samples far from the mean, non-implausible samples are less likely to be found in this region of parameter space. This is not a reflection of reality but mainly an artifact of using Gaussian distributed samples. In the case of the ellipsoid-defined volume, the uniformity of samples could be preventing a similar outcome. More non-implausible samples may therefore be found at the edges of the ellipsoid that the Gaussian-method failed to locate, leading to an increase in the size of the bounding volume.

However, when constructing the ellipsoid volumes, a cut-off is imposed on the initially normally distributed samples by choosing $\chi^2_{d,0.05}$. This implies that there is always a small subset of parameter samples that may be non-implausible but are discarded nonetheless. When defining a Gaussian-defined volume, no such cut-off is imposed and thus no information is lost.[1] Therefore, the ellipsoid potentially 'loses' a small region of non-implausible parameter space. However, in the case of the ellipsoid, this may be remedied by increasing the choice of $\chi^2_{d,\alpha}$, although this was not deemed necessary in the case of a toy model validation. There is no such approach available to counter the bias of the Gaussian described earlier.

			Volume (%)	
Wave	Dim.	No. Obs.	Hyperrectangle	Rot. Hyperrectangle
1	4	10	16	0.62
2	4	40	1.1	0.12
3	4	60	0.23	0.06
4	4	83	0.05	8.4×10^{-3}
5	5	182	1.4×10^{-3}	8.7×10^{-5}
			Volume (%)	
Wave	Dim.	No. Obs.	Gaussian (95% C.I.)	Ellipsoid
1	4	10	0.19	0.19
2	4	40	2.2×10^{-3}	3.5×10^{-3}
3	4	60	6.2×10^{-4}	1.8×10^{-3}
4	4	83	6.6×10^{-5}	2.4×10^{-4}
5	5	182	4.1×10^{-6}	1.93×10^{-5}

Table 7.2: Parameter volume remaining at the end of each wave of the history match of the liquid drop model. The volume is given as a percentage of the initial parameter volume. For a Gaussian, the volume is calculated for a 95% probability mass and compared against 95% of the initial parameter volume. The total number of observables included in a given wave is included in the second column. Also given is the parameter dimensionality of the history match. Where only 4 parameters are included in the history match, the fifth-dimension uses a prior over a_{p} when calculating volume. This prior range is unchanged by the history match until wave 5.

---

[1] In the case of a Gaussian, the choice of $\chi^2_{d,0.05}$ is only relevant if one wishes to visualise results in the form of an iso-probability surface.

The history match was terminated after five waves. Significant reduction of the non-implausible parameter volume was unlikely to occur after five waves due to the high precision emulators that had been constructed, leading to $\sigma_{\text{em}} < \sigma_{\text{model}}$. Although notable volume reductions were achieved relative to the initial parameter volume searched, the final non-implausible volumes are not particularly small in size. This may be explained by performing a principle component analysis.

A principle component analysis aims to decompose the parameter space into *uncorrelated* components. This is done to understand how different directions of parameter space contribute to variability in model output. To perform the analysis we follow the procedure in Ref. [58], and a conditioned Hessian is constructed as

$$\tilde{H}_{ij} = \frac{\Sigma^{-1}_{ij}}{\sqrt{\Sigma^{-1}_{ii}}\sqrt{\Sigma^{-1}_{jj}}}, \tag{7.3}$$

where Σ is the covariance matrix of the final set of non-implausible samples obtained with the history match (using a ellipsoidal sampling design). Performing an eigen-decomposition on $\tilde{H}_{ij}$ provides a set of eigenvalues $\tilde{h}_i$, $i = 1, ..., d$, where $d = 5$ is the dimensionality of the liquid drop model. These eigenvalues are a quantification of how much each of the d components contribute to the model output variation. Therefore, a large value of $\tilde{h}_i$ indicates that this component has a significant effect on the cost function χ^2 (Eq. (6.8)). One requires that, for the model output variability to be captured, that the following cumulative value reaches a threshold. This may be written as

$$S_n = \frac{\sum_{i=1}^{n} \tilde{h}_i}{d}. \tag{7.4}$$

The threshold is typically set to $S_{\text{lim}} = 0.99$ [58]. Fig. 7.3 shows the cumulative value with components ordered from highest $\tilde{h}_i$ to lowest. After the inclusion of only three components, $S_3 > S_{\text{lim}}$. This implies that 99% of the variation in the output of the model may be captured by only three linear combinations of the the components, i.e., all data can be reproduced by varying the parameter space in only three directions. This explains the strong correlation structure of the model parameters.

The implication of such a result is that there essentially exist two redundant directions in parameter space that contribute very little to changes in model output. If the model output falls close to the observational data at one point, then regardless of how much parameters are varied along the redundant directions, the output will *always* fall close to the data. We refer back to the implausibility measure in Eq. (2.5) and note that this would lead to consistently low implausibility values for many parameter values. Therefore, we cannot expect the final non-implausible volume to be tightly constrained.

7.2 Non-implausible Sample Comparison

Table 7.3 shows the number of samples remaining, a.k.a deemed non-implausible, at the end of each wave. The number of samples remaining is given as a percentage of the total number of samples generated at the start of each wave.

There is no trend immediately visible in Table 7.3 due to the introduction of additional observables in each wave. Some of the chosen observables appear to have a greater effect on model output than others (see Fig. 6.2), and so the number of remaining samples fluctuates between waves. However, the results confirm that a number of samples are removed in each wave, and therefore all waves are necessary within the history match.

More interesting is the comparison between different non-implausible volume types. Significantly more samples are discarded when defining the volume as a hyperrectangle than in comparison to other volume definitions. This can qualitatively be explained by the 'empty space' seen within the non-implausible hyperrectangle volumes in Fig. 7.1. Each wave requires the resampling of this 'empty space', despite it containing samples already deemed implausible. Needlessly resampling an implausible parameter space is both computationally inefficient and reduces the precision of the emulator that may be obtained if sampling a smaller area.

		Samples Remaining (%)			
Wave	No. Obs.	Hyperrectangle	Rot. Hyperrectangle	Gaussian	Ellipsoid
1	10	0.09	0.09	0.09	0.09
2	40	2.0×10^{-3}	0.19	2.69	0.60
3	60	9.0×10^{-4}	4.70	44.3	15.5
4	83	1.0×10^{-4}	1.22	18.7	3.97
5	182	0.06	0.47	6.97	1.51

Table 7.3: Fraction of samples labelled as non-implausible after each wave of the history match of the liquid drop model. The fractions are given as a percentage of the initial number of samples at the start of each wave. In the case of the hyperrectangle non-implausible volume, the initial number of samples used was $N = 1 \times 10^7$. For all other volume types, the initial number of samples used was $N = 1 \times 10^6$. The total number of observables included in a given wave is included in the second column. Since the first wave of the history match requires samples to be generated over a hyperrectangle of parameter space, the fraction of samples is the same in wave 1 for all volume-definitions.

Fig. 7.4 illustrates the density of samples obtained in wave 2 through the *optical depth*. In each dimension, the optical depth represents the fraction (or 'depth') of the hidden non-implausible volume at a specified parameter coordinate. To compute the optical depth, an input parameter i is selected and the ith parameter range is divided into a number of bins. Each non-implausible sample, obtained at the end of a wave, is then assigned to a bin according to its i^{th} element. The same is done for the total set of samples used in the respective wave. One may then find the ratio of non-implausible samples to total samples in each bin. This is the optical depth, conditioned on the input i. One may perform a similar analysis in two-dimensions, conditioned on parameters (i, j).

Also indicated in Fig. 7.4 are analytical parameter values obtained through OLS. Note that the analytical parameter values displayed here are obtained from a regression using *only* the observables included in wave 2 of the history match. They are therefore different to those in Fig. 6.4, but more representative of those we may expect to see in this particular wave. The optical depth peaks close to the analytical value in all parameter dimensions.

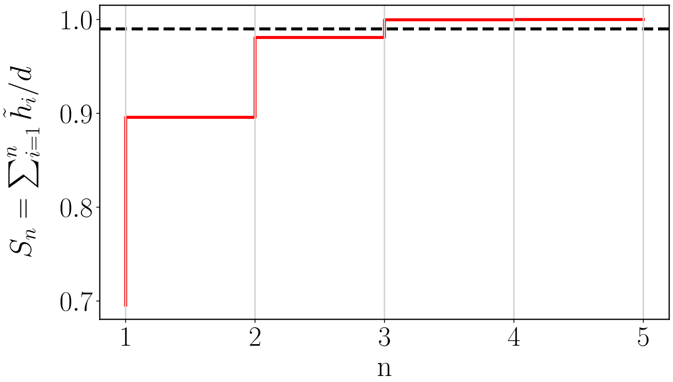

Figure 7.3: The cumulative value of the eigenvalues of the conditioned Hessian. 99% of the variability of the model output is captured by n model components once $S_n > 0.99$. Here we find that n=3 fulfills this criteria.

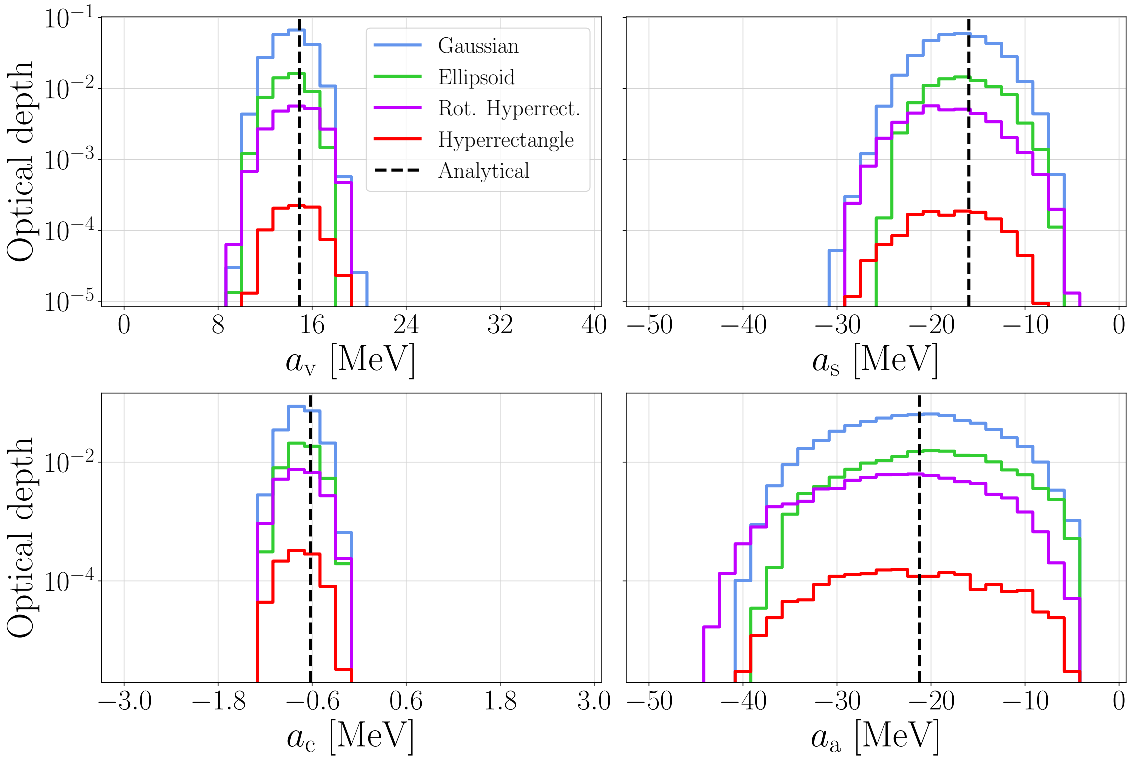

Figure 7.4: Optical depth given for each volume type in wave 2. The optical depth indicates the fraction of the hidden parameter volume deemed non-implausible, and is given on a log scale.

7.3 Sample Resolution

A notable result arising from the study of the different volume types is that of the sample resolution required for a successful run. It is desirable to analyse the sample resolution since the aim of history matching is to be able to resolve an interesting parameter region that may be significantly smaller than the initial parameter space searched. As introduced in Chapter 5, generating samples across a high-dimensional space may lead to a sparsity of samples. This may be combated through the use of a space-filling design. However, there will still be some distance between samples regardless of the dimensionality of choice of sampling design. Therefore, there is a risk of failing to locate a non-implausible volume if its size is smaller than the distance between samples. To ensure that a non-implausible volume is located, if it exists, then a high enough sample resolution is required. Rather than achieving high resolution through an increase in total number of samples, we speculated that the various sampling designs introduced in this thesis differ in their sampling resolution. We therefore conducted an investigation into the sample resolutions.

Each run of history matching begins with same first wave — samples are generated across the parameter volume using a hyperrectangle design. The result is the same set of non-implausible samples obtained at the end of wave 1, regardless of the choice of non-implausible volume. The samples at the start of wave 2 are generated using these identical sets of non-implausible samples but now differ according to the sampling design used. This allows for a direct comparison between samples generated at the beginning of wave 2.

To perform the analysis, a number of samples were generated for each volume type, using the *same* initial set of non-implausible samples. The nearest neighbour to each sample was located. The distance between a sample and its nearest neighbour was then computed, in the form of a four-dimensional vector. Fig. 7.5 shows the *average* distance to nearest neighbour in each dimension and for a given total number of samples.

Also computed is the analytical length scale, which we define for the purposes of this analysis as the $\pm 3\sigma$ range for each parameter, obtained through a regression, similar to that performed in Section 6.3.4, except using only observables included within wave 2 of the history match. The analytical length scale provides an approximation to the minimum scale of the non-implausible region that may be obtained in each dimension. The results of this analysis are presented in Fig. 7.5.

The hyperrectangle-defined volume leads to far sparser sampling than the alternate volume definitions. In the cases of a_{v} and a_{c} in Fig. 7.5, the average distance between samples remains higher than the analytical length scale for total number of samples $N < 10^7$. This justifies the choice of using $N = 10^7$ samples when implementing a hyperrectangle volume in the history match presented in this chapter. It also implies that, in general, using a hyperrectangle volume may lead to a failure in locating a particularly small non-implausible volume.

Fig. 7.6 shows the number of samples deemed non-implausible after evaluating the implausibility of the samples generated for Fig. 7.5. As expected, the hyperrectangle-defined volume locates fewer non-implausible samples than the alternative sample designs due to the low density of samples around the non-implausible volume.

The remaining volume-types perform notably better in regards to both number of non-implausible samples obtained, seen in Fig. 7.6, and the sample resolution, seen in Fig. 7.5. The Gaussian, both according to the 68% and 95% iso-probability contours, achieves the highest sample resolution and requires the least total number of samples. However, this success is dependent on the non-implausible volume lying close to the mean of the Gaussian, or at least within the probability contours defined in the figure.

The ellipsoid achieves a sample resolution that is comparable to the Gaussian, although slightly lower. It can therefore be said that the use of an ellipsoidal design can help to prevent a failure to locate a small non-implausible region without an increase in the total number of samples. Combined with its similar success in volume reduction seen in 7.1, its ability to capture correlations, and the removal of the bias present in the Gaussian, we can conclude that an ellipsoid design appears to be the most successful of the design types.

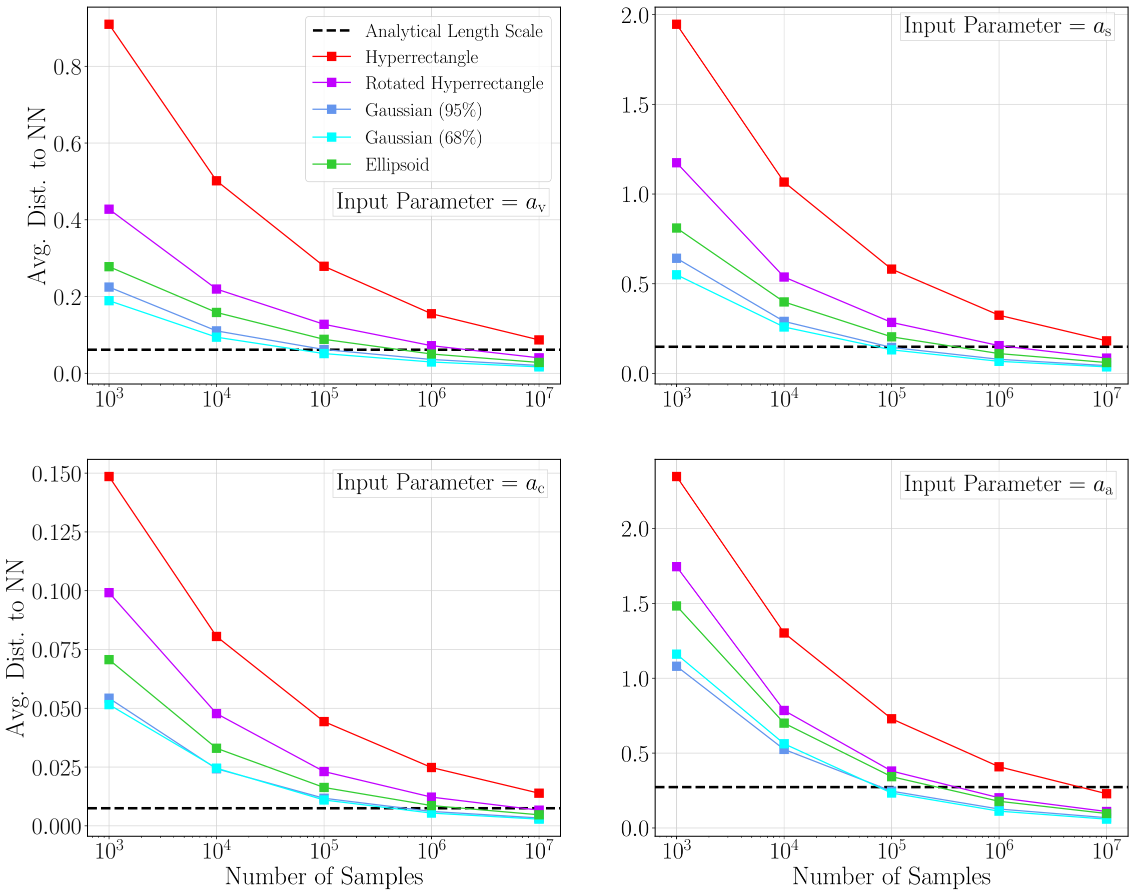

Figure 7.5: The average distance to nearest neighbour (denoted as NN), in each parameter dimension, as a function of the total number of samples in a given volume. Also shown in the analytical length scale, defined as the $\pm 3\sigma$ range, in each dimension, of the analytically obtained posterior distribution.

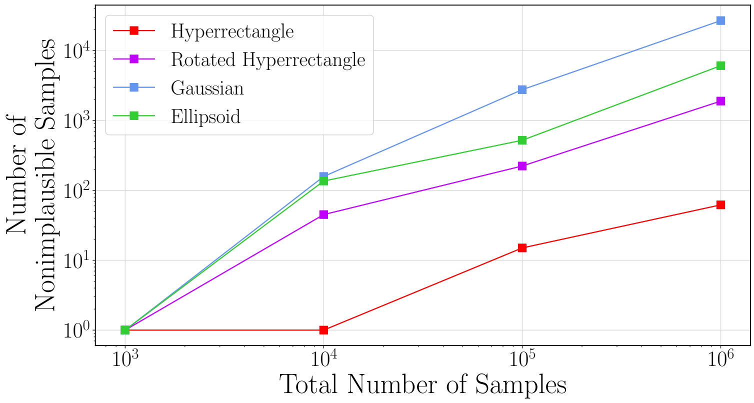

Figure 7.6: The number of samples deemed non-implausible in the second wave of the history match, given the total number of samples generated, for each volume definition. Note that the hyperrectangle locates only a single non-implausible sample for low values of the total number of samples.

Chapter 8

History Match of χEFT in the Nucleon-Nucleon Sector

As detailed in Chapter 3, working within the χEFT framework provides a model allowing for the calculation of NN scattering observables. However, working with χEFT introduces a set of unknown low-energy constants (LECs). In this chapter, we aim to apply history matching to the χEFT model at LO in MWPC in the NN sector. The aim is to obtain non-implausible parameter volumes containing LECs that produce model outputs consistent with *np* scattering observables. Implementing MWPC at LO introduces four LECs. The parameter vector is given by

$$\boldsymbol{\theta} = (\widetilde{C}_{^1S_0}, \widetilde{C}_{^3S_1}, C_{^3P_0}, C_{^3P_2}). \tag{8.1}$$

The corresponding units for each LEC are

$$(10^4 \text{ GeV}^{-2}, 10^4 \text{ GeV}^{-2}, 10^4 \text{ GeV}^{-4}, 10^4 \text{ GeV}^{-4}). \tag{8.2}$$

8.1 Computation of Scattering Phase Shifts and Observables

In order to implement a history match of χEFT, a set of model outputs must be generated for each sample in parameter space. The code used to compute model outputs for numerical solutions of the Lippmann-Schwinger equation, see Section 4.4.1, was kindly provided by O. Thim [60]. Constants used within the calculations are given in Table 8.1.

Constant	Value
Axial coupling g_A	1.29
Pion-decay constant f_π (MeV)	92.1
Nucleon mass m_N (MeV)	939.57
Pion mass m_π (MeV)	138.04

Table 8.1: Constants used within the computation of phase shifts and observables. These constants are present within the interaction potential at LO in MWPC. Note that mass and momenta units are typically MeV/c^2 and MeV/c, respectively, but this study implements $c = 1$.

Numerically solving the Lippmann-Schwinger equation requires a choice of the number of momentum-grid points N_p to be made — see Eq. (4.46). This choice must be carefully considered as high values of N_p result in computationally expensive calculations. However, overly low values may lead to non-converged results. To determine an optimal value, calculations of three SGT observables were performed across energies $12.995 \leq T_{\text{Lab}} \leq 40$ MeV. Table 8.3 can be referred to for the details of these observables. The calculations were made across a range of N_p values, with a momentum regulator cutoff $\Lambda = 450$ MeV. The LECs used for the calculations were chosen as the modes of the posteriors computed in Ref. [61], given by

$$\widetilde{C}_{^1S_0} = -0.112, \quad \widetilde{C}_{^3S_1} = -0.085, \quad C_{^3P_0} = 1.632, \quad C_{^3P_2} = 0.110. \tag{8.3}$$

The results of the evaluation are shown in Fig. 8.1. Plotted is the relative error of the output with respect to the total cross section computed at $N_p = 100$. This metric was chosen as convergence is expected at $N_p = 100$, and thus values close to 0 indicate that convergence has been achieved.

An acceptable level of convergence appears to be reached at around $N_p = 50$, where the relative error is $\sim 10^{-6}$. This is $\sim 10^4$ times greater than experimental uncertainties and $\sim 10^5$ times greater than model discrepancy (see Table 8.3). This is deemed as acceptable convergence, since any method uncertainty arising from the choice of N_p is insignificant in comparison to other uncertainties. A value of $N_p = 50$ was chosen for all further model runs in this thesis.

Also shown in Fig. 8.1b is the wall time taken to perform a calculation at each value of N_p. A quadratic fit was performed and calculation time is shown to have a quadratic dependence on N_p, justifying a conservative choice of N_p.

8.2 History Match Setup

In addition to model outputs, quantification of all relevant uncertainties is required in order to evaluate the implausibility measure. Experimental uncertainties are published in the literature. Method uncertainty is taken to be negligible. Model discrepancy is computed using the method outlined in Section 3.2, where values for $\bar{c}$ are required. Such values for $\bar{c}$, inferred across values of T_{Lab}, were provided by O. Thim [13]. The resulting values for σ_{model} may be found in Table 8.3. Note that the model discrepancy is, by far, the greatest contributor to the total error.

The history match itself is organised into two waves. The first wave introduces observational data in the form of *np* scattering phase shifts. In the second wave a different dataset is used, consisting of *np* scattering observables. A smaller number of total samples than used in the toy model validation (Chapter 7) were thought necessary, due to the lower dimensionality of parameter space. Therefore, a total of $N = 10^4$ samples are used in wave 1, and $N = 10^5$ samples are used in wave 2. Since correlations between LECs are not expected in wave 1, a hyperrectangle non-implausible volume is used.

Due to the introduction of a regulator function (see Section 4.4.1), LECs must be refitted to reproduce the observational data if different values of the momentum cutoff Λ are used. At higher values of $\Lambda \sim 700$ MeV, some LECs are seen to diverge. This behaviour is known as a limit cycle [8, 62]. Refs. [61, 63] use a cutoff $\Lambda = 450$ MeV at which there is no divergent behaviour. Therefore, the history match was initially run with the same Λ in order to be able to validate the obtained non-implausible volume with literature results. Upon validation using $\Lambda = 450$ MeV, the history match was run for further cutoffs $400 \leq \Lambda \leq 4000$ MeV. This is performed with the aim of investigating the behaviour of the χEFT model given variation in Λ.

In order to perform a history match, one must define an initial parameter space to be searched. To avoid the need for searching an infinitely large parameter space, or mistakenly searching the wrong area, the volume to search is therefore constructed so to contain LEC posterior modes computed in Ref. [61]. Ref. [61] also contains the standard deviations of the posteriors. Since history matching aims to find *all* non-implausible parameter space, the initial domains for $\widetilde{C}_{^1S_0}$, $\widetilde{C}_{^3S_1}$, and $\widetilde{C}_{^3P_0}$ were expanded to be an order of magnitude greater than the standard deviation of the corresponding posteriors in Ref. [61]. In the case of $\widetilde{C}_{^3P_2}$, the initial domain is two orders of magnitude greater, such that both the P-wave initial domains are comparable in size.

Since Ref. [61] implements $\Lambda = 450$ MeV, the initial parameter domains are thought to suffice for $\Lambda \leq 600$. The initial parameter volume is increased for greater values of Λ to account for LECs 'moving' through parameter space with increasing Λ. The initial parameter ranges to search are shown in Table 8.2.

	Λ	$\widetilde{C}_{^1S_0}$	$\widetilde{C}_{^3S_1}$	$C_{^3P_0}$	$C_{^3P_2}$
$\theta_{i,\text{min}}$	≤ 600	-0.16	-0.2	-10.0	-10.0
$\theta_{i,\text{max}}$	≤ 600	0.0	0.1	20.0	10.0
$\theta_{i,\text{min}}$	> 600	-0.3	-1.0	-10.0	-10.0
$\theta_{i,\text{max}}$	> 600	0	1.0	20.0	10.0

Table 8.2: The minimum and maximum bounds of the initial parameter space for each LEC. The use of the notation θ_i to denote a parameter follows that used in Section 2. For cutoffs $\Lambda > 600$ MeV, the initial parameter space was increased to ensure a non-implausible volume was located. Units for each LEC may be found in Eq. (8.2).

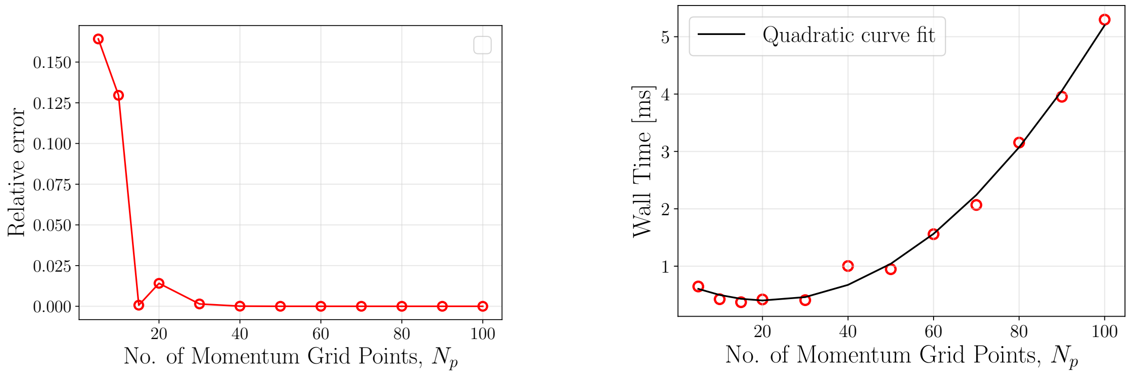

(a) **(b)**

Figure 8.1: The absolute relative error between SGT calculations achieved for a given N_p, and the corresponding calculation obtained at $N_p = 100$. Also shown is the time taken for each computation of an observable at a given N_p.

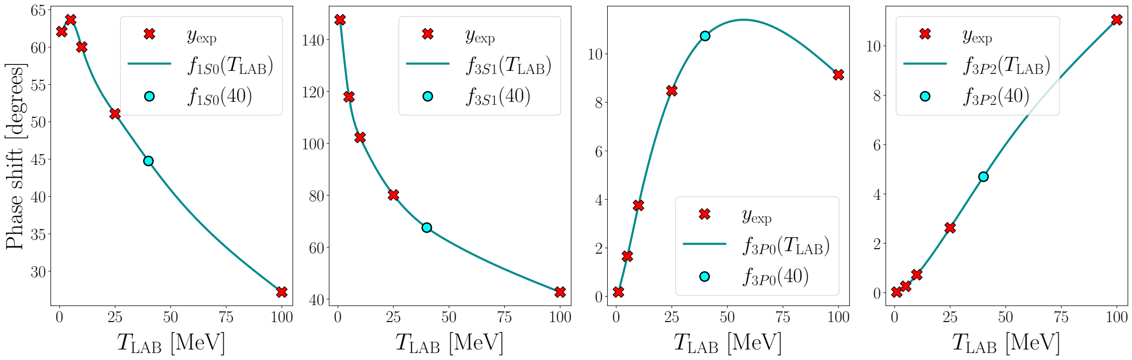

Figure 8.2: Phase shift data from the Granada database, corresponding to partial waves ${}^1S_0$, ${}^3S_1$, ${}^3P_0$, and ${}^3P_2$, within *np* scattering. Since phase shifts are not available at $T_{\text{Lab}} = 40$ MeV, data at this energy was obtained through spline interpolation (shown by solid lines) and is indicated in blue.

8.2.1 Wave 1 — Phase Shifts

The lab energies $\boldsymbol{T}_{\text{lab}}$ considered during the first wave of history matching are

$$\boldsymbol{T}_{\text{lab}} \equiv (1,\ 5,\ 10,\ 25,\ 40,\ 100)\ \text{MeV}. \tag{8.4}$$

Data for *np* scattering phase-shifts is taken from the Granada database [14, 15]. Corresponding experimental uncertainties are provided alongside the data in the form of standard deviations σ_{exp}, and are small in size. The model uncertainties used are $\sigma_{\text{model}} = 0.3 \cdot y_{\text{obs}}$ for $T_{\text{Lab}} \leq 40$ MeV and $\sigma_{\text{model}} = 0.8 \cdot y_{\text{obs}}$ for $T_{\text{Lab}} \sim 100$ MeV.

There is no data available within the Granada database for $T_{\text{Lab}} = 40$ MeV, but phase shifts at this value are easily obtained through spline interpolation. The data used, along with the $T_{\text{Lab}} = 40$ MeV phase shift obtained through interpolation, can be seen in Fig. 8.2. Phase shifts from partial waves ${}^1S_0$, ${}^3S_1$, ${}^3P_0$, ${}^3P_2$ are used, which combined with the six T_{Lab} energies gives an observation data vector $\boldsymbol{z}$ of length 24.

Since each LEC is dependent only on its respective partial wave, the first wave of history matching was split into four sub-waves. Each of the four sub-waves uses data from only one partial wave, corresponding to the data shown in each respective subplot of Fig. 8.2. In each sub-wave, a single LEC is active. The LECs not considered in the sub-wave are inactive parameters and set to arbitrary values. The benefit of this approach is that each LEC can be constrained independently, requiring fewer model evaluations in total. The output of each sub-wave is a one-dimensional range of non-implausible parameter values for each LEC. These ranges are then used to define a four-dimensional parameter volume to be searched in wave 2.

A generous implausibility cut-off of $I_{2M} < 3$ was chosen for each of the sub-waves, where we refer to Section 2.1 in which I_{2M} was introduced as the second maximum implausibility value. This choice was motivated by the fact that our assignment of σ_{model} is uncertain and a further reduction of samples is expected in wave 2.

8.2.2 Wave 2 — Observables

In the second wave of history matching, phase shifts are no longer used as the set of observational data. Instead, *np* scattering observables are introduced. The observables correspond to the total cross section (SGT), differential cross section (DSG), and polarisation of the beam (PB). The full set of experimental data, consisting of 13 observational datapoints, may be found in Table 8.3. The data spans the energy range of $0.12 \leq T_{\text{Lab}} \leq 99$ MeV.

Observable	y_{obs}	T_{Lab} [MeV]	Angle [deg]	$\sigma_{\text{model}}/y_{\text{obs}}$	Reference
SGT	12050.0 mb	0.12	-	0.3	[64]
SGT	2206.0 mb	3.186	-	0.3	[65]
SGT	749.0 mb	12.995	-	0.3	[66]
SGT	321.5 mb	28.0	-	0.3	[67]
SGT	217.8 mb	40.0	-	0.3	[67]
SGT	76.0 mb	97.2	-	0.8	[68]
DSG	8.01 mb/sr	99.0	21.0	0.8	[69]
DSG	2.14 mb/sr	99.0	78.0	0.8	[69]
DSG	9.50 mb/sr	99.0	149.0	0.8	[69]
PB	0.047	25.0	33.1	0.3	[70]
PB	0.053	25.0	90.3	0.3	[71]
PB	0.170	95.0	29.8	0.8	[72]
PB	0.291	95.0	88.5	0.8	[72]

Table 8.3: *np* scattering observables used within the second wave of history matching. Each datapoint is given alongside the experimental value y_{obs}, lab-energy T_{Lab}, angle, and the model uncertainty relative to the observational data $\sigma_{\text{model}}/y_{\text{obs}}$.

A summary of both waves of the history match is given in Table 8.4, where the number of observables used, the number of parameters (dimensionality), and the chosen implausibility cutoffs can be found. The choice of implausibility cutoffs in wave 2 is guided by Ref. [11], where a sequence of cutoffs is implemented; Both the first and second maximum implausibilities, denoted I_M and I_{2M} respectively, are used with imposed cutoffs of 3.0 and 2.5, respectively.

Wave	Sub-wave	LECs	Dim.	No. Samples	No. of Observables	Cutoffs	
						I_M	I_{2M}
1	1	$\widetilde{C}_{^1S_0}$	1	10^4	6	-	3.0
1	2	$\widetilde{C}_{^3S_1}$	1	10^4	6	-	3.0
1	3	$C_{^3P_0}$	1	10^4	6	-	3.0
1	4	$C_{^3P_2}$	1	10^4	6	-	3.0
2	-	All	4	10^5	13	3.0	2.5

Table 8.4: Summary of the two waves of history matching of χEFT in the *np* sector. Dim. refers to the dimensionality of the parameter space in the corresponding wave (or subwave).

8.3 Results for Cutoff $\Lambda = 450$ MeV

A plot of I_{2M} across parameter ranges, obtained in wave 1 of the history match, is shown in Fig. 8.3. The non-implausible parameter ranges, corresponding to the range in which $I_{2M} < 3$, is indicated. The lower limit of the $\widetilde{C}_{^3S_1}$ non-implausible range reaches the lower limit of the parameter space searched, suggesting that more negative parameter values may also be non-implausible. However, this was not thought to pose a problem since a further reduction of this region was expected when introducing scattering observables to the history match, and thus the history match was continued into the second wave.

Fig. 8.3 also confirms that the use of only phase shifts in wave 1 successfully reduces the parameter space. Upon investigation of the non-implausible region achieved after each sub-wave, seen in Table 8.5, $C_{^3P_0}$ and $C_{^3P_2}$ achieve a greater percentage reduction than $\widetilde{C}_{^1S_0}$, $\widetilde{C}_{^3S_1}$. We note that the initial ranges for $C_{^3P_0}$ and $C_{^3P_2}$ are at least an order of magnitude greater than those of $\widetilde{C}_{^1S_0}$ and $\widetilde{C}_{^3S_1}$. Therefore, this is not a particularly surprising result. However, it is still of interest to investigate model sensitivity to parameters in order to gain a deeper understanding of the process occurring in wave 1. This investigation is discussed in Section 8.3.1.

Calculations of the size of the non-implausible volumes remaining after each wave (or sub-wave) are given in Table 8.5. The final results of the history match can be seen in Fig. 8.4. We note that the introduction of scattering observables into the history match does decrease the total non-implausible volume, but only with respect to $\widetilde{C}_{^3S_1}$ and $C_{^3P_2}$. However, upon plotting the remaining non-implausible samples (red dots), it does appear that an additional number of samples *inside* the volume were deemed implausible, with respect to all LECs.

Wave	Sub-wave	LECs	NI samples (%)	NI volume (%)
1	1	$\widetilde{C}_{^1S_0}$	59.2	59.2
1	2	$\widetilde{C}_{^3S_1}$	41.4	24.5
1	3	$C_{^3P_0}$	11.4	2.79
1	4	$C_{^3P_2}$	3.0	0.08
2	-	All	5.27	0.045

Table 8.5: Quantitative results of the history match of χEFT at LO in MWPC, performed at $\Lambda = 450$ MeV. Shown are the number of non-implausible (NI) samples, given as a percentage of the total number of samples generated in the given wave/sub-wave. Also shown is the non-implausible volume remaining after each wave/sub-wave. All volumes are given as a percentage of the four-dimensional initial parameter volume prior to wave 1.

Performing an initial history match at $\Lambda = 450$ MeV provides the benefit of being able to somewhat validate the results, either with existing literature values [61, 63] or current ongoing studies [13]. A comparison with such values is shown in Fig. 8.5. These values correspond to modes of LEC posteriors obtained using MCMC sampling. The values are confirmed to fall within the final non-implausible regions of $\widetilde{C}_{^1S_0}$ and $\widetilde{C}_{^3S_1}$.

There are no values available for $C_{^3P_0}$ and $C_{^3P_2}$ from Ref. [63], since the study implements WPC, and therefore $C_{^3P_0}$ and $C_{^3P_2}$ are only introduced at NLO[1]. The posterior modes from Ref. [61] agree well for $C_{^3P_0}$ but fall outside of the non-implausible region for $C_{^3P_2}$. However, this posterior was obtained using only low-energy data ($T_{\text{Lab}} \leq 40$ MeV) and so some discrepancy is expected. The value from Ref. [13] was obtained in conjunction with the study performed in this thesis and therefore used comparable observational data and uncertainties. It falls within the non-implausible volume in all dimensions.

Plots representing the optical depth and implausibility measure of the non-implausible volumes obtained at the end of wave 2 may be found in Fig. 8.6. We refer back to Section 7.2 for an explanation of optical depth, and Eq. (2.5) for the implausibility measure. We note both a high density of non-implausible samples (indicated by high optical depth) and low implausibility for less attractive (negative) values of the LECs, implying that these LECs tend to produce observables more consistent with data. However, a full Bayesian analysis is required to make a probabilistic interpretation of these results. We also note that the densest and least implausible regions lie near the edge of the final non-implausible volume. These particular volume boundaries are those achieved in wave 1. It is therefore possible that, without the use of phase shifts in wave 1, the final non-implausible volume would be notably larger. This suggests that phase shifts more strongly constrain the volume than scattering observables. This is especially notable when considering the more generous implausibility cutoff used in wave 1 than in wave 2.

---

[1] Since several more LECs are also introduced at NLO, posterior modes for $C_{^3P_0}$ and $C_{^3P_2}$ are unsuitable for comparison with MWPC LO results.

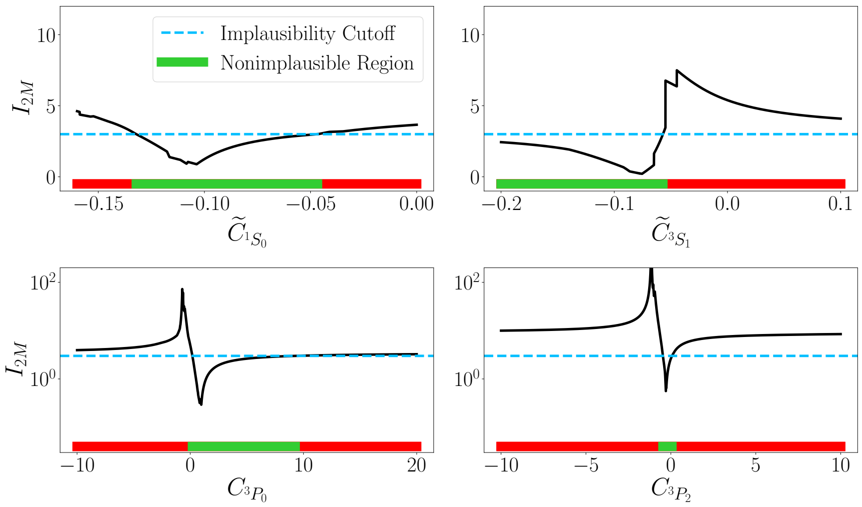

Figure 8.3: The second-maximum implausibility I_{2M} obtained in each sub-wave of wave 1 of the history match. The implausibility cut-off and the non-implausible regions are also shown.

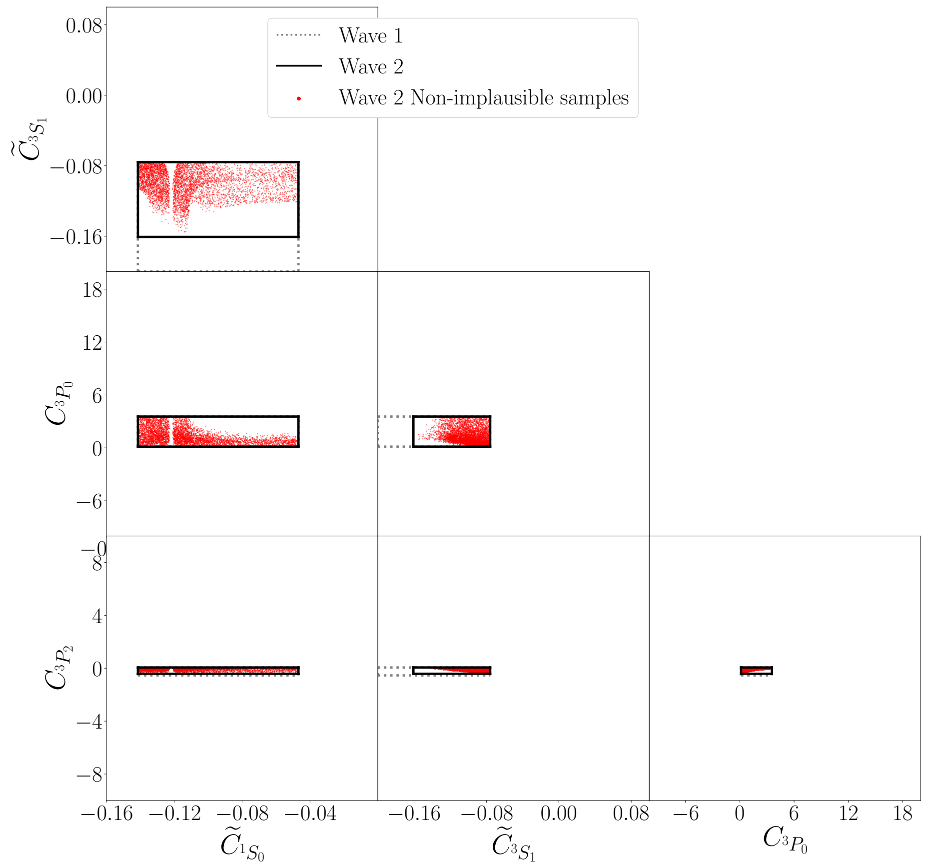

Figure 8.4: Results of the history match of χEFT for cutoff $\Lambda = 450$ MeV, in the form of a corner plot. The regions indicated by the dotted lines are the non-implausible volumes obtained after wave 1. Solid lines indicate the non-implausible volumes obtained after wave 2. Also shown are the non-implausible samples remaining after wave 2 (red dots).

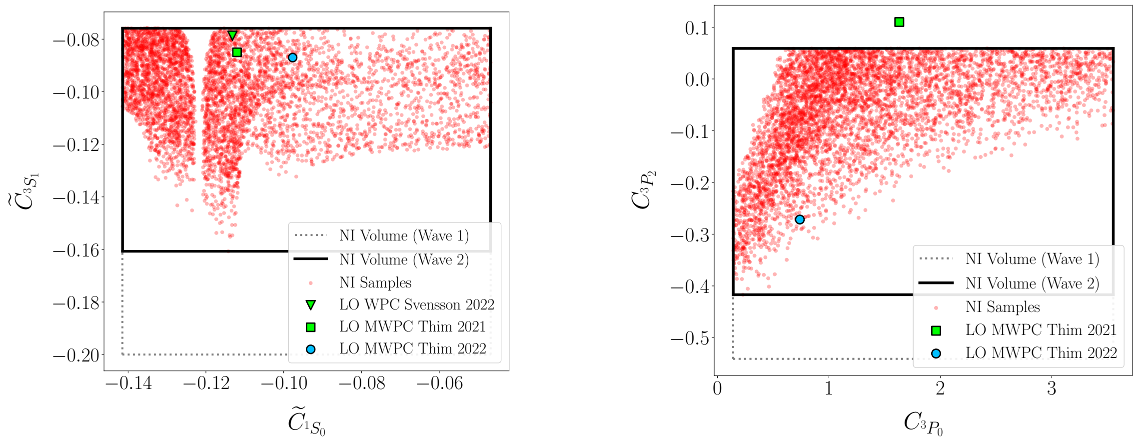

Figure 8.5: A close up of two two-dimensional projections of the non-implausible volume of LECs. In (a), the non-implausible regions obtained in wave 1 and wave 2 are shown, for parameters $\widetilde{C}_{^1S_0}$ and $\widetilde{C}_{^3S_1}$. In (b), the same is shown for parameters $C_{^3P_0}$ and $C_{^3P_2}$. In both plots, the final set of non-implausible samples (red dots) is also shown. The green scatter points correspond to modes of posteriors obtained for the LECs, given in Refs. [61, 63]. Note that Ref. [63] used WPC at LO so no values are available for $C_{^3P_0}$ and $C_{^3P_2}$. The blue scatter point indicates the mode of the posteriors obtained by O. Thim [13] using a comparable set of observables and uncertainties.

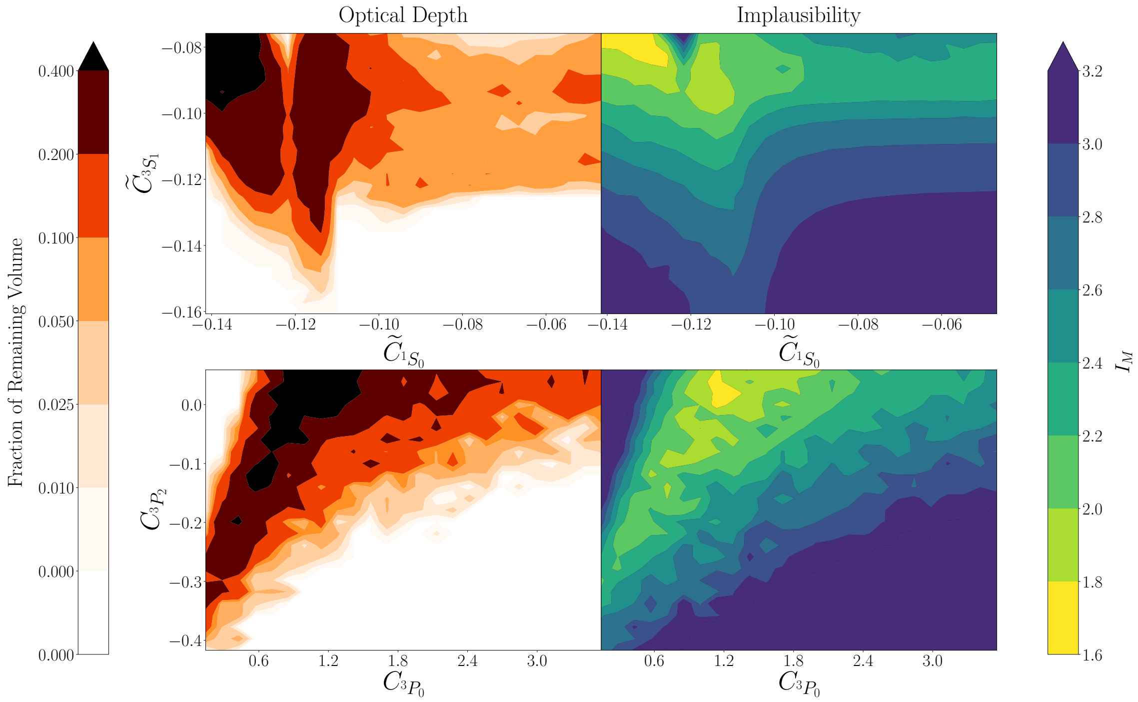

Figure 8.6: Optical depth and implausibility I_M, obtained at the end of wave 2, are plotted as heat maps. The parameter ranges correspond to the span of the final non-implausible volume.

8.3.1 Model Sensitivity to LECs

A sensitivity analysis of wave 1 of the history match performed at $\Lambda = 450$ MeV can be found in Fig. 8.7, where the variation in model output across the initial parameter range is shown (the filled pink region). Note that, in the case of $C_{^3P_0}$ and $C_{^3P_2}$, the model output is discontinuous. Also shown are the phase shifts used in wave 1 as y_{obs} with corresponding $\pm 3\sigma$ uncertainties including both σ_{obs} and σ_{model}. A random selection of 100 non-implausible samples remaining after wave 1 were used to generate model outputs (green lines), which are confirmed to fall within nearly all $y_{\text{obs}} \pm 3\sigma$ regions. We note that the use of $I_{2M} > 3$ as the implausibility cutoff in wave 1 explains why not all non-implausible samples leads to outputs inside every 3σ range. The choice of initial parameter space to search leads to samples deemed as implausible for each LEC and across the entire energy range. This confirms a reasonable choice of parameter space to search. However, the initial lower boundary of $\widetilde{C}_{^3S_1}$ does appear to limit the space searched and it is likely that non-implausible samples would still occur for more negative parameter values in this case. As discussed previously, it was expected that the introduction of scattering observables will further constrain $\widetilde{C}_{^3S_1}$. As seen in Fig. 8.4, this expectation was shown to be correct. It is unlikely that any increase in the initial parameter space would have had an effect on the final non-implausible volume [2].

Introducing scattering observables in wave 2 does not lead to a large reduction in the non-implausible volume. The only reduction occurs for $\widetilde{C}_{^3S_1}$ and $C_{^3P_2}$. As before, an analysis of the sensitivity of model output on LECs is performed. Fig. 8.8 shows the variation in model output across the parameter space searched, and the model output for 100 of the final non-implausible samples. Low-energy observables, such as low-energy SGT and PB, appear to lead to higher variations in model output than the high-energy data. Combined with the lower model uncertainty in these cases, it is these observables that appear to most constrain the non-implausible volume. High-energy data does not appear to lead to much reduction in parameter space, potentially due to the high model uncertainty used for this data. However, the DSG datapoint at 78° appears to be an exception to this case, somewhat justifying the inclusion of high-energy data.

---

[2] It cannot be claimed for certain that non-implausible samples would not have appeared at more negative values in wave 2, but non-implausible regions at these values likely correspond to unphysical bound states. They are therefore not particularly 'plausible' when considering the physics. See Section 8.5 for further discussion.

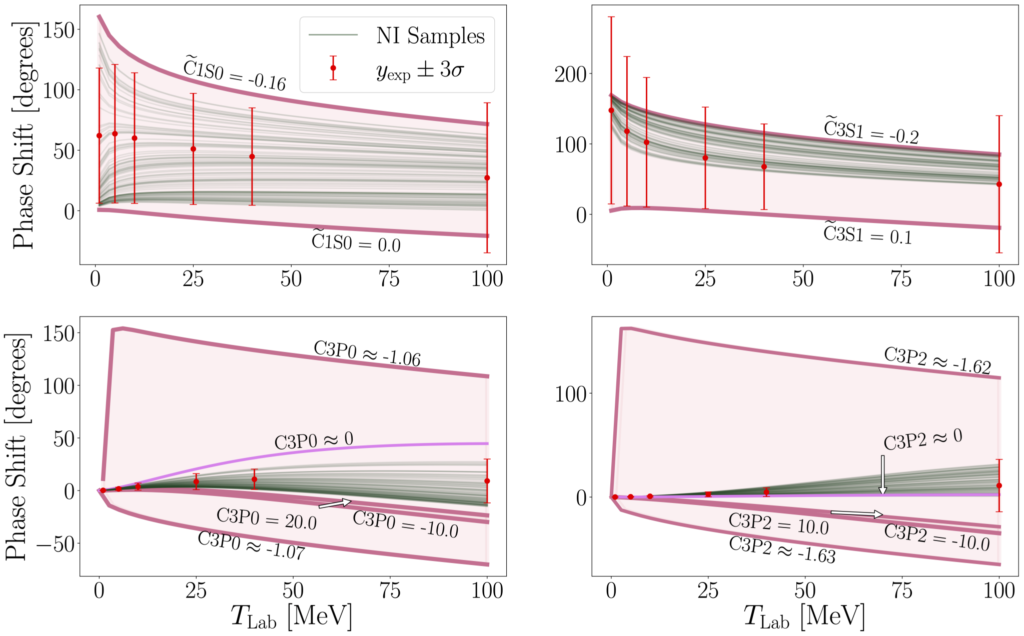

Figure 8.7: Variation in phase shifts across a range of T_{Lab} values, using Λ=450 MeV. The filled pink regions correspond to the range of model outputs achieved across the initial parameter space. A set of 100 random non-implausible samples (green lines) are also shown. The $C_{^3P_o} \approx 0$ and $C_{^3P_2} \approx 0$ lines correspond to the case if LO in WPC had been implemented, as opposed to LO in MWPC.

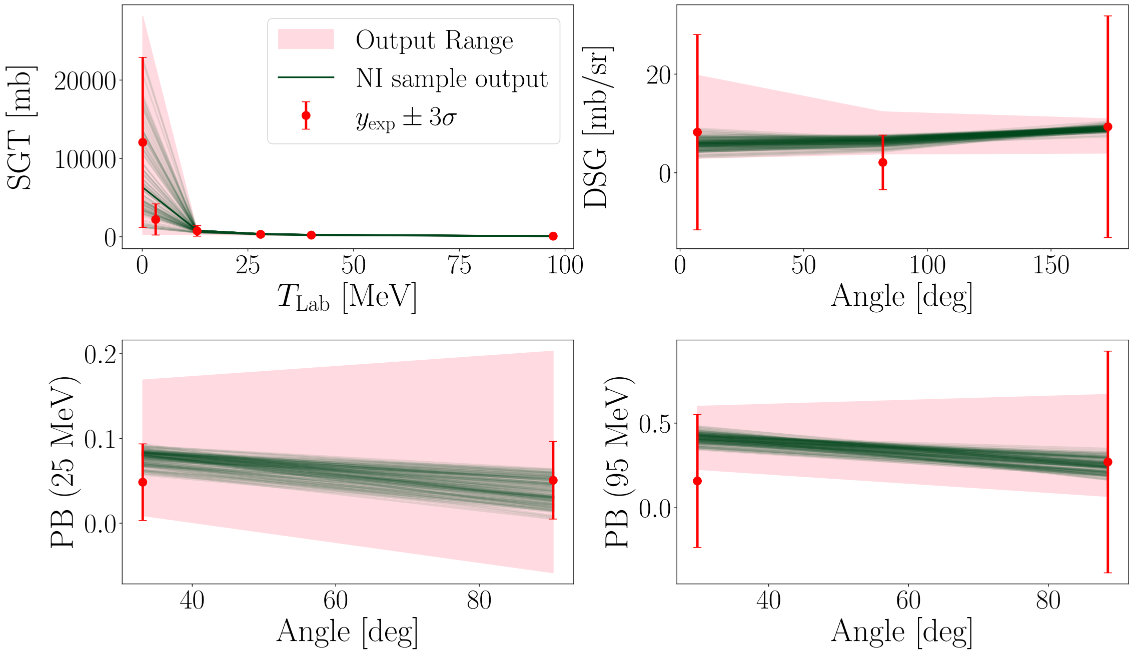

Figure 8.8: The variation in model output for scattering observables, using Λ=450 MeV. The filled range corresponds to the range in model output achieved across the parameter space searched in wave 2 of the history match. The green lines correspond to 100 samples taken from the set of non-implausible samples obtained after wave 2.

8.3.2 Prediction of the Deuteron Binding Energy

In order to both validate the non-implausible LEC volume obtained at $\Lambda = 450$ MeV and to illustrate the capabilities of history matching, each non-implausible LEC sample was used to compute the binding energy of the deuteron. A histogram of the results is given in Fig. 8.9, with the empirical binding energy also indicated. Note that the histogram is only an indication of the frequency that a predicted value appears, and it is *not* a probability distribution. The empirical value successfully falls within the range of predicted binding energies, but the histogram tends towards lower binding energies.

In order to illustrate the reason for both the wide range and the tendency of the predictions towards lower values, the final non-implausible samples with respect to $\widetilde{C}_{^3S_1}$ and $\widetilde{C}_{^1S_0}$ are plotted. There is clearly a much higher density of samples within the area that produces lower binding energies. As emphasised before, history matching is a likelihood free method and it is therefore unreasonable to expect precise observable predictions without a probabilistic interpretation of the parameters.

In Fig. 8.10, predictions of the deuteron binding energy and the SGT observable are given, corresponding to each of the non-implausible samples, at $\Lambda = 450$ MeV. Since SGT is dependent on more than one LEC, we now see a wider spread of predictions.

Both Fig. 8.9 and Fig. 8.10 suggest that the non-implausible volume would be further constrained by including the ^{2}H binding energy observable within the history match. This is illustrated by the 3σ region (grey shaded area) shown in both figures, where $\sigma = \sigma_{\text{model}} = 0.3y_{\text{obs}}$, with y_{obs} being the deuteron binding energy. This value was chosen to be consistent with the uncertainties used in this history match. Since the binding energy of the deuteron is primarily dependent on $\widetilde{C}_{^3S_1}$, the non-implausible range of this LEC could be significantly reduced to the region bounded by the red dashed lines in Fig. 8.9. Additionally, it is likely that the other LECs will also be constrained as they attempt to reproduce the observable, working within the reduced $\widetilde{C}_{^3S_1}$ range, as seen in Fig. 8.10. This is desirable if the aim is to predict more precise observable values, or to simply obtain a more constrained non-implausible volume.

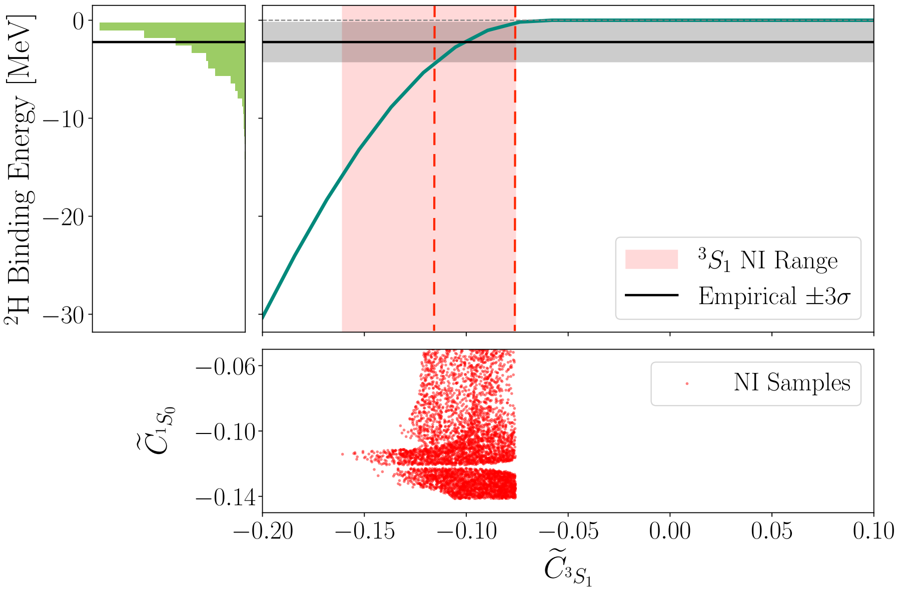

Figure 8.9: Deuteron binding energy as a function of $^3S_1$ (dark green curve). The leftmost plot is a histogram of predicted deuteron binding energies using the set of non-implausible LECs. The red shaded area in the upper right plot indicates the non-implausible range obtained after wave 2 of the history match of χEFT at $\Lambda = 450$ MeV. The area contained within the red dashed lines corresponds to a further constrained parameter range, if deuteron binding energy is included as an observable within the history match.

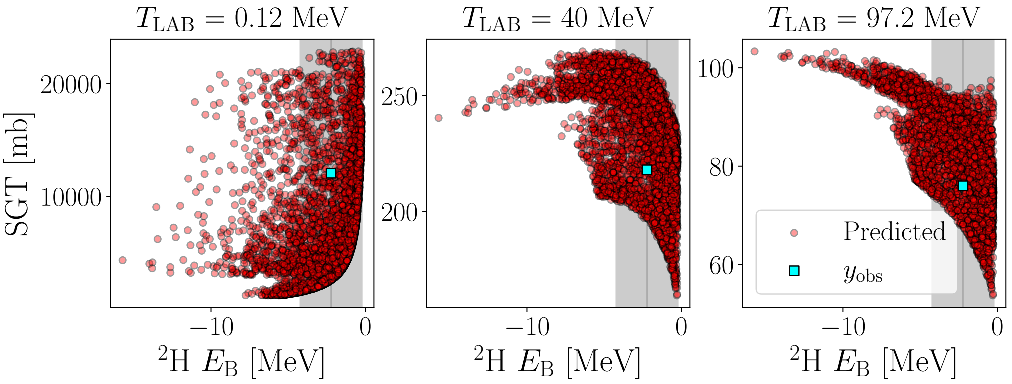

Figure 8.10: Deuteron binding energy and SGT predictions given by each remaining non implausible sample after the history match of χEFT at $\Lambda = 450$ MeV. The blue point corresponds to the empirical ^{2}H binding energy and experimental SGT values at the corresponding energy.

8.4 Results for Alternate Cutoffs

As detailed in both Section 4.4.1 and Section 8.2, a new history match of the χEFT model must be performed if the value of Λ is varied, since the LECs are dependent on the choice of Λ. The history match, as described in the previous section, was run for $400 \leq \Lambda \leq 4000$ MeV. Fig. 8.11 shows the non-implausible ranges for each LEC at a given Λ. If multiple modes were seen within the non-implausible volume, then the range spanned by each mode is plotted and coloured either green or red. Red regions are labelled as 'unphysical bound states', the reasoning of which is discussed in Section 8.5.

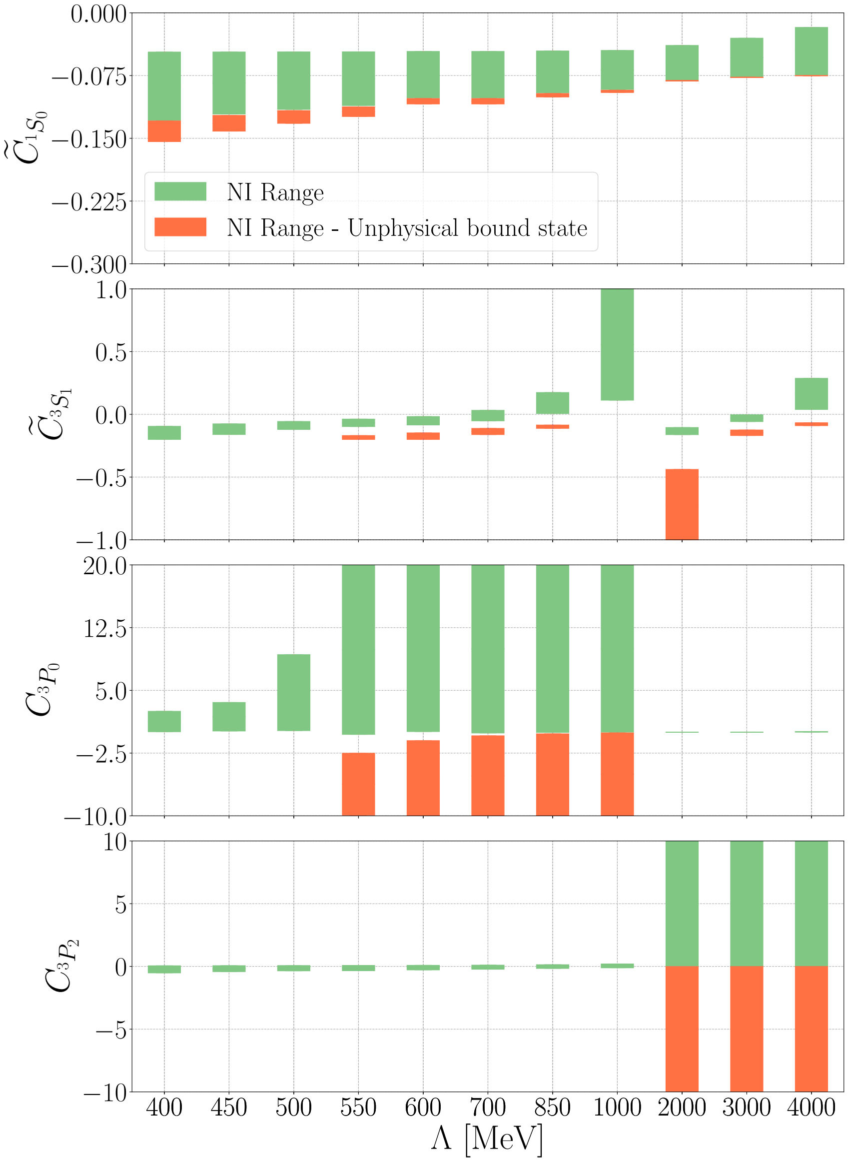

Figure 8.11: Non-implausible ranges for each LEC, obtained running a history match for a given momentum cutoff Λ. Volumes displaying multimodal behaviour were split into separate regions and visualised accordingly, where unphysical bound states are indicated in red.

8.4.1 Sensitivity Analysis for Alternate Cutoffs

A further qualitative sensitivity analysis was performed for $400 \leq \Lambda \leq 600$ MeV. An investigation of low-energy PB is shown in Fig. 8.12. SGT, high-energy PB, and DSG sensitivity analyses may be found in Appendix A, in Figs. A.3, A.4, and A.5, respectively. Observables were computed by varying each LEC independently across the initial LEC range searched in wave 1, and setting the remaining LECs as constants corresponding to the sample remaining after wave 2 with the lowest value of I_{2M} (for a given Λ). Model outputs that fall outside of the $y_{\text{obs}} \pm 3\sigma$ region would receive an implausibility above the I_M cutoff during the history match. Therefore, a simplified interpretation of these plots is that the areas of the curves that fall outside the shaded 3σ region are implausible regions. The results confirm those seen in Fig. 8.8, where low-energy SGT, low-energy PB, and the DSG datapoint at 78° appear to most constrain the history match.

Several important notes must be made about this sensitivity investigation. Firstly, the x-axis corresponds to the *initial* parameter ranges searched in wave 1 and LECs leading to model outputs outside the 3σ region may already be classed as implausible after wave 1. This explains why we do not see a significant reduction in parameter volume in wave 2, despite some observables showing high sensitivity to the LECs. Furthermore, the outputs plotted were computed for the LEC with the lowest implausibility and thus samples far from this LEC would produce outputs more often outside of the 3σ region. However, it is likely that in the case of some observables, e.g. high-energy SGT, sensitivity to LECs is so low and model uncertainty is so high that these observables rarely, if ever, result in a high implausibility value. Another important point to note is that the second wave of history matching utilises a second maximum implausibility cutoff of $I_{2M} > 2.5$ (see Table 8.4). As such, some observables shown will be 'compared' to a region smaller than the 3σ region visualised.

An interesting feature of Figs. 8.12 and A.4 is the appearance of negative values of PB at some values of the LECs. PB is defined such that its sign is positive [73], and it is thought that the negative outputs of our model are an artifact of the truncation of χEFT. Although this truncation error has been incorporated into the model discrepancy used within the history match, the negative model outputs still fall outside of the 3σ region and may contribute to deeming a sample implausible. Although out of the scope of this thesis, a further investigation of the model uncertainty may be appropriate in the case of these observables.

With these considerations in mind, the sensitivity analyses allow us to gain a better understanding of our history match. In all the sensitivity analyses, the peaks in model output tend to occur near the centre of the parameter ranges rather than at the extreme values. This suggests that using phase shifts in wave 1 to constrain the parameter space was a sensible choice, as it appears that observables in wave 1 would not have led to such a large reduction.

Despite observables not leading to a significant volume reduction in wave 2, the sharp peaks suggest that many samples within our volume are still being classed as implausible. This explains the multi-modal regions of parameter space for $\widetilde{C}_{^1S_0}$ at all Λ, and $\widetilde{C}_{^3S_1}$ and $C_{^3P_0}$ at $\Lambda = 600$ MeV. Since the non-implausible volume is defined only as a hyperrectangle around all non-implausible samples, this behaviour is only visible upon investigation of which samples remain after wave 2, as in Fig. 8.4, or if the optical depth is visualised, as in Fig. 8.6. A further discussion of the multi-modal behaviour takes place in Section 8.5.

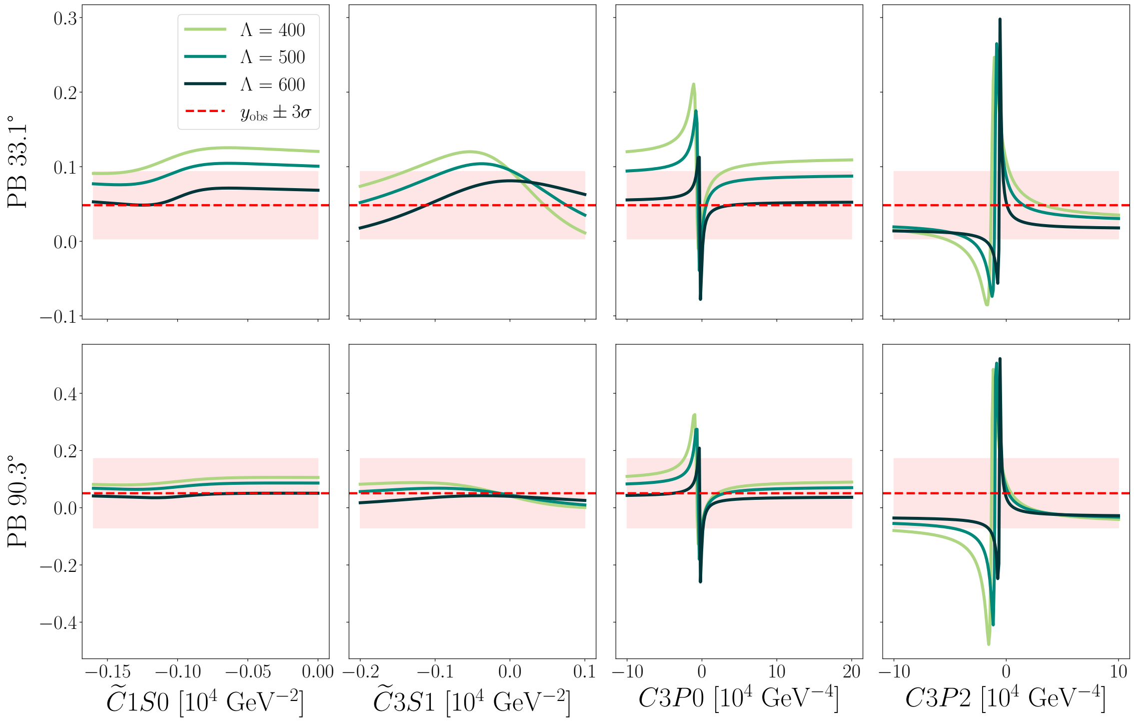

Figure 8.12: PB at a given angle, computed across ranges of each LEC. All values of PB in this plot were computed at T_{Lab}=25 MeV.

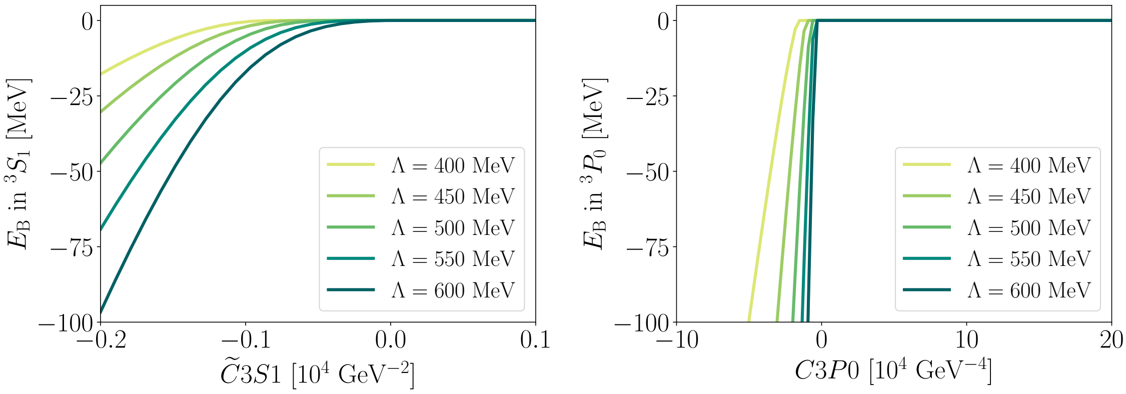

Figure 8.13: Ground-state energy of the np system in the $^3S_1$ and $^3P_0$ channels. Calculations were performed across the explored ranges of $\widetilde{C}_{^3S_1}$ and $C_{^3P_0}$, and for a range of Λ values.

8.5 Multi-Modal Behaviour

Multi-modal non-implausible regions appear for several of the LECs across all cutoffs Λ. We begin by discussing the multi-modal behaviour of $\widetilde{C}_{^1S_0}$. Due to the likelihood-free nature of history matching, probabilities are not assigned to any region of parameter space. It is therefore not possible to determine which of the two modes in $\widetilde{C}_{^1S_0}$ is the most probable region[3]. However, we can analyse the regions by considering the existence of bound states within the relevant channel. A sufficiently attractive potential will support a bound state. We therefore suggest that a bound state is occurring when the value of the LEC becomes too negative (attractive).

However, it is known that the only physical bound state occurring in the NN system is the $^3S_1$-$^3D_1$ deuteron state [31], and thus there is *not* a bound state in the $^1S_0$ channel. Since multiple modes appear within $\widetilde{C}_{^1S_0}$ for all Λ, we conclude that this bound state is most likely a consequence of using a LO description in MWPC.

Interestingly, additional modes begin to appear for some values of $\Lambda \geq 550$ MeV, within $\widetilde{C}_{^3S_1}$ and $C_{^3P_0}$. Since these modes do not appear for all values of Λ, it is thought that their existence is due to the use of a regulator function (see Section 4.4.1). We therefore deem these regions as 'unphysical', despite the fact that the LECs produce model outputs consistant with observational data.

To investigate the hypothesis that the multi-modal regions correspond to unphysical bound states, the binding energy was computed across the relevant parameter ranges, as shown in Fig. 8.13. If the potential is sufficiently attractive, the eigenspectrum of the Hamiltonian contains at least one negative eigenvalue. States in which $E < 0$ are bound states. We consider bound states to be unphysical if we see an unreasonably high (in magnitude) binding energy (see Section 8.3.2 for the reasonably sized deuteron binding energy for reference). As seen in the figure, increasing Λ leads to a steeper gradient in binding energy. This suggests that, for higher Λ, less attractive values of the LECs are required for unphysical bound states to appear. This explains why an increasing number of distinct non-implausible regions are found for $\widetilde{C}_{^3S_1}$ and $C_{^3P_0}$ during high-Λ history matches.

---

[3] The most probable region can be interpreted either as the region most consistent with observational data, or the region agreeing with the physics upon which χEFT is based. The first cannot be analysed with history matching alone and requires a full Bayesian analysis. However, the second interpretation can be analysed.

Chapter 9

Conclusion and Outlook

9.1 Conclusion

The focus of this thesis has centred on two distinct areas: Validation and improvement of the method of history matching, and the application of history matching to explore the LO χEFT description of the NN system.

In Chapter 2, the method of history matching was introduced and supplemented by a discussion on Gaussian process emulators. In Chapter 3, the fundamentals of χEFT were covered. It was beyond the scope of this thesis to discuss the many concepts at work within χEFT. Instead, the motivation behind the theory was briefly discussed and power counting was described as a method of constructing a working model to describe nuclear interactions. Finally, LECs within χEFT were introduced as a set of unknown parameters and history matching was proposed as a method of exploring the model performance in the high-dimensional space of the LECs. In Chapter 4, the basics of scattering theory were covered with the aim of explaining how scattering observables are obtained from an interaction potential.

In Chapter 5, the limitations of history matching were addressed through the introduction of several novel sampling methods within a subtask of history matching. The methods were developed to capture correlations between parameters, and did so within their definition of a *non-implausible volume*.

In Chapter 6, the nuclear liquid drop model was introduced as a toy model and used for validation of the history matching scheme. The setup of the validation was explored in detail. In Chapter 7, the results of the history match of the liquid drop model were presented. Posterior parameter distributions, obtained analytically, were confirmed to fall within the acquired non-implausible volumes. The results were accompanied by an investigation into the sampling density required by each non-implausible volume definition. It was concluded that an ellipsoidal non-implausible volume displayed the most promising results; Correlations were successfully captured, and a higher sample resolution indicated improved computational efficiency.

Armed with a validated history matching scheme, a study of the χEFT model was presented in Chapter 8. History matches were performed for cutoffs $400 \leq \Lambda \leq 4000$ MeV and non-implausible volumes were located in parameter space for every case. The most notable result arising from the analysis was the appearance of multi-modal regions of parameter space, including domains corresponding to unphysical bound states. Finally, the non-implausible samples obtained at $\Lambda = 450$ MeV were used to predict the deuteron binding energy. The results suggested that the inclusion of such an observable could further constrain the final non-implausible volume.

In conclusion, the history matches performed in this thesis have lead to the successful identification of non-implausible volumes within parameter space, both in the case of the nuclear liquid drop model and χEFT. The strength of history matching lies in its ability to locate *all* non-implausible parameter regions[1] rather than a single, optimal value typically obtained by Frequentist methods. The simultaneous appearance of multi-modal regions of parameter space seen in Chapter 8 therefore represent one of the strongest assets of history matching — insight into the model itself.

Furthermore, history matching is not bound by the challenges most often encountered working within a Bayesian framework. It does not require a detailed specification of a prior, nor the functional form of the likelihood to be known. However, global parameter searches are challenging and this thesis identified that the history matching approach often fails to capture correlations between parameters if implementing hyperrectangle sampling according to upper and lower parameter bounds, as in Refs. [10, 11, 17]. Promisingly, this thesis suggests that this issue may be successfully combated through the construction of rotated hyperrectangle, Gaussian, or ellipsoid non-implausible volumes. As mentioned above, we recommend the use of an ellipsoid non-implausible volume for this purpose.

9.2 Outlook

There exist several areas in which the study performed in this thesis could be improved or developed in the future.

9.2.1 Full Bayesian Analysis

One general use of history matching is that of a precursor for a full Bayesian analysis. One may wish to use history matching such that the parameter space is reduced prior to performing analyses that would be computationally costly to evaluate over the entirety of the space.

An example of a popular Bayesian analysis is MCMC. A non-implausible volume obtained through history matching, could indicate where a posterior probability distribution, obtained through MCMC, may lie in parameter space. Using this knowledge, MCMC walkers can be initialised in the parameter volume obtained from a

---

[1] Assuming a high enough sample resolution is achieved, and all relevant areas of parameter space are explored.

history match. More specifically, initial walker positions can be set to that of non-implausible parameter samples. Initialising walkers closer to an expected posterior mean has the potential benefit of aiding the speed at which convergence of MCMC is reached.

This potential outlook has been successfully demonstrated in a current study. This thesis obtained sets of non-implausible samples from the history match of χEFT, at varying values of momentum regulator cutoff Λ. At the time of publication of this thesis, these samples are currently used as initial positions for walkers within an MCMC analysis of χEFT at LO in MWPC [13]. The current status, and short-term outlook, of this collaboration is to perform further analysis of the non-implausible regions in relation to the MCMC results. In particular, the sensitivity analysis performed in Section 8.3.1 provides some insight into the behaviour of LECs and the appearance of bound states at higher values of Λ.

9.2.2 Location of Sample Clusters

A potential improvement to the history matching scheme developed in this thesis is the implementation of automatic functionality within the history matching scheme to handle multi-modal behaviour. The benefit of successfully locating clusters during a history match is that sub-waves of history matching could be performed on each separate cluster. This would avoid the construction of a single volume enclosing all separate non-implausible regions, and prevent needlessly sampling the ‘empty’ space between regions. Furthermore, if performing history matches on each individual region, a higher sample density would be achieved. This is also beneficial if using emulators, since different emulators could potentially be constructed for each separate and *smaller* region of parameter space, consequently increasing emulator accuracy.

Manual identification of multiple modes is difficult in high-dimensional spaces. This motivates the need for an automatic algorithm. One approach could include the ability to locate distinct regions in parameter space using a clustering algorithm. Clustering algorithms generally operate by grouping sets of points in a multi-dimensional space, based on a chosen distance metric. Pre-developed clustering methods exist within various `Python` libraries, including `scipy`. However, these methods generally require the number of clusters to be known. Alternatively, there are methods implemented within nested sampling that could be used for this purpose [74].

The challenge involved in the implementation of clustering algorithms is ensuring that regions within parameter space are correctly identified without the need for checks throughout the history match. The tuning of hyperparameters within the clustering algorithm would also requires careful consideration, as it would need to be performed for each wave of a history match.

9.2.3 Eigenvector Continuation Emulators

Emulators are a core feature of history matching and an essential alternative to computationally expensive simulations. They are often one of the primary reasons that an iterative reduction in parameter space can be achieved. A Gaussian process emulator was implemented during the toy model validation performed in this thesis. However, no emulator was implemented during the history match of LECs due to the limited computational complexity of the calculations required in this thesis, demonstrated by the small computational time given in Figure 8.1b.

However, the use of emulators within nuclear physics is a fast developing and exciting area and could be a useful addition to the implementation in this thesis. The inclusion of emulators would speed up the history matching process and could allow one to include additional low-energy nuclear observables that are more costly to compute. If one wanted to explore higher orders of MWPC, the dimensionality of parameter space would quickly increase. In this case, an emulator may prove to be necessary to achieve realistic computation times.

Eigenvector continuation emulators [75] are an example of a type of emulator that would be interesting to see included within this history matching implementation. The use of such emulators has already shown to be successful upon application to χEFT [26, 76]. Another eigenvector continuation-inspired emulator is detailed in Ref. [77], where the idea of eigenvector continuation has been used to formulate an emulator specifically for the two-body scattering problem. It is therefore particularly relevant to the work performed in this thesis. The Lippmann-Schwinger equation is solved for a few cases such that a small matrix, e.g., a T-matrix, is obtained. Using Newton's variational method [78], an approximation to the entire scattering T-matrix may then be obtained. Referring back to Chapter 4, it is clear how this emulator could be directly applied within the history matching implementation to compute scattering observables.

Bibliography

1. Weinberg, S. Phenomenological Lagrangians. *Physica A* **96,** 327–340 (1979).
2. Weinberg, S. Nuclear forces from chiral lagrangians. *Phys. Lett. B* **251,** 288–292 (1990).
3. Weinberg, S. Effective chiral lagrangians for nucleon-pion interactions and nuclear forces. *Nucl. Phys. B* **363,** 3–18 (1991).
4. Epelbaum, E. *Nuclear forces from chiral effective field theory: a primer* 2010. arXiv: `1001.3229 [nucl-th]`.
5. Van Kolck, U. Few nucleon forces from chiral Lagrangians. *Phys. Rev. C* **49,** 2932–2941 (1994).
6. Machleidt, R & Entem, D. R. Chiral effective field theory and nuclear forces. *Phys. Rept.* **503,** 1–75 (2011).
7. Scherer, S. & Schindler, M. R. *A Primer for Chiral Perturbation Theory* ISBN: 978-3-642-19253-1 (Springer-Verlag Berlin, 2012).
8. Nogga, A, Timmermans, R. G. E. & van Kolck, U. Renormalization of One-Pion Exchange and Power Counting. *Phys. Rev. C* **72,** 054006 (2005).
9. Yang, C. J., Ekström, A., Forssén, C. & Hagen, G. Power counting in chiral effective field theory and nuclear binding. *Phys. Rev. C* **103,** 054304 (2021).
10. Vernon, I., Goldstein, M. & Bower, R. Galaxy Formation: Bayesian History Matching for the Observable Universe. *Statist. Sci.* **29,** 81–90 (2014).
11. Vernon, I. *et al.* Bayesian uncertainty analysis for complex systems biology models: emulation, global parameter searches and evaluation of gene functions. *BMC Syst. Biol.* **12,** 1 (2018).
12. Goldstein, M. & Wooff, D. *Bayes Linear Statistics: Theory and Methods* ISBN: 978-0-470-01562-9 (John Wiley Sons Ltd., 2007).
13. Thim, O., May, E., Ekström, A. & Forssén, C. In preparation. (2022).
14. Pérez, R. N., Amaro, J. E. & Arriola, E. R. Partial Wave Analysis of Nucleon-Nucleon Scattering below pion production threshold. *Phys. Rev. C* **88,** 024002 (2013).
15. Pérez, R. N., Amaro, J. E. & Arriola, E. R. Coarse-grained potential analysis of neutron-proton and proton-proton scattering below the pion production threshold. *Phys. Rev. C* **88,** 064002 (2013).
16. Andrianakis, I. *et al.* Reified Bayesian Modelling and Inference for Physical Systems. *SIAM-ASA J. Uncertain. Quantif.* **5(1),** 694–719 (2017).
17. Vernon, I., Goldstein, M. & Bower, R. Galaxy formation: a Bayesian uncertainty analysis. *Bayesian Anal.* **5(4),** 619–669 (2010).
18. Brynjarsdóttir, J. Learning about physical parameters: The importance of model discrepancy. *Inverse Probl.* **30,** 114007 (2014).

19. Pukelsheim, F. The three sigma rule. *Am. Stat.* **48,** 88–91 (1994).
20. Rasmussen, C. E. & Williams, C. K. I. *Gaussian Processes for Machine Learning* ISBN: 0-262-18253-X (The MIT Press, 2006).
21. Muta, T. *Foundations of Quantum Chromodynamics: An Introduction to Perturbative Methods in Gauge Theories, (3rd ed.)* 3rd. ISBN: 978-981-279-353-9 (World Scientific, Hackensack, N.J., 2010).
22. Gupta, R. *Introduction to lattice QCD: Course* in *Les Houches Summer School in Theoretical Physics, Session 68: Probing the Standard Model of Particle Interactions* (July 1997), 83–219. arXiv: `hep-lat/9807028`.
23. Hartmann, S. Effective Field Theories, Reductionism and Scientific Explanation. *Stud. Hist. Philos. Sci. B* **32,** 267–304 (2001).
24. Ordonez, C., Ray, L. & van Kolck, U. Nucleon-nucleon potential from an effective chiral Lagrangian. *Phys. Rev. Lett.* **72,** 1982–1985 (1994).
25. Ordonez, C., Ray, L. & van Kolck, U. The Two nucleon potential from chiral Lagrangians. *Phys. Rev. C* **53,** 2086–2105 (1996).
26. Wesolowski, S *et al.* Rigorous constraints on three-nucleon forces in chiral effective field theory from fast and accurate calculations of few-body observables. *Phys. Rev. C* **104,** 064001 (2021).
27. Wesolowski, S, Klco, N, Furnstahl, R. J., Phillips, D. R. & Thapaliya, A. Bayesian parameter estimation for effective field theories. *J. Phys. G* **43,** 074001 (2016).
28. Furnstahl, R. J., Klco, N, Phillips, D. R., & Wesolowski, S. Quantifying truncation errors in effective field theory. *Phys. Rev. C* **92,** 024005 (2015).
29. Wesolowski, S, Furnstahl, R. J., Melendez, A & Phillips, D. R. Exploring Bayesian parameter estimation for chiral effective field theory using nucleon–nucleon phase shifts. *J. Phys. G: Nucl. Part. Phys.* **46,** 045102 (2019).
30. Melendez, J. A., Wesolowski, S & Furnstahl, R. J. Bayesian truncation errors in chiral effective field theory: nucleon-nucleon observables. *Phys. Rev. C* **96,** 024003 (2017).
31. Sakurai, J. J. & Napolitano, J. *Modern Quantum Mechanics* ISBN: 978-1-4757-3799-8 (Cambridge University Press, 2017).
32. Shankar, R. *Principles of Quantum Mechanics* ISBN: 978-1-4757-0578-2 (Springer, 1994).
33. Belkic, D. *Principles of Quantum Scattering Theory* ISBN: 0-7503-0496-0 (Institute of Physics Publishing, 2004).
34. *INS data analysis center: SAID* `ttp://gwdac.phys.gwu.edu`. Accessed: 2022-05-06.
35. Hoshizaki, N. Appendix. Formalism of Nucleon-Nucleon Scattering. *Prog. Theor. Phys.* **42,** 107–159 (1968).
36. Taylor, J. R. *Scattering Theory: The Quantum Theory of Nonrelativistic Collisions* ISBN: 0-471-84900-6 (Wiley, 1972).
37. Friedrich, H. *Scattering Theory* ISBN: 978-3-642-38282-6 (Springer, 2013).
38. Epelbaum, E. & Meissner, U. G. On the Renormalization of the One-Pion Exchange Potential and the Consistency of Weinberg's Power Counting. *Few-Body Syst.* **54,** 2175–2190 (Oct. 2006).

39. Miller, S. *Nucleon-Nucleon Scattering in a Wave-Packet Formalism.* Licentiate Thesis. Chalmers University of Technology, Gothenburg (2020).
40. Landau, R. H. *Quantum Mechanics II: A Second Course in Quantum Theory, 2nd Edition* ISBN: 0-471-1 1608-4 (Wiley, 2004).
41. Morrison, M. A. & Feldt, A. N. Through scattering theory with gun and camera: Coping with conventions in collision theory. *Am. J. Phys.* **75,** 67–80 (2007).
42. Sammut, C. & Webb, G. I. *Encyclopedia of Machine Learning and Data Mining* ISBN: 978-1-4899-7686-4 (Springer, 2017).
43. Joseph, V. Space-Filling Designs for Computer Experiments: A Review. *Qual. Eng.* **28,** 28–35 (2016).
44. Muller, M. E. A Note on a Method for Generating Points Uniformly on N-Dimensional Spheres. *Commun. ACM* **2,** 19–20 (1959).
45. Dezert, J. & Musso, C. An efficient method for generating points uniformly distributed in hyperellipsoids, *Proceedings of the Workshop on Estimation Tracking and Fusion* (2001).
46. Tabachnick, B. G. & Fidell, L. S. *Using Multivariate Statistics, Sixth Edition* ISBN: 978-0-205-89081-1 (Pearson, 2013).
47. Witte, R. S. & Witte, J. S. *Statistics* ISBN: 978-1-119-25451-5 (Wiley, 2017).
48. MacKay, D. J. C. *Information Theory, Inference, and Learning Algorithms* ISBN: 978-0-5216-4298-9 (Cambridge University Press, 2003).
49. Iman, R. L., Helton, J. C. & Campbell, J. E. An Approach to Sensitivity Analysis of Computer Models: Part I—Introduction, Input Variable Selection and Preliminary Variable Assessment. *J. Qual. Technol.* **13,** 174–183 (1981).
50. Krane, K. S. *Introductory Nuclear Physics* ISBN: 978-0-471-80553-3 (Wiley, 1987).
51. Wang, M. *et al.* The AME2016 atomic mass evaluation (II). Tables, graphs and references. *Chin. Phys. C* **41,** 030003 (2017).
52. Rennie, R. & Law, J. *A Dictionary of Physics* ISBN: 978-0-1988-2147-2 (Oxford University Press, 2019).
53. Martin, B. R. & Shaw, G. *Nuclear and Particle Physics: An Introduction* ISBN: 978-1-119-34463-6 (Wiley, 2019).
54. Yuan, C. Uncertainty decomposition method and its application to the liquid drop model. *Phys. Rev. C* **93,** 034310 (2016).
55. Benzaid, D., Bentridi, S., Kerraci, A. & Amrani, N. Bethe–Weizsäcker semiempirical mass formula coefficients 2019 update based on AME2016e. *Nucl. Sci. Tech.* **31,** 9 (2020).
56. Forssén, C. Private communication. 2021.
57. Gregory, P. *Bayesian Logical Data Analysis for the Physical Sciences* ISBN: 978-0-521-15012-5 (Cambridge University Press, 2010).
58. Kejzlar, V, Neufcourt, L, Nazarewicz, W & Reinhard, P. G. Statistical aspects of nuclear mass models. *J. Phys. G* **47** (2020).
59. Wilson, A. J. Volume of n-dimensional ellipsoid. *SAX* **1,** 101–6 (2010).
60. Thim, O. Private communication. 2022.
61. Thim, O. *Renormalization of Chiral Effective Field Theory in the Nucleon-Nucleon Sector.* Master Thesis. Chalmers University of Technology, Gothenburg (2021).

62. Braaten, E. & Phillips, D. Renormalization-group limit cycle for the 1/ r2 potential. *Phys. Rev. A* **70,** 52111–052111 (2004).
63. Svensson, I., Ekström, A. & Forssén, C. Bayesian parameter estimation in chiral effective field theory using the Hamiltonian Monte Carlo method. *Phys. Rev. C* **105,** 014004 (2022).
64. Allen, W. D. & Ferguson, A. T. G. *Flux Measurements of Fast Neutrons with a Recoil Counter in the Energy Range of 50-2000 Kev* (Atomic Energy Research Establishment, 1955).
65. Engelke, C. E., Benenson, R. E., Melkonian, E & Lebowitz, J. M. Precision Measurements of the np Total Cross Section at 0.4926 and 3.205 MeV. *Phys. Rev.* **129,** 324 (1963).
66. Davis, J. C. & Barschall, H. H. Fast-Neutron Total Cross Section of Deuterium. *Phys. Rev. C* **3,** 1798–1803 (1971).
67. Bowen, P. H., Scanlon, J. P., Stafford, G. H. & Hodgson, J. J. T. P. E. Neutron total cross-sections in the energy range 15 to 120 MeV. *Nucl. Phys.* **2,** 457–464 (1961).
68. Culler, V. & Waniek, R. W. Total Cross Sections for High-Energy Neutrons. *Phys. Rev.* **99,** 585 (1955).
69. Scanlon, J. P., Stafford, G. H., Thresher, J. J., Bowen, P. H. & Langsford, A. Angular distributions for n-p scattering in the energy range 22.5 to 110 MeV. *Nucl. Phys.* **41,** 401–423 (1963).
70. Wilczynski, J *et al.* Measurements of the neutron-proton analyzing power in the energy range from 17 to 50 MeV. *Nucl. Phys. A* **425,** 458–468 (1984).
71. Sromicki, J, Holslin, D, Barker, M. D., Quin, P. A. & Haeberli, W. Spin Dependence in Low-Energy Neutron-Proton Scattering. *Phys. Rev. Lett.* **57,** 2359 (1986).
72. Stafford, G. H., Whitehead, C & Hillman, P. Polarization in neutron proton scattering at 95 MeV. *Nuovo Cim.* **5,** 1589–1597 (1957).
73. Hoshizaki, N. Appendix. Formalism of Nucleon-Nucleon Scattering. *Prog. Theor. Phys.* **42,** 107–159 (1968).
74. Buchner, J. Nested Sampling Methods. *Ann. Stat.* (2021).
75. Frame, D. *et al.* Eigenvector continuation with subspace learning. *Phys. Rev. Lett* **121(3),** 032501 (2018).
76. König, S., Ekström, A., Hebeler, K., Lee, D. & Schwenk, A. Eigenvector Continuation as an Efficient and Accurate Emulator for Uncertainty Quantification. *Phys. Lett. B* **810,** 135814 (2020).
77. Melendez, J., Drischler, C., Garcia, A., Furnstahl, R. & Zhang, X. Fast accurate emulation of two-body scattering observables without wave functions. *Phys. Lett. B* **821,** 136608 (2021).
78. Rabitz, H. & Conn, R. Variational Technique for Scattering Theory. *Phys. Rev. A* **7,** 577–585 (2 1973).

Appendix A

Additional Figures

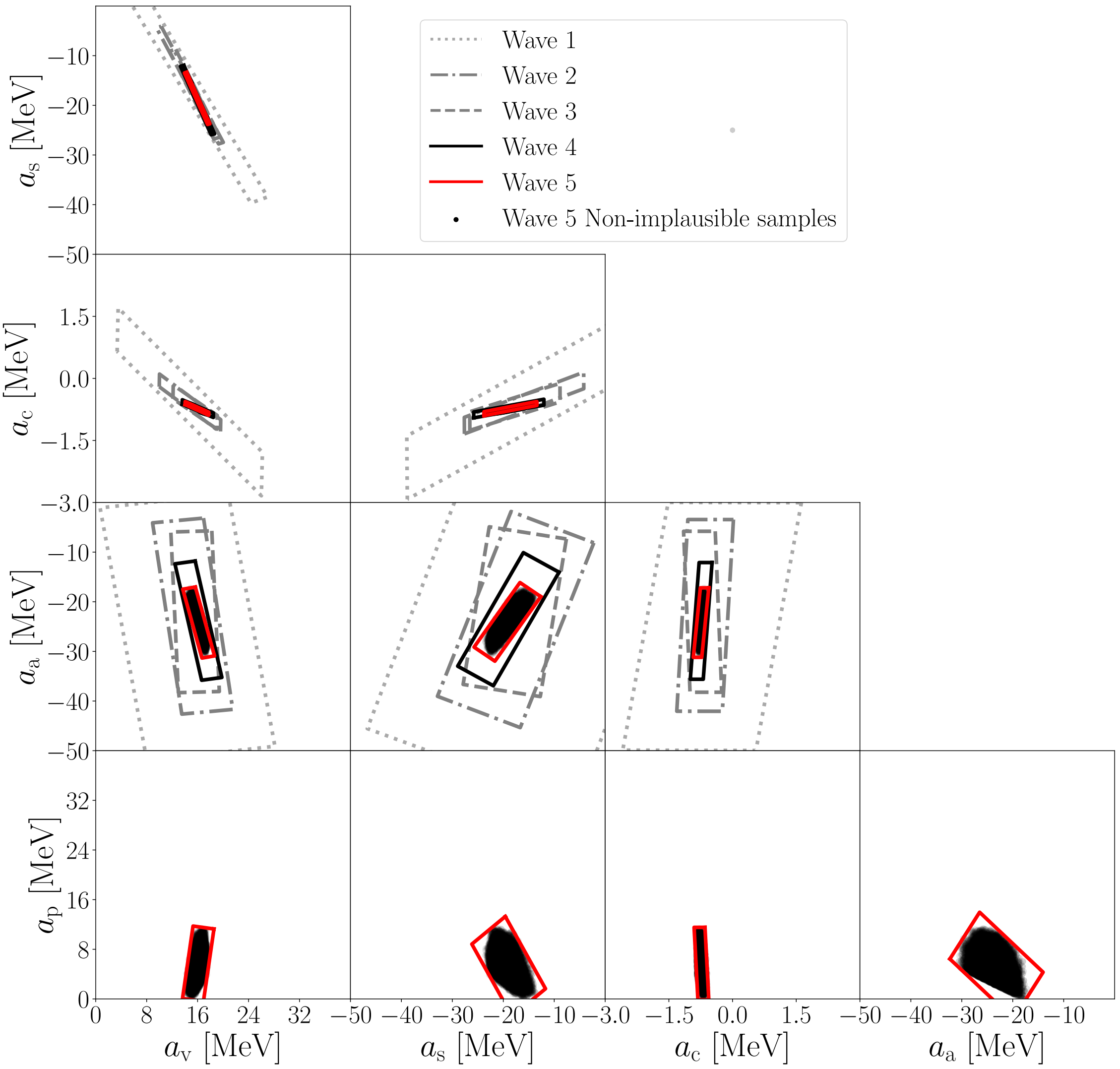

Figure A.1: Non-implausible volumes obtained after each wave of history matching of the liquid drop model, using a rotated hypercube-defined non-implausible volume. Also shown are the non-implausible samples remaining after wave 5. These figures are similar to those shown in Fig. 7.2 and Fig. 7.2, with the difference lying in the choice of non-implausible volume. Refer to Chapter 7 for further details on the relevant history match.

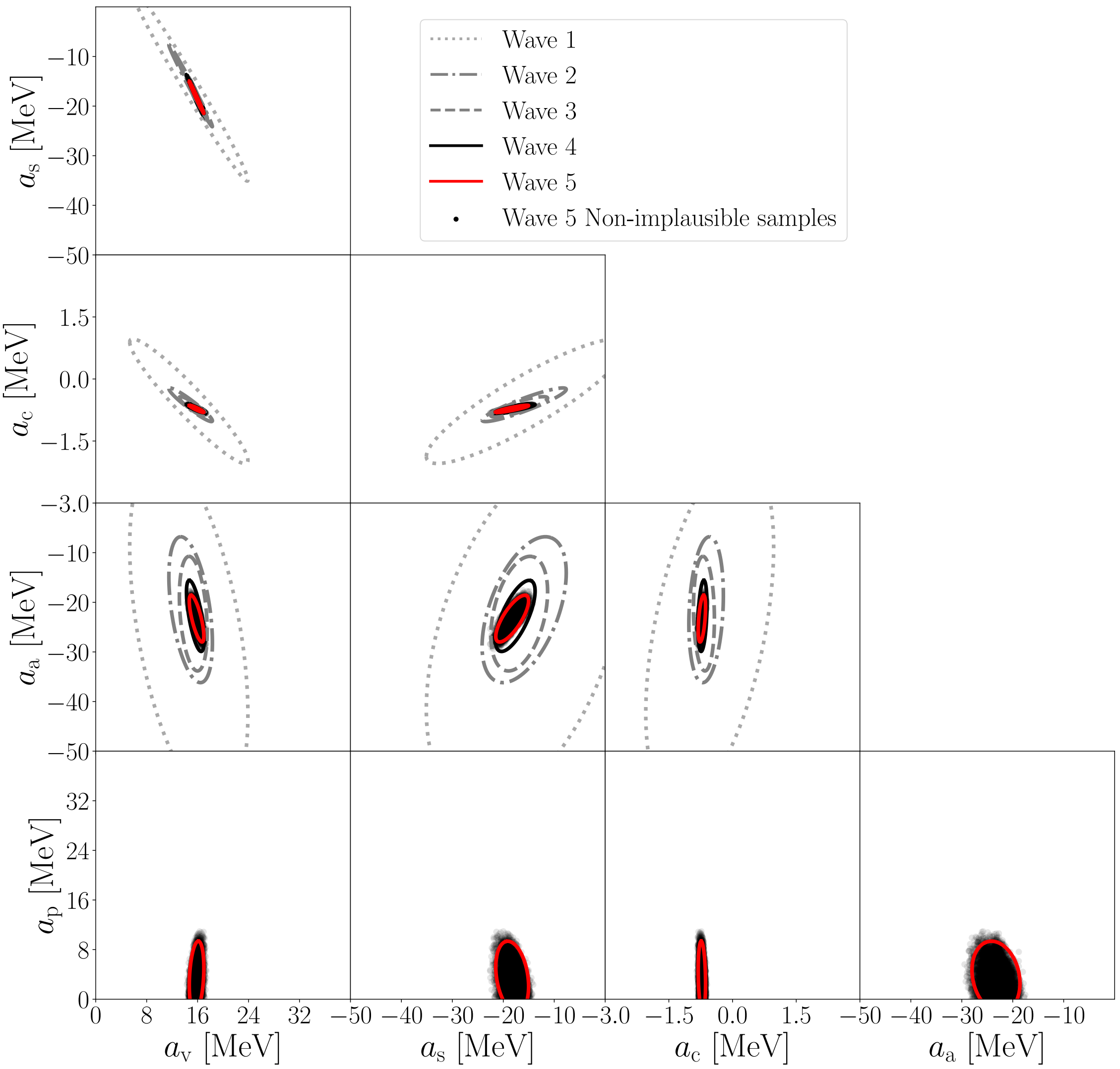

Figure A.2: Non-implausible volumes obtained after each wave of history matching of the liquid drop model, using a Gaussian-defined non-implausible volume. Each Gaussian volume has been represented by its 95% iso-probability surface. Also plotted are the non-implausible samples remaining in the final (fifth) wave. These figures are similar to those shown in Fig. 7.2 and Fig. 7.2, with the difference lying in the choice of non-implausible volume. Refer to Chapter 7 for further details on the relevant history match.

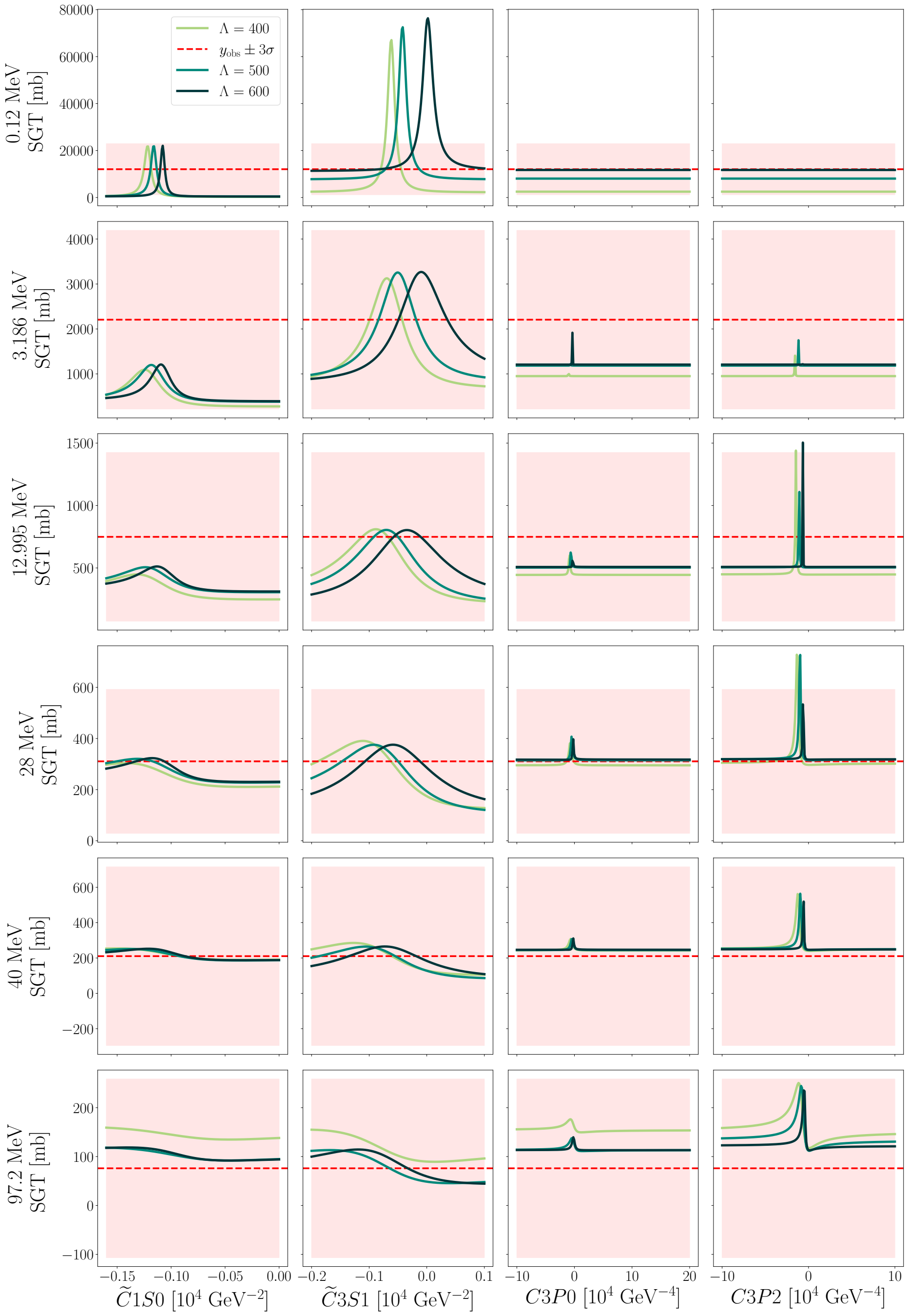

Figure A.3: SGT at a given T_{Lab}, computed across ranges of each LEC. When one LEC is varied, the others are set to correspond with the non-implausible sample with the lowest value of I_M, obtained in the history match of χEFT at LO in MWPC. Observables were computed for $\Lambda = \{400, 500, 600\}$ MeV.

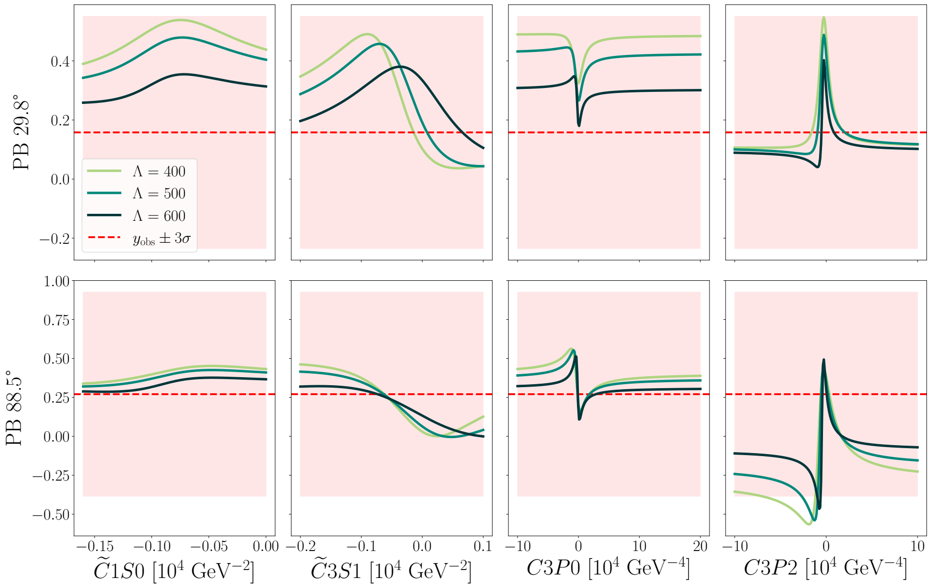

Figure A.4: PB computed across ranges of each LEC, with T_{Lab}=95 MeV. When one LEC is varied, the others are set to correspond with the non-implausible sample with the lowest value of I_M, obtained in the history match of χEFT.

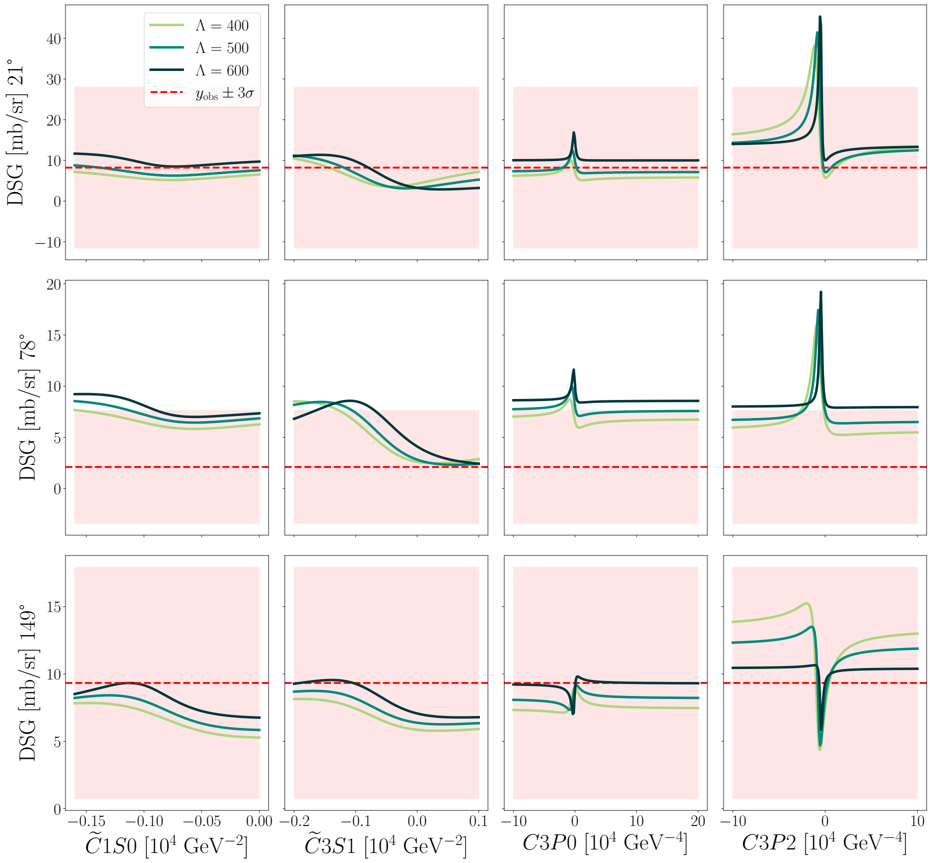

Figure A.5: DSG computed across ranges of each LEC, with T_{Lab}=99 MeV. When one LEC is varied, the others are set to correspond with the non-implausible sample with the lowest value of I_M, obtained in the history match of χEFT.

Appendix B

Further Scattering Theory

B.1 The S-Matrix

The S-matrix was introduced in Chapter 4 in relation to both the scattering T-matrix and scattering phase shifts. The following section aims to provide an intuitive understanding of the S-matrix, following theory given by Ref. [33].

We consider a time-dependent description of scattering. We introduce the time-dependent states $|\psi(t)\rangle$ that evolve following the time-dependent Schrödinger equation

$$i\hbar\frac{\partial}{\partial t}\left|\psi(t)\right\rangle = H\left|\psi(t)\right\rangle . \tag{B.1}$$

We define the initial state of the system $|\psi(t=0)\rangle = |\psi\rangle$, where $t=0$ is the time in which the particle interacts with the potential. The evolution of the system from an initial state $|\psi\rangle$ to a final state $|\psi(t)\rangle$ at time t may be described by the time evolution operator $U(t, t=0)$. The evolution is therefore represented by

$$\left|\psi(t)\right\rangle = U(t,t=0)\left|\psi\right\rangle = e^{iHt}\left|\psi\right\rangle . \tag{B.2}$$

We consider a particle approaching a potential from distance well outside the range of the potential, at $t=-\infty$. In the limits of $t\to-\infty$ and $t\to\infty$, the particle is far from the potential and thus the time evolution operator reduces to that of a free particle $U(t) = e^{-iH_0 t}$. We denote the asymptotic states as

$$\left|\psi(t)\right\rangle \xrightarrow[t\to-\infty]{} \left|\psi_{\text{in}}\right\rangle , \qquad \left|\psi(t)\right\rangle \xrightarrow[t\to+\infty]{} \left|\psi_{\text{out}}\right\rangle , \tag{B.3}$$

where $|\psi_{\text{in}}\rangle$ and $|\psi_{\text{out}}\rangle$ are eigenstates of H_0, and the interacting state $|\psi\rangle$ is an eigenstate of H. In terms of the time evolution operator, this may be written as

$$U(t,0)\left|\psi\right\rangle \xrightarrow[t\to-\infty]{} \left|\psi_{\text{in}}\right\rangle , \qquad U(t,0)\left|\psi\right\rangle \xrightarrow[t\to+\infty]{} \left|\psi_{\text{out}}\right\rangle , \tag{B.4}$$

or alternatively as

$$\left|\psi\right\rangle = U(0,-\infty)\left|\psi_{\text{in}}\right\rangle \equiv \Omega_+\left|\psi_{\text{in}}\right\rangle , \qquad \left|\psi\right\rangle = U(0,+\infty)\left|\psi_{\text{out}}\right\rangle \equiv \Omega_-\left|\psi_{\text{out}}\right\rangle . \tag{B.5}$$

Where $\Omega_{\pm}$ are defined as the Møller operators. We may therefore write that

$$|\psi_{\text{out}}\rangle = \Omega_{-}^{\dagger}\Omega_{+}\,|\psi_{\text{in}}\rangle\,. \tag{B.6}$$

One may then define the S-matrix, creating a relation between the in and out asymptotic states, as

$$S = \Omega_{-}^{\dagger}\Omega_{+}. \tag{B.7}$$

The probability for a scattering process is given by [41]

$$P(\,|\psi_{\text{out}}\rangle \leftarrow |\psi_{\text{in}}\rangle) = |\,\langle\psi_{\text{out}}|\,S\,|\psi_{\text{in}}\rangle\,|^2. \tag{B.8}$$

B.2 The Lippmann-Schwinger Equation

This section aims to briefly elaborate on the origins of the Lippmann-Schwinger equation. To begin, we repeat the Schrodinger equation

$$(H_0 + V)\,|\psi\rangle = E\,|\psi\rangle\,. \tag{B.9}$$

This can be rearranged to become

$$|\psi\rangle = \,|\phi\rangle + \frac{1}{E - H_0}V\,|\psi\rangle\,, \tag{B.10}$$

where $|\phi\rangle$ is an initial plane wave state that obeys

$$H_0\,|\phi\rangle = E\,|\phi\rangle\,, \tag{B.11}$$

ensuring that as $V \to 0$, $\phi \to \psi$. In order to avoid the singularity introduced by $E - H_0$, an infinitesimal rotation $i\epsilon$ is introduced [39], such that

$$|\psi\rangle = \,|\phi\rangle + \frac{1}{E - H_0 \pm i\epsilon}V\,|\psi\rangle\,, \tag{B.12}$$

The above relation is the *Lippmann-Schwinger equation.*

The transition matrix, or *T matrix*, is introduced as relating an outbound scattering state to a plane wave state as [31]

$$T\,|\phi'\rangle = V\,|\psi\rangle\,, \tag{B.13}$$

where $|\psi\rangle$ is an outbound scattering state with momentum $\boldsymbol{p}$ and $|\phi'\rangle$ is a plane wave state with momentum $\boldsymbol{p'}$. The momenta under consideration are defined as the relative momenta of two particles in the centre-of-mass frame, where $\boldsymbol{p} = \boldsymbol{p}_{\text{rel}}$ and $\boldsymbol{p'} = \boldsymbol{p'}_{\text{rel}}$.

By operating on Equation B.12 from the left with $\langle\phi|\,V$, the T-matrix is introduced into the Lippmann-Schwinger equation and we obtain the operator equation [31]

$$T = V + V\frac{1}{E - H_0 + i\epsilon}T. \tag{B.14}$$

The plane wave states can be denoted by their momentum as $|\phi'\rangle = |\boldsymbol{p}'\rangle$ and $|\phi\rangle = |\boldsymbol{p}\rangle$. We now introduce the notation $\langle\mathbf{p'}|\, T \,|\mathbf{p}\rangle = T(\mathbf{p'}, \mathbf{p})$ and $\langle\mathbf{p'}|\, V \,|\mathbf{p}\rangle = V(\mathbf{p'}, \mathbf{p})$. Representing Equation B.14 in momentum space gives the Lippmann-Schwinger equation in integral form as [40]

$$T(\mathbf{p'}, \mathbf{p}) = V(\mathbf{p'}, \mathbf{p}) + \int d^3\boldsymbol{k}\; V(\mathbf{p'}, \mathbf{k}) \frac{1}{E - E_k + i\epsilon} T(\mathbf{k}, \mathbf{p}). \tag{B.15}$$

DEPARTMENT OF PHYSICS
CHALMERS UNIVERSITY OF TECHNOLOGY
Gothenburg, Sweden
www.chalmers.se

CHALMERS
UNIVERSITY OF TECHNOLOGY